An Accelerated Corrosion Test Method for Pre-Cracked Reinforced Concrete

By

Shahriar Abed

DISSERTATION

Submitted in partial fulfillment of the requirements.

for the degree of Doctor of Philosophy at

The University of Texas at Arlington

August 2023

Arlington, Texas

Supervising Committee:

Supervisor: Professor Dr. Ali Abolmaali

Co-Supervising: Dr. Himan Hojat Jalali

Dr. Mohammad Najafi

Dr. Rasool Kenarangui

ABSTRACT

Accelerated Corrosion Test Method for Reinforced Composite Concrete

Shahriar Abed, Ph.D.

The University of Texas at Arlington, 2023

Supervising Professor: Professor Ali Abolmaali

Reinforced concrete (RC), a composite material combining the strength of concrete and the tensile strength of steel reinforcement, has significantly transformed the field of civil engineering and contributed to the advancement of modern infrastructure. Reinforced concrete structures are susceptible to deterioration over time despite their numerous advantages. One of the primary factors leading to the degradation of RC is the corrosion of steel reinforcement, primarily caused by exposure to aggressive environmental elements such as chloride ions, carbonation, and moisture. This dissertation aims to provide valuable insights into the accelerated corrosion behavior of steel bars embedded in concrete, considering factors such as crack size, chloride solution concentration, applied voltages, and the potential effects of autogenous healing.

This research's evaluation of corrosion rates relies on several methods, including Half-Cell Potential measurements, Weight Loss analysis of steel specimens, and elemental analysis of steel samples. The study comprises two phases: the first focuses on the accelerated corrosion of steel wires, while the second investigates accelerated corrosion on steel bars embedded in concrete.

In the first phase, 108 steel rebars were immersed in three different solution concentrations (2,000 ppm, 30,000 ppm, and 100,000 ppm) and subjected to six levels of applied voltages (0, 2, 4, 8, 12, and 16 Volts). The corrosion rate was determined by measuring weight loss over 14 days to identify critical voltage levels. The results indicate that increasing the applied voltage accelerates the corrosion process, with higher voltages (12 and 16 Volts) resulting in more significant weight loss and corrosion than lower voltages. Notably, after five days of testing, some rebars were no longer suitable for further analysis.

The second phase expands on the promising outcomes from the first phase by examining the accelerated corrosion on steel bars embedded in concrete specimens with varying crack sizes, concentration solutions, and voltages. A total of 1080 reinforced concrete cylinders were subjected to three different crack widths (0.01", 0.03", 0.05", and 0.1"), three voltage levels (2, 4, and 8 Volts), and three solution concentrations (2,000 ppm, 30,000 ppm, and 100,000 ppm). Monthly testing throughout six-month was conducted to evaluate the influence of crack size, voltage levels, and solution concentration on the corrosion behavior of the embedded steel bars. Half-cell potentials, per ASTM-C876 standards, were recorded, and the weight loss of the steel bars was measured monthly to quantify the corrosion level. Additionally, scanning electron microscopy (SEM) and energy-dispersive X-ray spectroscopy (EDX) analyses were performed to assess the levels of corrosion and oxidation in each sample.

In summary, the research seeks to predict the deterioration of reinforced steel structures and estimate the service life of concrete pipes in real-world conditions. This is achieved through accelerated corrosion studies, load-bearing capacity assessments, and applying the Arrhenius concept for extrapolation and projection.

ACKNOWLEDGMENT

I would like to extend my deepest appreciation to my supervising professor, Professor Ali Abolmaali, for his invaluable guidance, unwavering support, and continuous dedication throughout my career at the Center for Structural Engineering Research/Simulation and Pipeline Inspection. This dissertation would not have reached its successful completion without his expert supervision.

I would like to express my sincere gratitude to Dr. Himan Hojat Jalali for generously dedicating his time and offering invaluable guidance as a Co-Supervisor throughout this project and his scholarly pursuits. Additionally, I extend my heartfelt appreciation to Dr. Park, whose valuable insights have provided me with invaluable methodologies and expanded my knowledge, undoubtedly shaping the trajectory of my future work. Furthermore, I would like to sincerely thank my esteemed committee members, Dr. Najafi, and Dr. Kenarangui, for their valuable feedback, which has significantly contributed to the refinement of this research.

I would like to acknowledge the technical and financial support provided by the American Concrete Pipe Association, particularly Corey Header, whose assistance was instrumental in the successful execution of this project.

Finally, I would like to thank my friends and colleagues at the Center for Structural Engineering Research/Simulation and Pipeline Inspection for their assistance throughout this research endeavor. Their contributions have been indispensable to the overall accomplishment of this work.

August 2023

DEDICATION

To my parents, whose steadfast love, guidance, and sacrifices have been the foundation upon which I have built my aspirations and achievements. Your consistent support and unwavering belief in me have propelled me forward, even during the most challenging times. I am forever grateful for your enduring encouragement and the values you have instilled in me. This dissertation is a testament to your resolute faith in my abilities and a reflection of the countless opportunities you have provided me. Thank you for being my pillars of strength and for always being there for me.

To my loving wife (Sevda), who has been my rock and source of inspiration throughout this journey, I dedicate this accomplishment to you. Your unwavering support, patience, and understanding have been invaluable. Your love has fueled my determination and kept me going during the most challenging times. Thank you for always standing by my side.

To my devoted brother (Shahram) and caring sister (Zohreh), your constant support and belief in my abilities have strengthened me throughout this journey. Your words of wisdom and encouragement have guided me during challenging times. Thank you for being my pillars of support.

Last but certainly not least, I dedicate this work to my exceptional supervisor, Dr. Ali Abolmaali. Your guidance, mentorship, and expertise have been transformative in my academic and professional journey.

To all mentioned above, I am immensely proud to have you in my life.

Table of Contents

CHAPTER 1. INTRODUCTION 1

1.1. Overview 1

1.2. Corrosion 3

1.3. Accelerated Corrosion 4

1.3.1. Accelerated Corrosion Test 5

1.4. Problem Statements 6

1.5. Scope and Goals 10

1.6. Thesis Outline 11

1.7. Research Objectives and Contributions 12

1.8. Practical Application of Stud 13

CHAPTER 2. LITERATURE REVIEW 15

2.1. Overview 15

2.2. Literature Review 15

CHAPTER 3. EXPERIMENTAL PROGRAM 29

3.1. Accelerated Corrosion on Steel Wires. 29

3.1.1. Test Procedure 29

3.1.2. Test Results 31

3.1.3. SEM & EDX 38

3.2. Accelerated Corrosion of Bars Embedded in Concrete Cylinders 42

3.2.1. Overview 42

3.2.2. Scope and Goals 44

3.3. Autogenous Healing 45

3.4. Test Methodology 47

3.4.1. Half-Cell Potential 47

3.4.2. Scanning Electron Microscope 55

3.4.3. Energy Dispersive X-Ray 56

3.4.4. Crack Measuring Microscope 58

3.5. Material Properties 59

3.5.1. Concrete 59

3.5.2. Rebars 64

3.5.3. Spacers 67

3.5.4. Chloride Sodium 68

CHAPTER 4. PREPARATION OF TEST 70

4.1. Experimental Process 70

CHAPTER 5. RESULTS 80

5.1. Overview 80

5.2. Results from Profometer 81

5.3. Results from Remaining Weight 82

5.3.1. Effect of Voltages on Corrosion Rate 83

5.3.2. Effect of Crack Width on Corrosion Rates 91

5.3.3. Effect of Sodium Chloride on Corrosion Rates 97

5.4. Results from SEM & EDX 101

5.4.1. SEM Results 102

5.4.2. EDX Results 104

5.5. Results from Different Rebar Sizes 113

5.6. Results from Autogenous Healing 114

CHAPTER 6. STATISTICAL ANALYSIS 116

6.1. Overview 116

6.2. Analysis of Variance 117

6.3. Post-Hoc Tests (Tukey's HSD) 122

6.4. Regression Analysis 126

6.5. Prediction Models 127

6.5.1. Using Python to Generate the Linear Regression Model and Equation 128

6.5.2. Linear Regression Model 130

6.5.3. The Equation for Linear Regression 133

6.5.4. Interaction Linear Regression 133

6.5.5. The Equation for Interaction Regression 135

6.5.6. Neural Network Model 137

CHAPTER 7. SUMMARY AND CONCLUSION 141

7.1. Summary 141

7.2. Conclusion 142

7.3. Recommendation of Future Work 147

References 148

Appendix I: Numerical Results Obtained from Profometer & Remaining Weight 155

Appendix II: Graphical Results from the Remaining Weight 159

Appendix III: Codes Generated in Python Software 179

Appendix IV: Steps for Making the Prediction MODEL in MATLAB 182

List of Figures

Figure 1. Reinforced Concrete Pipe 2
Figure 2. Electro Chemical Chloride Reactor (ASTM G48) 6
Figure 3. Crack Width Limitations According to ASTM C1840 (ACPA Webinar, 2023) 7
Figure 4. Service Life Curve 14
Figure 5. Wire Coil from Forterra 29
Figure 6. Accelerated Corrosion Test on Rebars 31
Figure 7. Average Remaining Weight and Diameter at 2,000 ppm 32
Figure 8. Average Remaining Weight and Diameter at 30,000 ppm 33
Figure 9. Average Remaining Weight and Diameter at 100,000 ppm 35
Figure 10. Corrosion Effects on the Steel Bars Under (a) Control & 2Volts, (b) Control & 8Volts, (c) Control & 16 Volts After 14 Days at 2,000 ppm. 36
Figure 11. Corrosion Effects on the Steel Bars Under (a) Control & 2Volts, (b) Control & 8Volts, (c) Control & 12 Volts After 14 Days at 30,000 ppm. 36
Figure 12. Corrosion Effects on the Steel Bars Under (a) Control & 2Volts, (b) Control & 8Volts, (c) Control & 12 Volts After 14 Days at 100,000 ppm. 37
Figure 13. Oxidation Level of Surface in EDX Results. 39
Figure 14. Microscopic Surface Image of Specimens at Control With 500x Magnification. 40
Figure 15. Microscopic Surface Image of Specimens at 2 Volt With 500x Magnification. 40
Figure 16. Microscopic Surface Image of Specimens at 4 Volt With 500x Magnification. 40
Figure 17. Microscopic Surface Image of Specimens at 8 Volt With 500x Magnification. 41
Figure 18. Microscopic Surface Image of Specimens at 12 Volt With 500x Magnification. 41
Figure 19. Change of the Weight of Iron and Oxygen at the Sample's Surface. 42
Figure 20. Steel Bars Embedded in a Concrete Cylinder with a Crack. 43
Figure 21. Schematic of Half-Cell Potential Testing (Piyush et al. 2016) 48
Figure 22. (a) Anode and Cathode Cells, and (b) Setup of Half-Cell Potential Measurement. (GIATEC Web, 2023) 49
Figure 23. Principle of Steel Corrosion in Concrete with Oxygen Availability (Proceq Profometer Operation Instructions) 51
Figure 24. Measuring Principle (Proceq Profometer Operation Instructions) 52
Figure 25. Proceq Profometer 53
Figure 26. Rod Corrosion Electrode 54

Figure 27. SEM & EDX Machine 58
Figure 28. Crack Measuring Microscope 59
Figure 29. (a) Slump Test for High Cement Content and (b) Low Cement Content 63
Figure 30. Concrete Provided at Forterra 64
Figure 31. (a) Rebars Used in 24" Pipe, and (b) Rebars Used in 96" Pipe 66
Figure 32. Wires for 24 inches of Pipe 67
Figure 33. Spacers with the Width of 0.03" 68
Figure 34. Sodium Chloride 69
Figure 35. (a) Partitioned Cap in Four Equal Sections, (b) Wooden Pieces as a marker to Divide in Four Equal Parts, and (c) Marking the Cylinders 70
Figure 36. Cutting the Cylinders 71
Figure 37. Making a Hole at the Bottom of the Cylinders 71
Figure 38. Spacers with (a) 0.01", (b) 0.03", (c) 0.05", and (d) 0.1" Widths 72
Figure 39. Placing the Spacers 73
Figure 40. (a) Measuring the Rebar's Weight, and (b) Labeling 74
Figure 41. Concrete Cubes for Cover 74
Figure 42. Placing the Wires in Cylinders 75
Figure 43. (a) Using WD-40, and (b) Casting Cylinders 76
Figure 44. Setup Pools. 77
Figure 45. Voltage Application Setup 79
Figure 46. Profometer Reading (mV) & Remaining Weight (%) 82
Figure 47. Effect of Voltages at 2,000 ppm & 0.01" Crack Width 85
Figure 48. Effect of Voltages at 30,000 ppm and 0.01" Crack Width. 89
Figure 49. Effect of Voltages at 100,000 ppm and 0.01" Crack Width. 90
Figure 50. Effect of Crack Width at 2,000 ppm and 0 Volt 94
Figure 51. Effect of Crack width at 2,000 ppm and 2 Volt 97
Figure 52. Effect of Sodium Chloride on Corrosion Rate at 0 Volt and 0.01" Crack Width 101
Figure 53. SEM for 0.01" Crack Width at the Control and 2,000 ppm Under (a) 120x and (b) 400x Magnification 102
Figure 54. SEM for 0.01" Crack Width at the Control and 30,000 ppm Under (a) 90x and (b) 400x Magnification 102

Figure 55. SEM for 0.01" Crack Width at the Control and 100,000 ppm Under (a) 50x and (b) 400x Magnification 103
Figure 56. SEM for 0.1" Crack Width at the Control and 2,000 ppm Under (a) 50x and (b) 400x Magnification 103
Figure 57. SEM for 0.1" Crack Width at the Control and 30,000 ppm Under (a) 50x and (b) 400x Magnification 103
Figure 58. SEM for 0.1" Crack Width at the Control and 100,000 ppm Under (a) 50x and (b) 400x Magnification 104
Figure 59. Element Analysis of 0.01" Crack Width at Control and 2,000 ppm 106
Figure 60. Element Analysis of 0.01" Crack Width at Control and 30,000 ppm 107
Figure 61. Element Analysis of 0.01" Crack Width at Control and 100,000 ppm 108
Figure 62. Elemental Analysis of 0.01" with Different Concentration Solutions at 0 Volt 109
Figure 63. EDX Results for 0.01" Crack Width and 0 Volt 109
Figure 64. EDX Results for 0.01" Crack Width and 2 Volt 111
Figure 65. EDX Results for 0.03" Crack Width and 2 Volt 112
Figure 66. EDX Results for 0.05" Crack Width and 2 Volt 112
Figure 67. EDX Results for 0.1" Crack Width and 2 Volt 113
Figure 68. Effect of Rebar Size on Corrosion Rate at 2,000 ppm and 0.01" Crack Width. 114
Figure 69. Effect of Cement Amount on Autogenous Healing 115
Figure 70. Observed vs. Predicted Values for Remaining Weight at Linear Regression Model 130
Figure 71. Observed vs. Predicted Values for Remaining Weight at Interaction Linear Regression 135
Figure 72. Predicted Values for Remaining Weight at Neural Network Model 138
Figure 73. Effect of Voltages in Predicted and Actual Terms 139
Figure 74. Effect of Solutions in Predicted and Actual Terms 140
Figure 75. Effect of Crack Width in Predicted and Actual Terms 140
Figure 76. Effect of Voltages at 2,000 ppm and 0.01" Crack Width. 159
Figure 77. Effect of Voltages at 2,000 ppm and 0.03" Crack Width. 159
Figure 78. Effect of Voltages at 2,000 ppm and 0.05" Crack Width. 160
Figure 79. Effect of Voltages at 2,000 ppm and 0.1" Crack Width. 160
Figure 80. Effect of Voltages at 30,000 ppm and 0.01" Crack Width. 161
Figure 81. Effect of Voltages at 30,000 ppm and 0.03" Crack Width. 161
Figure 82. Effect of Voltages at 30,000 ppm and 0.05" Crack Width. 162

Figure 83. Effect of Voltages at 30,000 ppm and 0.1" Crack Width. 162
Figure 84. Effect of Voltages at 100,000 ppm and 0.01" Crack Width. 163
Figure 85. Effect of Voltages at 100,000 ppm and 0.03" Crack Width. 163
Figure 86. Effect of Voltages at 100,000 ppm and 0.05" Crack Width. 164
Figure 87. Effect of Voltages at 100,000 ppm and 0.1" Crack Width. 164
Figure 88. Effect of Crack Width at 0 Volt & 2,000 ppm..... 165
Figure 89. Effect of Crack Width at 2 Volt & 2,000 ppm..... 165
Figure 90. Effect of Crack Width at 4 Volt & 2,000 ppm..... 166
Figure 91. Effect of Crack Width at 8 Volt & 2,000 ppm..... 166
Figure 92. Effect of Crack Width at 0 Volt & 30,000 ppm..... 167
Figure 93. Effect of Crack Width at 2 Volt & 30,000 ppm..... 167
Figure 94. Effect of Crack Width at 4 Volt & 30,000 ppm..... 168
Figure 95. Effect of Crack Width at 8 Volt & 30,000 ppm..... 168
Figure 96. Effect of Crack Width at 0 Volt & 100,000 ppm..... 169
Figure 97. Effect of Crack Width at 2 Volt & 100,000 ppm..... 169
Figure 98. Effect of Crack Width at 4 Volt & 100,000 ppm..... 170
Figure 99. Effect of Crack Width at 8 Volt & 100,000 ppm..... 170
Figure 100. Effect of Concentration Solutions at 0.01" Crack Width & 0 Volt. 171
Figure 101. Effect of Concentration Solutions at 0.01" Crack Width & 2 Volt. 171
Figure 102. Effect of Concentration Solutions at 0.01" Crack Width & 4 Volt. 172
Figure 103. Effect of Concentration Solutions at 0.01" Crack Width & 8 Volt. 172
Figure 104. Effect of Concentration Solutions at 0.03" Crack Width & 0 Volt. 173
Figure 105. Effect of Concentration Solutions at 0.03" Crack Width & 2 Volt. 173
Figure 106. Effect of Concentration Solutions at 0.03" Crack Width & 4 Volt. 174
Figure 107. Effect of Concentration Solutions at 0.03" Crack Width & 8 Volt. 174
Figure 108. Effect of Concentration Solutions at 0.05" Crack Width & 0 Volt. 175
Figure 109. Effect of Concentration Solutions at 0.05" Crack Width & 2 Volt. 175
Figure 110. Effect of Concentration Solutions at 0.05" Crack Width & 4 Volt. 176
Figure 111. Effect of Concentration Solutions at 0.05" Crack Width & 8 Volt. 176
Figure 112. Effect of Concentration Solutions at 0.1" Crack Width & 0 Volt. 177
Figure 113. Effect of Concentration Solutions at 0.1" Crack Width & 2 Volt. 177
Figure 114. Effect of Concentration Solutions at 0.1" Crack Width & 4 Volt. 178

Figure 115. Effect of Concentration Solutions at 0.1" Crack Width & 8 Volt. 178

List of Tables

Table 1. Conducted and Corresponding Number of Specimens 30

Table 2. Average Remaining Weight and Diameter of Wires at 2,000 ppm..... 31

Table 3. Average Remaining Weight and Diameter of Wires at 30,000 ppm..... 33

Table 4. Average Remaining Weight and Diameter of Wires at 100,000 ppm..... 34

Table 5. Test Schedule and the Corresponding Numbers of Cylinder Specimens..... 44

Table 6. Test Schedule and the Corresponding Number of Cylinder Specimens for Autogenous Healing 47

Table 7. Potential Measured Values (mV) and Corrosion Probability (Adapted from ASTM C876) 50

Table 8. Typical Ranges of Half-Cell Potential of Rebars in Concrete (Adopted from RILEM TC-154,2003) 55

Table 9. Proportions of Concrete Mix Design with High Cement Ratio 61

Table 10. Proportions of Concrete Mix Design with Lower Cement Ratio 62

Table 11. Salt Mass Required to Achieve Different Concentrations in the Pool 78

Table 12. Effect of Voltages at 2,000 ppm and 0.01"Crack Width. 84

Table 13. ANOVA Results. 85

Table 14. HSD Results. 86

Table 15. Effect of Voltages at 30,000 ppm and 0.01" Crack Width. 87

Table 16. Effect of Voltages at 100,000 ppm and 0.01" Crack Width. 89

Table 17. Effect of Crack Width on Corrosion Rate at 2,000 ppm and 0 Volt 91

Table 18. Correlation Coefficient for Different Crack Sizes at 2,000 ppm and 0 Volt..... 93

Table 19. Effect of Crack Width on Corrosion Rate at 2,000 ppm and 2 Volt 94

Table 20. Pearson Correlation Coefficient for Different Solutions..... 99

Table 21. Tukey HSD Results for Different Solutions..... 99

Table 22. Element Analysis of 0.01" Crack Width at Control and 2,000 ppm 105

Table 23. Element Analysis of 0.01" Crack Width at Control and 30,000 ppm 107

Table 24. Element Analysis of 0.01" Crack Width at Control and 100,000 ppm 108

Table 25. Crack Closer Measurements for High and Low Cement Content 114

Table 26. F- Distribution Table 120

Table 27. Effect of Voltages at 30,000 ppm and 0.01" Crack Width 123

Table 28. Linear Regression Results 131

Table 29. Coefficient Values for Each Variable 132

Table 30. Coefficient Values for Interaction Regression 134

Table 31. Results for 2,000 ppm and 0.01" Crack Width at Different Voltages. 155

Table 32. Results for 2,000 ppm and 0.03" Crack Width at Different Voltages. 155

Table 33. Results for 2,000 ppm and 0.05" Crack Width at Different Voltages. 155

Table 34. Results for 2,000 ppm and 0.1" Crack Width at Different Voltages. 156

Table 35. Results for 30,000 ppm and 0.01" Crack Width at Different Voltages. 156

Table 36. Results for 30,000 ppm and 0.03" Crack Width at Different Voltages. 156

Table 37. Results for 30,000 ppm and 0.05" Crack Width at Different Voltages. 157

Table 38. Results for 30,000 ppm and 0.1" Crack Width at Different Voltages. 157

Table 39. Results for 100,000 ppm and 0.01" Crack Width at Different Voltages. 157

Table 40. Results for 100,000 ppm and 0.03" Crack Width at Different Voltages. 158

Table 41. Results for 100,000 ppm and 0.05" Crack Width at Different Voltages. 158

Table 42. Results for 100,000 ppm and 0.1" Crack Width at Different Voltages. 158

CHAPTER 1. INTRODUCTION

1.1. Overview

Reinforced concrete (RC) is widely used as a construction material that combines the compressive strength of concrete with the tensile strength of steel reinforcement. It has revolutionized the field of civil engineering and played a crucial role in the development of modern infrastructure. The versatility, durability, and cost-effectiveness of reinforced concrete have made it a preferred choice for various structural applications, including buildings, bridges, dams, and pavements.

The usage of reinforced concrete in construction offers several advantages. Firstly, it provides high structural strength, enabling the construction of robust and long-lasting structures that can withstand heavy loads. The ability to mold concrete into various shapes and sizes allows for flexible design possibilities, accommodating diverse architectural requirements. Additionally, the fire-resistant properties of reinforced concrete make it a relatively reliable choice for structures that can withstand high temperatures and protect human lives and property (Kosmatka et al., 2002, Mehta et al., 2014).

One of the prominent applications of reinforced concrete is the fabrication of reinforced concrete pipes (RCPs), shown in Figure 1. Reinforced concrete pipes (RCP) have long been essential components in the construction of various infrastructure projects. These cylindrical conduits are reinforced with steel to enhance their structural integrity and load-bearing capabilities, making them widely used in stormwater management systems, sewage conveyance, culverts, and other underground applications.

Figure 1. Reinforced Concrete Pipe

The advantages of reinforced concrete pipes stem from their durability, corrosion resistance, and cost-effectiveness. Their ability to withstand harsh environmental conditions and a longer service life contribute to sustainable infrastructure development.

However, reinforced concrete pipes are not immune to deterioration despite their numerous benefits. Various factors contribute to the degradation of RCPs structures over time. One of the primary causes is the corrosion of steel reinforcement, which can occur due to exposure to aggressive environments, such as chloride ions, carbonation, and moisture (Soutsos et al. 2016). The corrosion process leads to the formation of cracks, weakening the structural integrity and potentially compromising the safety of the entire system.

1.2. Corrosion

Corrosion in reinforced concrete refers to the deterioration of the reinforcing steel within concrete due to chemical reactions between the steel and its surrounding environment. This corrosion process can weaken the structural integrity of the concrete and eventually lead to structural failures if not addressed.

Several factors can contribute to the corrosion of reinforced concrete:

1. ***Carbonation*:** Carbonation occurs when carbon dioxide from the atmosphere reacts with the alkaline components in concrete, reducing its pH level. Lowered pH reduces the passivation of the reinforcing steel, making it more susceptible to corrosion (Mindess et al. 2006). Carbonation is a prominent catalyst for the degradation of reinforced concrete infrastructures within environments characterized by elevated carbon dioxide (CO2) concentrations, notably prevalent in urban hubs and parking edifices. In light of the substantial atmospheric pollution and pronounced CO2 content endemic to major metropolitan areas, it is plausible to anticipate a heightened manifestation of concrete structures exhibiting escalated degrees of carbonation advancement.

2. ***Chloride ingress***: Chloride ions can penetrate the concrete and reach the reinforcing steel, typically from de-icing salts or seawater exposure. In the presence of moisture, chloride ions break down the passive oxide layer on the steel surface, initiating corrosion (Neville and Brooks, 2010). The translocation of chloride ions towards the rebar materializes via a diffusion mechanism. This phenomenon can be delineated into a dual-phase framework comprising propagation and initiation stages. The propagation phase is inaugurated as the ions permeate the concrete matrix, exerting no immediate impact on the integrity of the

steel reinforcement. In contrast, the inception stage materializes once the concentration of chlorides attains a pivotal threshold, prompting the genesis of deteriorative processes.

3. ***Moisture and Oxygen***: Moisture and oxygen in the concrete create an electrolytic environment supporting corrosion. The moisture acts as an electrolyte, facilitating the movement of ions, while oxygen serves as the oxidizing agent for the corrosion reactions (Gaynor, 1982).

4. ***Concrete quality and cover thickness***: Poor quality concrete with a high permeability or inadequate cover thickness over the reinforcing steel can accelerate the ingress of aggressive substances and increase the likelihood of corrosion (Böhni, 2004).

1.3. Accelerated Corrosion

Chloride-induced corrosion is a significant long-term potential cause of damage and deterioration in reinforced concrete pipes (RCPs), primarily due to the aggressive action of chloride ions on the steel reinforcement. The effects of chloride-induced corrosion on the structure may take several years to become visible since the process is gradual in the natural environment. Researchers commonly employ the Accelerated Corrosion Test (ACT) to investigate the durability and mechanical properties of RC structures and aim to simulate and predict the long-term effects of corrosion in a shorter time.

Several methodologies can expedite the corrosion process, including applying an electrical current, elevating temperature and humidity, or subjecting the material to aggressive environments. These techniques are employed to accelerate the degradation of materials and enhance the corrosion rate.

1.3.1. Accelerated Corrosion Test

The Electrochemical Chloride Reactor is a laboratory apparatus that studies chloride-induced corrosion in reinforced concrete structures. Electrochemical reactors investigate the effects of chloride ions on the corrosion of steel reinforcement in a controlled and accelerated manner. The reactor consists of two main components: a steel bar, representing the reinforcement, and a counter electrode, often made of copper or platinum. These electrodes are immersed in a chloride solution that serves as the corrosive environment. The chloride solution typically contains a specific concentration of chloride ions, which are known to initiate and accelerate the corrosion process.

(ASTM G48)

Electrochemical reactions occur at their respective interfaces when an electrical potential is applied between the steel bar (anode) and the counter electrode (cathode). At the steel bar, the anodic reaction involves the oxidation of iron to form ferrous ions:

$$Fe \rightarrow Fe^{2+} + 2e^{-}$$

Meanwhile, at the counter electrode, the cathodic reaction takes place, which typically involves the reduction of hydrogen ions to form hydrogen gas:

$$2H^{+} + 2e^{-} \rightarrow H_2$$

These reactions occur within the chloride solution, leading to the migration of chloride ions toward the steel bar. This simulates the process of chloride ingress and the subsequent initiation and propagation of corrosion in reinforced concrete structures.

Controlling the applied voltage, chloride concentration, and testing duration can accelerate the corrosion process and evaluate various factors influencing the corrosion rate, such as chloride content, concrete composition, and protective measures.

The Electrochemical Chloride Reactor provides a controlled environment to investigate the mechanisms and kinetics of chloride-induced corrosion and to assess the effectiveness of corrosion mitigation strategies. (Brad and Faulkner, 2000).

A typical setup for the ACT is an electrochemical chloride reactor, as illustrated in Figure 2, comprising a steel bar and a copper bar immersed in a chloride solution. The reactor continuously extracts electrons from one end and delivers them to the other.

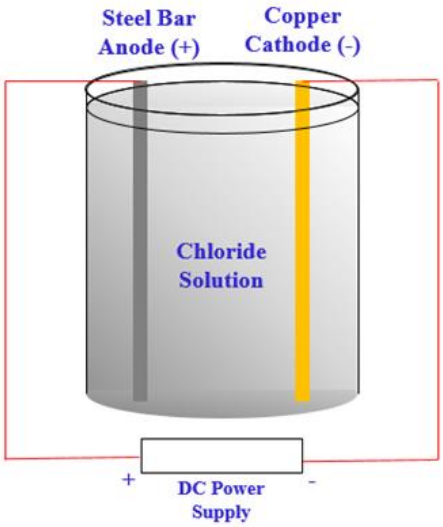

Figure 2. Electro Chemical Chloride Reactor (ASTM G48)

1.4. Problem Statements

Reinforced concrete pipes play a vital role in infrastructure systems, where their structural integrity, leak prevention, and long-term durability are of utmost importance. To ensure their functionality, crack widths in these pipes are regulated by industry guidelines such as those

provided by the American Concrete Institute (ACI), the American Association of State Highway and Transportation Officials (AASHTO), and the American Society for Testing and Materials (ASTM C1840) to ensure structural integrity, prevent leakage, and maintain long-term durability.

ACI 318 recommends a maximum allowable crack width of 0.013 inches for reinforced concrete elements, while AASHTO LRFD Bridge Design Specifications suggest a limit of 0.02 inches under service loads. However, ASTM C1840 suggests the limitations of cracks according to Figure 3.

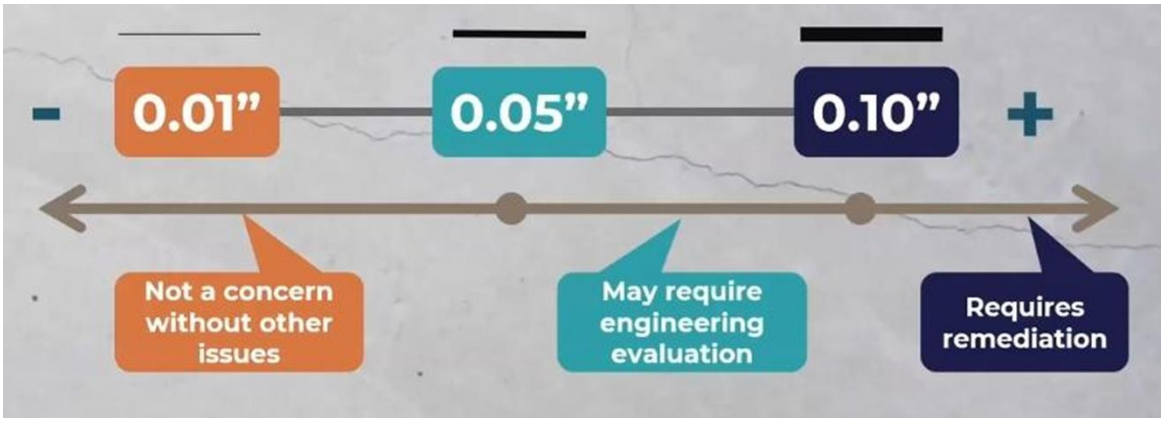

Figure 3. Crack Width Limitations According to ASTM C1840 (ACPA Webinar, 2023)

While these guidelines offer crack width limits for reinforced concrete elements, examining the relationship between crack widths and corrosion rates in concrete pipes is necessary. Additionally, the concentration of sodium chloride solutions within pipes varies according to environmental conditions and industrial standards. So, three distinct concentration levels of chloride sodium were identified for this study. Furthermore, different voltages are directly applied to rebars within the pipes to accelerate the corrosion process. Corrosion induced by chloride ions presents a significant challenge in harsh environments and greatly impacts the durability and longevity of concrete pipes.

Therefore, it is crucial to comprehensively understand the effects of crack width, sodium chloride concentration, and applied voltages on corrosion rates to develop effective corrosion prevention strategies.

To address this research gap, this study investigates the effects of crack widths on corrosion rates in reinforced concrete pipes. Four crack width values will be considered: 0.01 inches, 0.03 inches, 0.05 inches, and 0.1 inches. This study will focus on three concentration levels: 2,000, 30,000, and 10,000 ppm, representing realistic ranges.

Additionally, the corrosion process naturally takes time; therefore, different voltages will be directly applied to rebars within the pipes to accelerate the corrosion process and facilitate experimental investigations. To develop effective corrosion prevention strategies for concrete pipes, knowing the impact of crack width, sodium chloride concentration, and applied voltages on corrosion rates is essential. By utilizing accelerated testing methods to simulate actual pipe conditions, this research aims to provide valuable insights into these factors. However, it is essential to acknowledge the limitations of accelerated testing.

Limitations:

1. ***Laboratory Conditions*:** The tests were conducted in a controlled laboratory environment, which may not fully replicate real-world conditions in the field. As a result, the obtained corrosion rates might differ from those experienced in actual structures.
2. ***Limited Crack Width Range*:** The study may have investigated a limited range of crack widths, and the findings might not be applicable to crack widths outside the tested range. Different crack widths beyond those examined could produce distinct corrosion behaviors.

3. ***Specific Solution Concentrations*:** The investigation focused on only three different concentration solutions, and the results might not account for the full spectrum of solution concentrations present in real-world scenarios. Other concentration levels may exhibit varying corrosion behaviors.

4. ***Voltage Application*:** The application of voltages to accelerate the corrosion process might not perfectly simulate the conditions in real structures. The relationship between applied voltages and actual field conditions could be more complex.

5. ***Representativeness of Concrete Cylinders*:** While concrete cylinders are commonly used for corrosion testing, they may not fully represent the behavior of complex real-world structures, such as pipes or bridges. Differences in geometry and other factors might affect corrosion rates.

6. ***Additional Influencing Factors*:** The study considered crack width, concentration solution, and voltages as primary factors influencing corrosion rates. However, other variables, such as temperature, humidity, material properties, and chemical interactions, were not explicitly studied but could play a role in the corrosion process.

7. ***Duration of Testing*:** The duration of the tests might have been limited, and longer exposure times could lead to different corrosion behaviors. The long-term effects of crack width, solution concentration, and voltage application on corrosion rates were not explicitly studied.

Nonetheless, this study will contribute to investigating the combined impact of three pivotal factors (crack width, concentration solutions, and electrical voltages) on the corrosion process in reinforced concrete structures. While previous research has often examined these factors in

isolation, this study takes a pioneering approach by comprehensively analyzing their interactions. This contributes to a more holistic understanding of corrosion behavior, bridging the gap between controlled laboratory experiments and real-world conditions and developing practical and reliable corrosion prevention strategies, enhancing the durability and performance of reinforced concrete pipes in infrastructure systems.

1.5. Scope and Goals

The scope of this research is to expand on the findings of the background study (accelerated corrosion on steel bars presented in chapter 3) and develop a protocol for measuring accelerated corrosion on steel bars embedded in cylindrical concrete specimens with varying crack sizes, concentration solutions, and voltages. It evaluates the relationship between crack width, sodium chloride concentration, and applied voltages on concrete pipe corrosion rates.

The primary goal is to investigate the impact of crack width, solution concentration, and voltages on the corrosion behavior of accelerated aging. Additionally, the study aims to explore the phenomenon of autogenous healing concerning corrosion and evaluate the crack width influence on the accelerated corrosion test.

Tests will be conducted on concrete cylinders immersed in chloride solutions to analyze the corrosion levels using various techniques, including Half-Cell Potentials, weight loss measurements, Scanning Electron Microscopy (SEM), and Energy-Dispersive X-ray Spectroscopy (EDX).

1.6. Thesis Outline

The research study is structured into seven chapters, which include an introduction, literature review, experimental program, preparation for testing, results, statistical analysis, and a final chapter summarizing the conclusions and suggesting future work.

Chapter One, titled "Introduction," provides an overview of the accelerated corrosion process and outlines the research objectives.

Chapter Two, the "Literature review," explores previous studies related to corrosion studies, the autogenous healing of cracked concrete, and the analysis of SEM/EDX. Based on prior research, it also discusses the effect of different rebar sizes on corrosion.

Chapter Three elaborates on the experimental procedures, divided into two phases: accelerated corrosion on rebars and accelerated corrosion on rebars embedded in concrete. This chapter presents the testing protocols employed.

Chapter Four outlines the steps in preparing concrete cylinders and the half-cell potential tests and weight loss measurements conducted.

Chapter Five presents the results from all the tests conducted throughout the research.

Chapter Six involves the statistical analysis and the development of prediction models and equations based on the data obtained.

In chapter seven, the research findings, conclusions, and recommendations for future work are discussed.

Additionally, Appendices I, II, III, and IV contain numerical results obtained from the Profometer and weight loss measurements, graphical figures depicting the impact of each parameter, steps for

generating equations using Python, and steps for generating predicted versus observed values in models, respectively.

1.7. Research Objectives and Contributions

This research aims to:

1. Develop a protocol for measuring accelerated corrosion on steel bars embedded in cylindrical concrete specimens with varying crack sizes.
2. Investigate the effect of accelerated corrosion on steel bars embedded in concrete cylinders fully immersed in varying concentrations of chloride solutions.
3. Determine the influence of crack width on the corrosion behavior of steel bars under accelerated corrosion conditions.
4. Evaluate the impact of applied voltage levels (2 Volt, 4 Volt, and 8 Volt) on the accelerated corrosion rates of embedded steel bars and compare them with the control samples.
5. Examine the relationship between crack widths (0.01 in., 0.03 in., 0.05 in., and 0.1 in.) and corrosion rates to assess the effect of crack size on corrosion progression.
6. Record Half-Cell Potentials according to ASTM-C876 to assess the corrosion state of the embedded steel bars.
7. Measure the weight loss of the steel bars every month for up to six (6) months to quantify the level of corrosion.
8. Perform SEM and EDX analyses on the samples to determine the levels of corrosion and oxidation in each sample.

9. Investigating the correlation between varying rebar sizes and corrosion rates.
10. Investigate the influence of autogenous healing on the corrosion behavior of steel by studying crack closure using a crack measuring microscope.
11. Statistical analysis was used to find the significant differences in each parameter.

By achieving these research objectives, the study aims to provide valuable insights into the accelerated corrosion behavior of steel bars embedded in concrete, the role of crack size and concrete encasement, the influence of chloride solutions and applied voltages, and the potential effects of autogenous healing. The findings will enhance the understanding of corrosion mechanisms and inform the development of more effective corrosion mitigation strategies for reinforced concrete structures.

1.8. Practical Application of Stud

Various factors, including crack width and concentration of solutions, influence the corrosion process in reinforced concrete structures. Detecting the corrosion rates on these structures typically takes several years. Accelerated corrosion tests involve applying voltages to reinforced concrete specimens to expedite this process. This can help isolate and analyze the effects of individual parameters on corrosion rates.

The outcomes of this research have significant implications for real-world scenarios. The results will aid in predicting the extent of deterioration in reinforced steel structures with different crack widths using an acceleration corrosion protocol by immersing the specimens in saline solution with different concentrations and applying different voltages simultaneously. The insights gained from this study can be particularly valuable for infrastructures like pipes, culverts, and bridges.

More specifically, the extension of the study's findings allows for a thorough exploration of how accelerated corrosion impacts these parameters in a realistic operational environment. Furthermore, a comprehensive D-load test can be methodically conducted to assess the load-bearing capacity of concrete pipes. This investigation's overarching goal is to estimate the expected service life of concrete pipes proactively.

Estimating this service life involves extending a diminishing curve based on empirical results gathered from the D-load test. The resulting curve is converted into a trajectory representing a projected 100-year service life to make this analysis more applicable in real-world scenarios. This transformation is accomplished using an equation grounded in the theoretical principles of the Arrhenius concept. The Arrhenius concept involves activation energy, foundational in understanding how chemical reactions evolve, particularly in changing environmental conditions. Figure 4 visually presents the service life curve corresponding to the accelerated conditions.

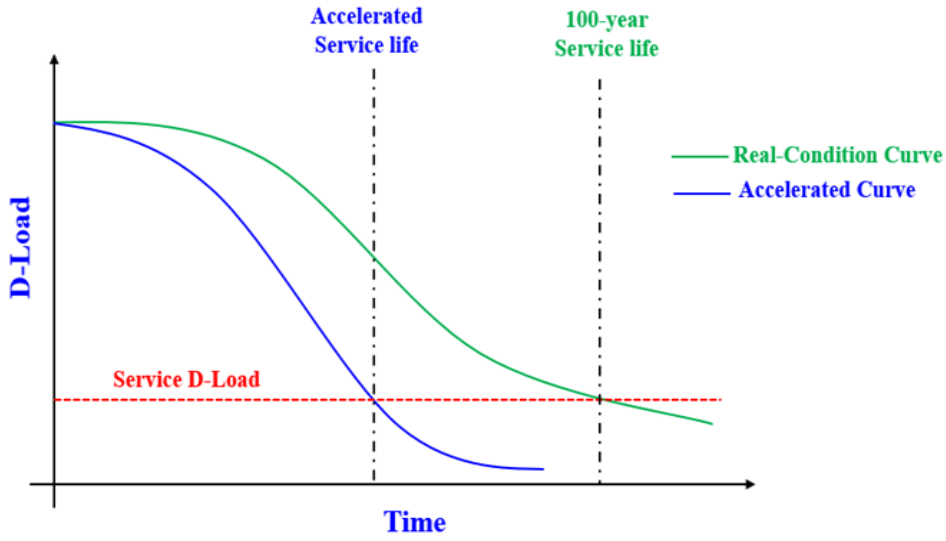

Figure 4. Service Life Curve

CHAPTER 2. LITERATURE REVIEW

2.1. Overview

The literature review will encompass pertinent aspects concerning the research topic, explicitly focusing on corrosion studies, accelerated corrosion methodologies, the effect of crack width, concentration solutions, and voltages on reinforcement corrosion, potential half-cell testing, autogenous concrete healing, SEM, and EDX analyses.

2.2. Literature Review

Typically, the highly alkaline cement matrix in concrete maintains the reinforcing steel in a passive state, where the corrosion rate remains minimal due to forming a protective layer of iron oxide on the steel surface, according to the findings of Tuutti (1982). However, localized breakdown of this passivating layer occurs when enough chlorides reach the reinforcing bars, initiating the corrosion process. Chlorides can exist in concrete in two forms: dissolved in the pore solution as free chlorides or chemically and physically bound to the cement hydrates and their surfaces as bound chlorides. Only the pore solution's free chlorides continue penetrating through the concrete cover.

Baweja et al. (1998) conducted a study involving 50 reinforced concrete slabs that were partially immersed in sodium chloride (NaCl) solution with a concentration of 30,000 parts per million (ppm). The study aimed to compare the corrosion behavior of different cement mixes used in the slabs. The specimens were prepared using four different types of cement, and the water-to-cement ratio was varied. They examined the extent of corrosion in the steel reinforcement for each type of cement mix and compared the results. Results revealed that when the water-to-cement ratio exceeded 0.55, the blended cement concretes exhibited more corrosion in the steel reinforcement than the Portland cement concretes. The assessment of corrosion activity, measured by

electrochemical corrosion activity, indicated that the blended cement mixes showed a higher level of corrosion in the steel reinforcement under these conditions. The results suggest that the choice of cement type and control of the water-to-cement ratio are crucial factors in determining the corrosion resistance of concrete structures in chloride-rich environments.

Hearn (1998) explored the concept of autogenous healing. Autogenous healing refers to the inherent ability of cementitious materials to heal cracks in fractured zones. Hearn defined this phenomenon as the capacity of cement to repair cracks within the material without external intervention naturally. The research conducted by Hearn highlights the self-healing potential of cementitious materials, where cracks can be partially or entirely closed through various chemical and physical processes. Understanding the mechanism of autogenous healing is crucial for assessing concrete structures' long-term durability and self-repairing capabilities.

Another important finding was that the side of the rebar exposed to cracks exhibited more corrosion than other parts. Moreover, a transition from pitting to general corrosion was observed as one moved away from the crack opening. Angst et al. (2010) suggested that microscopic defects on the lower side of rebars were more prone to corrosion initiation. Visual or macroscopic defects like voids in contact with the steel surface may not always be the primary cause of corrosion initiation.

Chung (2012) explored various methods and materials employed for corrosion control of reinforced concrete. The reviewed methods included steel surface treatment, utilization of admixtures in concrete, and application of surface coatings on concrete. Steel surface treatment involves techniques to improve the corrosion resistance of the steel reinforcement. These treatments can include the application of protective coatings, such as zinc or epoxy-based coatings, or using corrosion inhibitors. The use of admixtures in concrete refers to incorporating certain

chemicals or substances during the mixing process to enhance the corrosion resistance of the concrete. These admixtures can modify the properties of the concrete, making it more resistant to chloride penetration or reducing the corrosion potential of the embedded steel. Surface coatings on concrete involve applying protective layers on the surface of the concrete to provide a barrier against the ingress of aggressive substances like chloride ions. Coatings can include polymer-based materials, epoxy coatings, or other corrosion-resistant coatings. As discussed in the paper, accelerated corrosion positively affects corrosion resistance. This can result in improved alkalinity loss in the concrete or enhanced penetration of corrosion inhibitors, thereby providing increased protection against corrosion.

Li et al. (2012) researched the effective diffusion coefficient of chlorides in concrete and found a model to protect the reinforcing steel from corrosion; the main objective of the research is to develop a model that can accurately predict the effective diffusion coefficient of chlorides in concrete. This diffusion coefficient is a critical parameter for assessing chloride ingress and its potential impact on the durability of concrete structures. The proposed model is described as a multi-phase model and suggests the complex nature of chloride transport in concrete, considering multiple phases or components that influence the diffusion process. These phases may include the cement paste, aggregates, pore solution, and other constituents present in concrete. The model focuses on predicting the effective diffusion coefficient of chlorides in concrete. The effective diffusion coefficient represents the overall diffusion behavior of chlorides in the concrete matrix, considering various factors such as pore structure, chloride binding, and other influencing parameters.

Busba and Sagüés (2013) highlighted the occurrence of corrosion in reinforced concrete structures, which is attributed to the ingress of chloride ions from seawater and de-icing salts into the steel

rebars. They emphasized the significance of the chloride content in determining the corrosion initiation stage, known as the Chloride Threshold Level (CLT). Once the chloride content reaches or surpasses the CLT, corrosion is triggered. The CLT serves as a critical threshold, indicating the chloride concentration at which the corrosive process begins. It represents the minimum level of chloride content required to initiate corrosion in the steel reinforcement within the concrete structure. It is important to note that any chloride concentration equal to or exceeding the CLT poses a significant risk for corrosion development. The findings emphasize the importance of monitoring and controlling the chloride content in reinforced concrete structures. By maintaining the chloride levels below the CLT, measures can be taken to prevent or delay the onset of corrosion, thus enhancing the durability and service life of the concrete members. Understanding the CLT and its implications allows engineers and practitioners to implement appropriate chloride control strategies, such as corrosion inhibitors, improved concrete mix designs, or protective coatings. By effectively managing chloride exposure, the risk of corrosion can be minimized, ensuring the structural integrity and longevity of reinforced concrete elements.

Moreno and Balasubramanian (2013) presented preliminary results of an investigation aimed at better understanding and characterizing the ongoing corrosion of reinforced concrete pipes (RCP) exposed to relevant conditions using accelerated corrosion. Specifically, the study focused on RCP exposed to concrete with high moisture content and low oxygen concentration at the rebar. Studying the corrosion behavior and mechanisms in such environments can enhance understanding of the factors influencing accelerated corrosion in reinforced concrete. The preliminary results presented by Moreno in this investigation provided initial findings regarding the ongoing corrosion of RCP. These findings could contribute to developing strategies and measures to mitigate corrosion and enhance the durability of reinforced concrete structures exposed to high moisture

content and low oxygen conditions. Moreno's work adds to the existing knowledge on accelerated corrosion and provides valuable insights into the corrosion behavior of reinforced concrete pipes under specific environmental conditions. The findings from this investigation may have practical implications for corrosion control and prevention in concrete structures exposed to similar conditions.

Shao and Li (2014) conducted a study to analyze the chloride diffusion equation in cracked reinforced concrete pipe piles. They developed an analytical solution for this equation, which allowed them to understand the behavior of chloride diffusion in the presence of cracks. Furthermore, they derived a mathematical expression that established a relationship between crack width and the equivalent diffusion coefficient. The discovery of this relationship between crack width and the diffusion coefficient was significant because it provided insights into the impact of cracks on chloride diffusion. This knowledge enables the development of a method for predicting the service life of cracked reinforced concrete pipe piles while considering the effects of cracks on chloride diffusion.

In a study by Palin et al. (2015), the performance of cement specimens made with ordinary Portland cement (OPC) and blast furnace slag (BFS) cement was investigated in fresh and seawater environments. The research aimed to assess the autogenous healing capabilities of the specimens under different conditions. The study's findings indicated that OPC specimens immersed in seawater exhibited the highest rate of autogenous healing compared to both OPC and BFS specimens immersed in freshwater. This suggests that the presence of seawater positively influences the healing process in OPC-based concrete.

Maes et al. (2016) conducted a study on autogenous healing in concrete and made significant observations regarding the healing process. One of their findings was that autogenous healing

occurs faster through the precipitation of calcium carbonates compared to specimens continuously immersed in water. Furthermore, Maes determined that the width of cracks plays a crucial role in the healing capacity of concrete. Their research revealed that cracks with a width of less than 105 μm could heal completely, indicating a successful crack closure. However, complete healing was not observed for cracks more significant than 105 μm, suggesting limitations in the healing process for wider cracks. The findings of Maes' study provide important insights into the autogenous healing phenomenon in concrete. Identifying the role of calcium carbonate precipitation and the dependence on crack width contribute to a better understanding of the factors that influence the healing potential of concrete. Understanding the healing capabilities of concrete is crucial for assessing the self-repairing properties of structures and predicting their long-term durability. The insights provided by Maes' research can inform the development of strategies to enhance the autogenous healing process in concrete, leading to improved structural integrity and longevity.

Otieno et al. (2016) presented an empirical model to predict the rate of chloride-induced corrosion in cracked reinforced concrete structures. Traditional models based on uncracked concrete failed to estimate the corrosion rate in these structures accurately. The model incorporated the influence of crack width on the corrosion rate during the crack propagation phase to address this limitation. By considering the effects of crack width, the proposed model provides a tool to determine the optimal combination of concrete strength, cover depth, and crack width. This information is essential for achieving the desired durability and exposure performance in marine environments where corrosion risks are particularly significant.

The model fills a crucial gap in corrosion prediction for cracked reinforced concrete structures. It acknowledges the importance of crack width in influencing the corrosion process and provides a more accurate corrosion rate estimation. This model is utilized to make informed decisions

regarding material selection, dimensions, and crack control measures, ultimately ensuring the longevity and performance of reinforced concrete structures in marine environments.

Ragab et al. (2016) research focused on seawater's impact on concrete deterioration. The study investigated the interactions between concrete and various substances present in seawater, including chlorides, sulfates, and magnesium. Using scanning electron microscopy (SEM), Ragab analyzed the formation of different products resulting from these reactions and examined the chloride ion concentration to varying depths within the concrete specimens. The study provided details into the complex reactions between concrete and seawater components, highlighting the potential changes in concrete properties. Examining chloride ion concentration at different depths helped to understand the depth of chloride penetration into the concrete, which is critical for assessing the durability and potential corrosion risks in marine environments.

Li and Zhang (2016) also studied the relationship between rebar size and the corrosion rate in reinforced concrete. The results indicated that the size of the rebar had a significant influence on the corrosion rate. It was found that larger diameter rebars have a lower-speed corrosion rate than smaller ones. Furthermore, the study also highlighted that the rebar size affected the distribution of corrosion products. Larger diameter rebars exhibited a more uniform distribution of corrosion products along the rebar surface, which helped to protect the rebar from further corrosion. On the other hand, smaller diameter rebars showed localized and more severe corrosion, leading to higher corrosion rates.

Chen et al. (2017) did another study on the SEM and EDX analysis to investigate the corrosion characteristics of rebars in a chloride-rich environment. They investigated the formation and growth of corrosion products, the effects of chloride penetration on rebar surfaces, and the

mechanisms of rebar corrosion by doing the SEM and EDX together. The findings from this analysis contributed to evaluating the corrosion rate.

In a study by Wang et al. (2017), the researchers investigated the cement ratio's influence on concrete's autogenous healing capacity. The findings revealed that an increase in cement ratio positively affected the extent and rate of autogenous healing. A higher cement ratio provided more available calcium hydroxide and other reactive components, which contributed to the formation of additional hydration products during the healing process. The high hydration products facilitated the sealing of cracks and enhanced the self-healing ability of the concrete. The paper also found a relationship between cement ratio, crack width reduction, and the effectiveness of autogenous healing.

Weiwei et al. (2017) studied the influence of crack width on chloride-induced corrosion in reinforced concrete structures. Through a 654-day laboratory test on cracked concrete specimens exposed to chloride solution, the study investigated the relationship between crack width, chloride concentration, and corrosion rate. The experimental results demonstrated that the corrosion rates in cracked specimens increased with higher percentages of chloride ions and wider crack widths. The study also revealed the interrelationship between crack width and chloride concentration influencing the corrosion rate. An empirical model was developed to predict the corrosion rate, considering the effects of crack width and chloride concentration. This model allows for estimating the maximum allowable crack width and chloride concentration to maintain the corrosion rate below a desired threshold.

Zhang et al. (2017) studied the influence of crack width on the corrosion rate of reinforced steel in concrete structures. The results indicated that an increase in crack width was directly correlated with an accelerated corrosion rate of the steel. The wider the cracks, the greater the exposure of

the steel reinforcement to corrosive agents, such as moisture and chloride ions, leading to a higher corrosion rate. The paper also examined the role of crack depth and length in conjunction with crack width to assess their combined effects on the corrosion behavior of reinforced steel.

Chen et al. (2018) investigated the influence of sodium chloride on the corrosion behavior of reinforced steel in a coastal environment. The findings revealed that the presence of sodium chloride had a significant impact on the corrosion rate of the steel. The study also examined the synergistic effects of other environmental factors, such as humidity and temperature, in combination with sodium chloride on the corrosion behavior of reinforced steel.

Garcia et al. (2018) examined the impact of sodium chloride on the corrosion rate of reinforced steel in a chloride-rich environment. Their findings revealed that as the concentration of sodium chloride increased, the corrosion rate of the reinforced steel also increased significantly. The presence of chloride ions from sodium chloride led to the breakdown of the passive film on the steel surface, accelerating the corrosion process. The results indicated a strong correlation between the chloride content, specifically sodium chloride, and the corrosion rate of the reinforced steel.

In a study conducted by Kim et al. (2018), the researchers focused on the influence of applied voltages on the corrosion rate of reinforced steel in a simulated corrosive environment. The findings revealed that the corrosion rate of the steel increased with higher applied voltages. The applied voltage was a driving force for electrochemical reactions, accelerating the corrosion process. The paper also discussed the role of voltages in promoting the breakdown of the passive film on the steel surface and facilitating the initiation and propagation of corrosion.

A study by de Rooij et al. (2018) found the capabilities of autogenous concrete healing with varying cement ratios. Their findings indicated that high cement ratio concrete exhibited superior

autogenous healing compared to low cement ratio concrete. The higher cement ratio provided more un-hydrated cement particles, which were available to react form healing products in moisture. These healing products contributed to the self-sealing of cracks and improved the overall healing capacity of the concrete. They also discovered the influence of cementitious materials and their impact on autogenous healing behavior.

The influence of rebar size on the corrosion rate of reinforced concrete structures was studied by Song et al. (2018). Their findings revealed that rebar size significantly impacted the corrosion rate. It was observed that larger-diameter rebars exhibited a lower corrosion rate than smaller-diameter rebars. The larger surface area of the smaller diameter rebars provided a more exposed metal surface, which resulted in a higher corrosion rate due to increased exposure to corrosive agents such as chlorides and moisture. The study also highlighted that the effect of rebar size on corrosion rate was influenced by other factors such as concrete cover thickness, environmental conditions, and concrete quality. These factors interacted with rebar size to affect the diffusion of corrosive agents and oxygen access to the rebar surface, ultimately influencing the corrosion rate.

A study conducted by Cao et al. (2019) investigated the impact of rebar size on the corrosion rate in reinforced concrete. The results indicated that rebar size played a significant role in determining the corrosion rate. It was found that smaller-diameter rebars exhibited a higher corrosion rate compared to larger-diameter rebars. This can be attributed to the larger surface area-to-volume ratio of smaller-diameter rebars, which leads to a higher concentration of corrosion-inducing species at the rebar surface. They also found that the corrosion rate was influenced by the availability of oxygen and the transport of corrosive agents. Smaller diameter rebars were more susceptible to localized corrosion due to limited oxygen diffusion and the concentration of

chlorides near the surface. In contrast, larger diameter rebars had better access to oxygen and exhibited a more uniform corrosion pattern.

In a study by Li et al. (2019), they found the impact of applied voltages on the corrosion rate of reinforced steel in a marine environment. The results showed that higher applied voltages increased the steel reinforcement's corrosion rate. The applied voltages influenced the electrochemical reactions at the steel-concrete interface, leading to accelerated corrosion. The paper also discussed the phenomenon of accelerated low-water corrosion (ALWC) and its association with applied voltages, shedding light on the mechanisms by which voltage influences the corrosion behavior of reinforced steel.

Pacheco-Torgal et al. (2019) studied the cement ratio's impact on self-healing concrete's autogenous healing potential. The results indicated that the increased cement ratio positively influenced the material's autogenous healing capacity. A higher cement ratio resulted in greater availability of calcium hydroxide and other reactive compounds, which played a crucial role in the precipitation of healing products. The increased amount of healing products facilitated the closure of cracks and improved the self-healing ability of the concrete. They researched the role of supplementary cementitious materials combined with cement ratio to enhance autogenous healing performance.

Smith et al. (2019) investigated the influence of sodium chloride on the corrosion rate of reinforced steel in a marine environment. They found that the presence of sodium chloride significantly accelerated the corrosion process. The chloride ions in the sodium chloride solution acted as aggressive agents, promoting the breakdown of the passive film on the steel surface and facilitating the initiation and propagation of corrosion. The results directly correlated with sodium chloride concentration and the reinforced steel's corrosion rate.

Wang et al. (2019) studied the impact of crack size on the corrosion rate of reinforced steel in a marine environment. The findings revealed that the corrosion rate increased with larger crack sizes. The cracks provided pathways for the ingress of corrosive agents, such as chloride ions and moisture, leading to accelerated corrosion processes. The study also examined the influence of different crack widths and depths on the corrosion behavior of reinforced steel, providing insights into the relationship between crack size and corrosion rate.

In a study conducted by Zhang et al. (2019), they employed SEM and EDX analysis to investigate the corrosion behavior of rebars in concrete structures. The SEM analysis provided high-resolution images of the corroded rebar surface, allowing for the visualization of corrosion products, pitting, and other morphological changes. The EDX analysis complemented the SEM images by providing basic composition information on the corrosion products. This technique helped identify the presence of chlorides, oxides, and other corrosion-related elements on the rebar surface.

The combined use of SEM and EDX analysis provided valuable insights into the corrosion mechanisms, the distribution and composition of corrosion products, and the extent of rebar degradation. It offered a detailed characterization of the corrosion process, aiding in assessing the corrosion resistance of different rebar materials and evaluating corrosion protection strategies.

Al-lami (2020), in his Ph.D. dissertation, investigated the corrosion of cracked pipes that were immersed in various sodium chloride concentrations. The study's primary objective was determining these pipes' service life under different chloride exposure conditions. By subjecting the cracked pipes to various sodium chloride concentrations, Al-lami aimed to simulate real-world scenarios and assess the impact of chloride exposure on the corrosion behavior of the pipes. The research likely involved monitoring parameters such as corrosion rate, depth of corrosion penetration, and visual inspection of the pipes over a certain period. The study conducted by Al-

lami can help estimate such pipes' service life and develop corrosion control strategies in environments with varying chloride concentrations.

In a study by Li et al. (2020), the researchers investigated the influence of crack width on the corrosion rate of reinforced steel in concrete structures exposed to a chloride-rich environment. The results demonstrated that increased crack width led to a higher corrosion rate of the steel reinforcement. The study also explored the relationship between crack width, corrosion rate, and the service life of reinforced concrete structures, providing insights into the importance of crack control in mitigating corrosion-induced deterioration.

Martin et al. (2020) focused on the Chloride-induced corrosion of steel bars in reinforced concrete, particularly in marine environments and areas exposed to de-icing salts, which has significantly contributed to the deterioration of essential structures like bridge decks and parking garages. The consequences of corrosion damage in these structures are often evident through surface rust staining, concrete cover cracking, and spalling caused by the expansion of corrosion products. Moreover, it can result in future structural issues due to the loss of cross-sectional area of the reinforcing steel and diminished bond strength along the steel-concrete interface.

In another study by Rossi et al. (2020), deep corrosion pits were observed at the steel-concrete interface (SCI) in areas where voids were present. After 20 years, specimens made with ordinary Portland cement (OPC) showed more corrosion in terms of volume loss compared to specimens made with blended cement. The direction of concrete casting relative to the orientation of rebars was also considered, and it was found that specimens with casting perpendicular to the steel rebars exhibited more bleeding water formation under the bars. This, in turn, led to defects in the SCI and the formation of voids. Consequently, in such cases, the underside of the rebar displayed more corrosion than other parts.

Silva et al. (2020) focused on the autogenous healing behavior of concrete with high and low cement ratios. The results revealed that high cement ratio concrete exhibited improved autogenous healing compared to low cement ratio concrete. The higher cement ratio provided a more extensive reservoir of reactive components, such as calcium hydroxide, which was crucial in forming healing products. The paper also discussed the impact of cementitious materials and their interaction with the cement ratio on autogenous healing performance.

In the other study, Tang et al. (2020) researched the SEM and EDX analysis of corroded rebars in concrete and investigated microstructural changes and elemental composition. The SEM analysis allowed for examining the rebar surface at high magnification, revealing the corrosion product deposition. The EDX analysis provided elemental mapping and quantification of the corrosion products, enabling the identification of specific elements involved in the corrosion process. It facilitated an understanding of the interaction between the rebar and the surrounding concrete matrix and the influence of environmental factors on corrosion initiation and propagation. The findings from this analysis aided in enhancing the durability of concrete structures.

In a study conducted by Yang et al. (2020), they investigated the influence of applied voltages on the corrosion rate of reinforced steel in a chloride-contaminated environment. The results indicated that higher applied voltages led to an increased corrosion rate of the steel. The paper also discussed the role of voltage in affecting the breakdown of the passive film, corrosion product formation, and the transport of corrosive species, providing insights into the mechanisms by which applied voltages influence the corrosion behavior of reinforced steel.

CHAPTER 3. EXPERIMENTAL PROGRAM

3.1. Accelerated Corrosion on Steel Wires.

3.1.1. Test Procedure

This study aimed to investigate the influence of voltage and chloride ion concentrations on the accelerated corrosion rate of steel bars. The experiment focused on 12-inch steel bars commonly used by pipe manufacturers for reinforcement cages, as illustrated in Figure 5. The experimental setup included electrochemical chloride reactors designed for three different levels of chloride concentration: 2,000 ppm, 30,000 ppm, and 100,000 ppm. Additionally, the experimental setup consisted of five voltage levels and a control condition, as presented in Table 1. The main objective of this investigation was to establish the correlation between voltage, chloride concentration, and accelerated corrosion rate in steel bars.

Figure 5. Wire Coil from Forterra

Table 1. Conducted and Corresponding Number of Specimens

Chloride Solution Concentration	Voltage Level (V)	Number of Samples
2,000 ppm	*Control (No Voltage)*	6
	2	6
	4	6
	8	6
	12	6
	16	6
30,000 ppm	*Control (No Voltage)*	6
	2	6
	4	6
	8	6
	12	6
	16	6
100,000 ppm	*Control (No Voltage)*	6
	2	6
	4	6
	8	6
	12	6
	16	6
		Total: 108

In the initial week of immersion, daily assessments of the samples' weight and diameter were conducted to monitor the progression of corrosion and diameter loss. Afterward, measurements were taken on days 1, 2, 3, 4, 5, 6, 7, and 14 days after immersion. The experimental setup included 18 electrochemical chloride reactors, as depicted in Figure 6, where each reactor consisted of six steel bars functioning as the anode and one copper bar serving as the cathode. The purpose of these measurements and the experimental configuration was to evaluate the samples' corrosion behavior and dimensional alterations throughout the immersion period.

Figure 6. Accelerated Corrosion Test on Rebars

3.1.2. Test Results

Over 14 days, the samples were exposed to various chloride solutions, applied voltages, and retrieved daily. After removing the rust layers using a steel brush, the diameter and weight of the wires were measured. The results of these measurements are presented in Table 2, indicating the remaining weight and diameter of the samples after each daily cleaning procedure. This process was conducted with great care to accurately monitor the alterations in the weight and diameter of the samples over time.

Table 2. Average Remaining Weight and Diameter of Wires at 2,000 ppm

Days	*Control*		*2 V*		*4 V*		*8 V*		*12 V*		*16 V*	
	W(gr)	*D(mm)*	*W(gr)*	*D(mm)*	*W(gr)*	*D(mm)*	*W(gr)*	*D(mm)*	*W(gr)*	*D(mm)*	*W(gr)*	*D(mm)*
0	*100.0*	*100.0*	*100.0*	*100.0*	*100.0*	*100.0*	*100.0*	*100.0*	*100.0*	*100.0*	*100.0*	*100.0*
1	*99.8*	*99.8*	*99.7*	*99.5*	*99.2*	*99.7*	*93.8*	*95.8*	*89.6*	*94.3*	*79.2*	*88.1*
2	*99.8*	*99.6*	*99.5*	*99.0*	*98.3*	*98.4*	*91.4*	*94.4*	*77.0*	*87.4*	*60.2*	*79.4*
3	*99.7*	*99.6*	*99.4*	*98.8*	*96.4*	*97.2*	*88.2*	*92.7*	*74.4*	*85.2*	*31.1*	*73.1*
4	*99.6*	*99.6*	*99.2*	*98.6*	*94.2*	*95.6*	*83.2*	*90.2*	*69.8*	*81.1*	*31.0*	*66.3*
5	*99.5*	*99.4*	*99.1*	*98.4*	*91.2*	*94.2*	*76.8*	*86.9*	*66.1*	*75.5*	*27.8*	*59.0*
6	*99.4*	*99.4*	*98.8*	*98.2*	*88.7*	*93.0*	*70.7*	*83.6*	*58.2*	*69.6*	*17.1*	*33.1*
7	*99.3*	*99.2*	*98.5*	*97.8*	*84.3*	*89.9*	*63.7*	*77.8*	*51.8*	*64.7*	*10.2*	*23.3*
14	*98.8*	*98.6*	*97.1*	*97.1*	*78.0*	*78.9*	*55.1*	*57.4*	*35.2*	*42.6*	*2.1*	*1.6*

The results in Table 2 indicate that at a chloride concentration of 2,000 ppm, the rebars' average remaining weight and diameter subjected to 12 and 16 Volts were less than 50% after a 14-day testing period. Furthermore, it is worth noting that corrosion was observed in almost all the rebars. Figure 7 portrays the rebars' average remaining weight and diameter at 2,000 ppm chloride concentration under different voltage conditions.

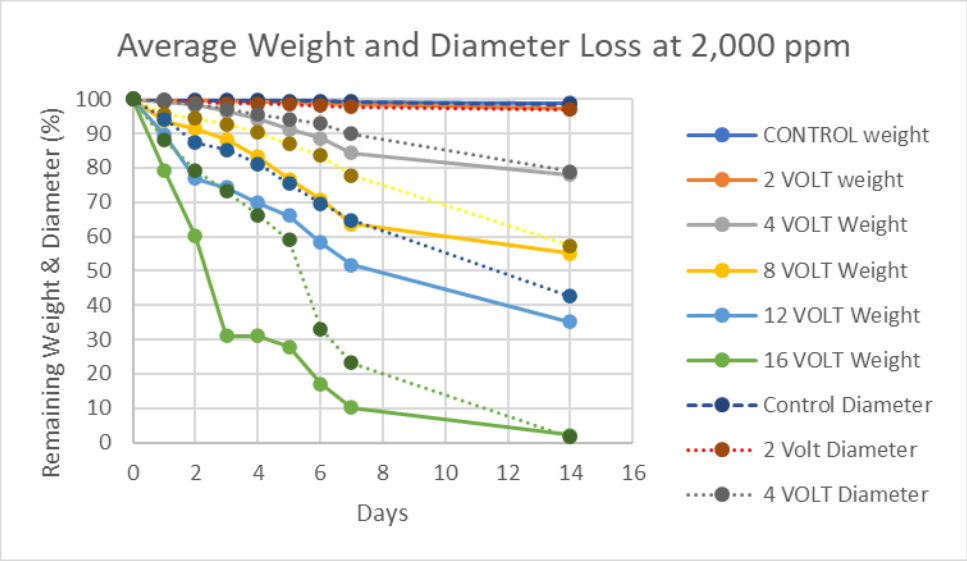

Figure 7. Average Remaining Weight and Diameter at 2,000 ppm

The study's outcomes indicate that at a chloride concentration of 30,000 ppm, the rebars exposed to 16 Volt suffered complete weight loss within six days of testing. Similarly, akin to the results obtained at 2,000 ppm, the remaining weight and diameter of the rebars exposed to 12 Volt were less than 50%. The numerical results are displayed in Table 3.

Table 3. Average Remaining Weight and Diameter of Wires at 30,000 ppm

Days	*Control*		*2 V*		*4 V*		*8 V*		*12 V*		*16 V*	
	W(gr)	*D(mm)*	*W(gr)*	*D(mm)*	*W(gr)*	*D(mm)*	*W(gr)*	*D(mm)*	*W(gr)*	*D(mm)*	*W(gr)*	*D(mm)*
0	*100.0*	*100.0*	*100.0*	*100.0*	*100.0*	*100.0*	*100.0*	*100.0*	*100.0*	*100.0*	*100.0*	*100.0*
1	*99.8*	*99.6*	*99.3*	*99.3*	*99.0*	*99.1*	*90.1*	*95.5*	*86.9*	*93.3*	*75.4*	*87.0*
2	*99.2*	*99.4*	*98.6*	*98.8*	*97.9*	*97.8*	*82.7*	*92.5*	*74.7*	*86.0*	*54.5*	*72.0*
3	*98.5*	*99.1*	*97.8*	*98.6*	*94.9*	*96.6*	*79.3*	*90.4*	*71.4*	*84.2*	*30.4*	*55.5*
4	*98.1*	*98.9*	*97.1*	*98.2*	*92.2*	*94.3*	*75.7*	*87.8*	*63.5*	*81.0*	*15.7*	*27.9*
5	*97.7*	*98.7*	*96.0*	*98.0*	*89.8*	*93.3*	*71.6*	*84.7*	*52.8*	*73.5*	*7.6*	*9.5*
6	*96.9*	*98.5*	*94.8*	*97.6*	*85.9*	*91.9*	*65.1*	*81.6*	*49.1*	*66.8*	*0.0*	*0.0*
7	*96.7*	*98.2*	*93.8*	*97.3*	*82.8*	*87.0*	*62.7*	*76.6*	*43.2*	*58.5*	*0.0*	*0.0*
14	*94.8*	*95.1*	*90.9*	*91.4*	*75.2*	*75.3*	*50.3*	*52.4*	*22.4*	*28.1*	*0.0*	*0.0*

Figure 8 depicts the average remaining weight and diameter of rebars at 30,000 ppm chloride concentration under different voltage conditions.

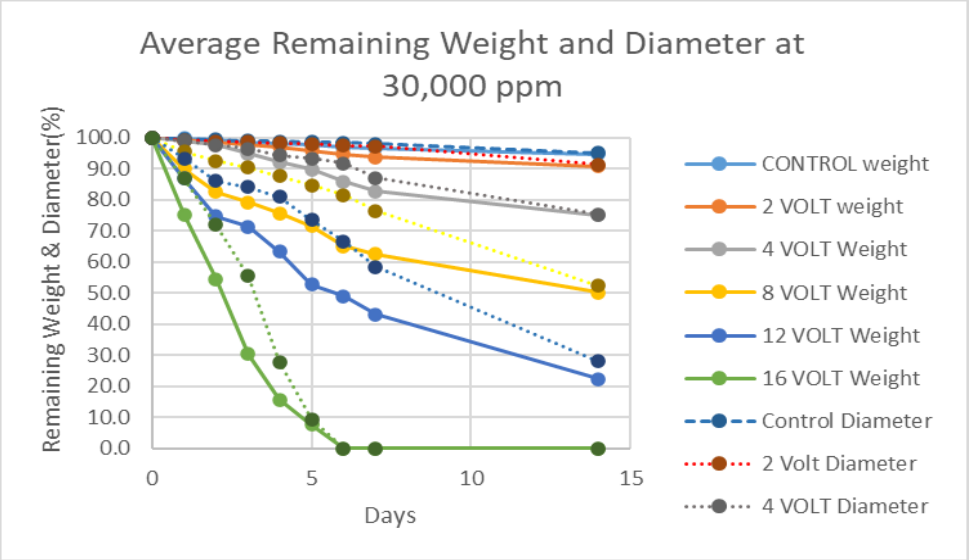

Figure 8. Average Remaining Weight and Diameter at 30,000 ppm

Table 4 displays the outcomes obtained for chloride solutions with a concentration of 100,000 ppm. The results indicate that after four days of testing, no rebars exposed to 16 Volt remained intact, indicating complete corrosion and loss. Similarly, rebars subjected to 12 Volt exhibited significant degradation, with more than 50% corroding and losing weight after five days of testing.

Additionally, wires subjected to 8 Volt also experienced deterioration, as demonstrated by a 50% weight loss after 14 days of testing. These results emphasize rebars' accelerated corrosion and deterioration under the specified voltage and chloride concentration conditions.

Table 4. Average Remaining Weight and Diameter of Wires at 100,000 ppm

Days	*Control*		*2 V*		*4 V*		*8 V*		*12 V*		*16 V*	
	W(gr)	*D(mm)*	*W(gr)*	*D(mm)*	*W(gr)*	*D(mm)*	*W(gr)*	*D(mm)*	*W(gr)*	*D(mm)*	*W(gr)*	*D(mm)*
0	*100.0*	*100.0*	*100.0*	*100.0*	*100.0*	*100.0*	*100.0*	*100.0*	*100.0*	*100.0*	*100.0*	*100.0*
1	*98.5*	*99.1*	*99.0*	*99.0*	*98.3*	*98.9*	*87.4*	*93.5*	*84.0*	*91.6*	*70.7*	*85.1*
2	*97.5*	*98.1*	*97.9*	*97.8*	*95.8*	*97.4*	*80.8*	*90.5*	*72.5*	*85.1*	*46.5*	*69.3*
3	*96.6*	*97.6*	*96.6*	*96.2*	*94.5*	*96.2*	*75.9*	*87.4*	*70.4*	*83.1*	*23.5*	*42.7*
4	*95.3*	*96.8*	*95.1*	*94.8*	*91.8*	*94.2*	*73.3*	*85.0*	*60.5*	*79.3*	*0.0*	*0.0*
5	*94.1*	*95.7*	*93.6*	*93.7*	*89.5*	*93.0*	*68.8*	*82.1*	*49.7*	*72.9*	*0.0*	*0.0*
6	*93.1*	*94.9*	*92.3*	*92.6*	*84.8*	*91.8*	*64.0*	*68.7*	*41.4*	*63.0*	*0.0*	*0.0*
7	*91.6*	*93.7*	*90.8*	*91.0*	*80.6*	*84.1*	*58.7*	*62.6*	*34.6*	*53.5*	*0.0*	*0.0*
14	*89.8*	*90.2*	*85.1*	*85.3*	*69.2*	*70.2*	*45.6*	*48.3*	*17.8*	*18.3*	*0.0*	*0.0*

Figure 9 presents a graphical representation of the rebars' average remaining weight and diameter, which were subjected to different voltage conditions while exposed to a chloride concentration of 100,000 ppm. The figure provides valuable insights into the corrosion behavior and degradation of the rebars under these specific conditions.

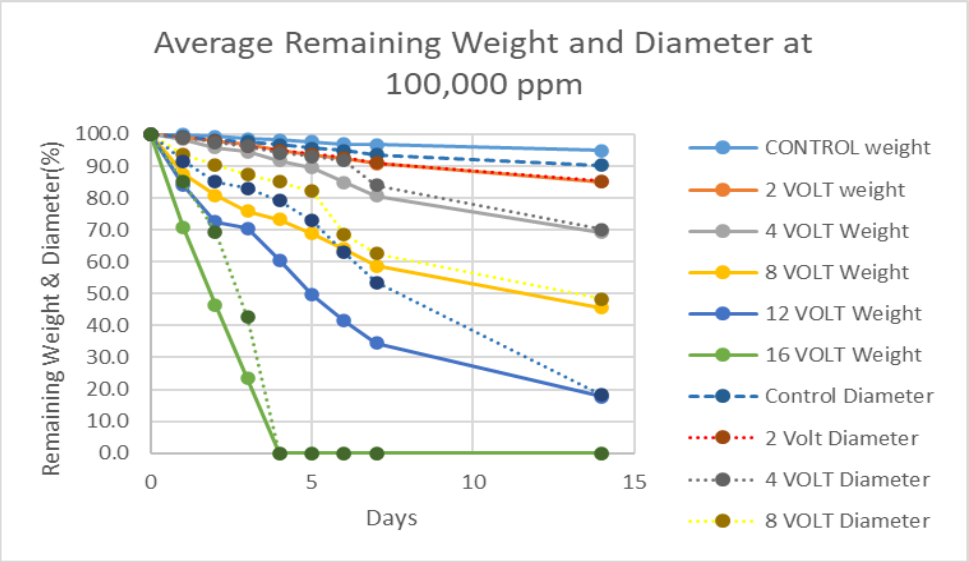

Figure 9. Average Remaining Weight and Diameter at 100,000 ppm

The visual changes observed in the steel bars on the 14th day of the experiment are presented in Figures 10, 11, and 12. Each figure corresponds to a different chloride concentration: 2,000 ppm, 30,000 ppm, and 100,000 ppm, respectively. These figures visually represent the corrosion effects on the steel bars under different voltage conditions.

The corrosion rates of the steel bars varied significantly depending on the voltage applied to the reactor and the chloride concentration level. It was observed that, regardless of the chloride concentration, the steel bars exhibited corrosion and experienced substantial material loss when subjected to 16 Volt before reaching the 14th day of measurement under the 30,000 ppm and 100,000 ppm conditions.

These findings highlight the significant influence of voltage and chloride concentration on the accelerated corrosion behavior of the steel bars.

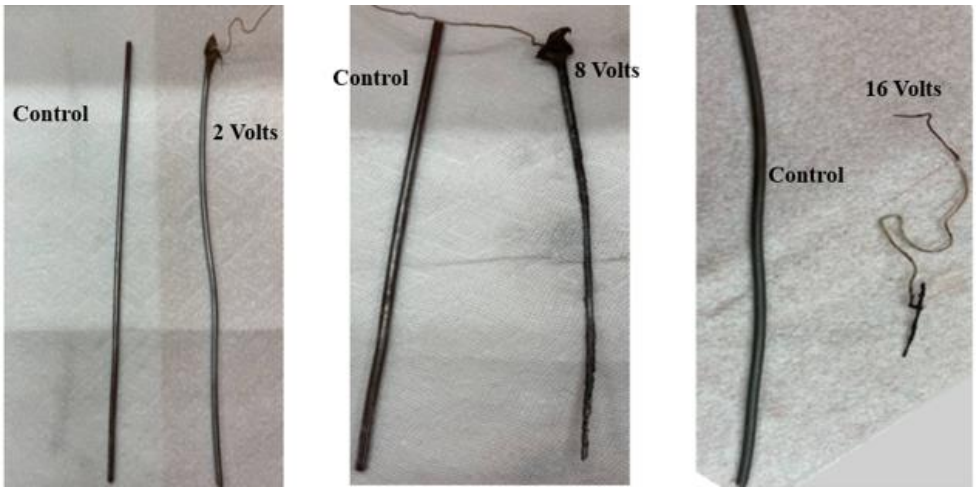

(a) (b) (c)

Figure 10. Corrosion Effects on the Steel Bars Under (a) Control & 2Volts, (b) Control & 8Volts, (c) Control & 16 Volts After 14 Days at 2,000 ppm.

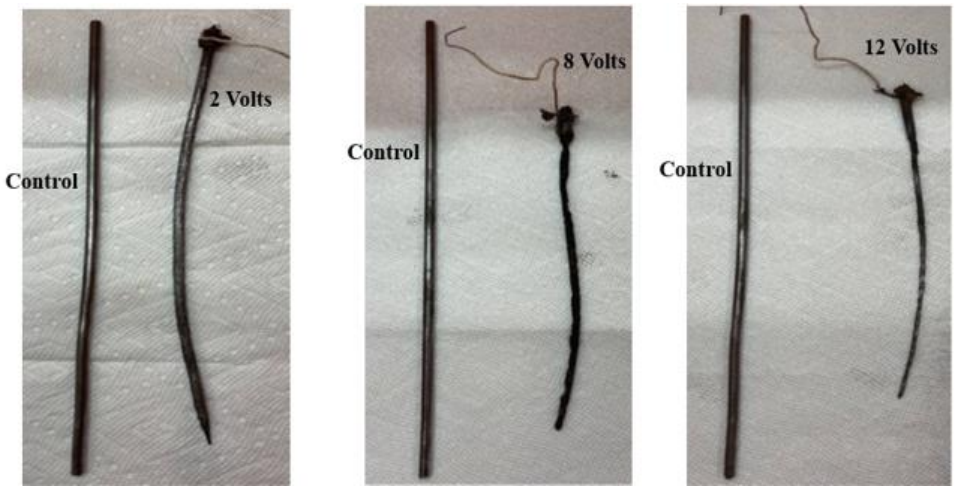

(a) (b) (c)

Figure 11. Corrosion Effects on the Steel Bars Under (a) Control & 2Volts, (b) Control & 8Volts, (c) Control & 12 Volts After 14 Days at 30,000 ppm.

.

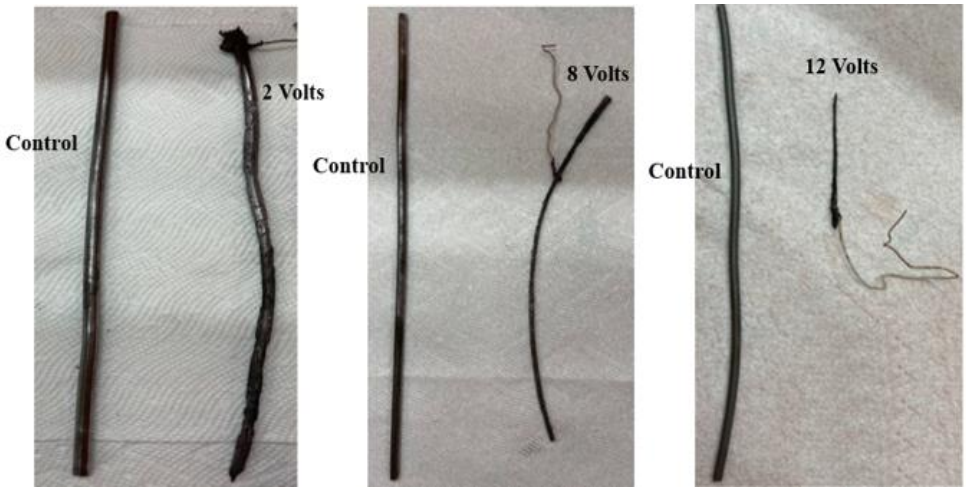

(a) (b) (c)

Figure 12. Corrosion Effects on the Steel Bars Under (a) Control & 2Volts, (b) Control & 8Volts, (c) Control & 12 Volts After 14 Days at 100,000 ppm.

.

These findings emphasize the importance of considering chloride concentration and voltage levels in assessing the accelerated corrosion of rebars. The results provide valuable insights into the performance of the rebar's corrosion under different environmental conditions.

Based on the provided results, several observations and conclusions can be made. So,

1. ***Corrosion Rate***: The corrosion rate of the rebars is influenced by the chloride concentration and the voltage applied. Higher chloride concentrations generally lead to a faster corrosion rate.

2. ***Voltage Impact***: In general, increasing the voltage accelerates the corrosion process. Rebars subjected to higher voltages, particularly 12 and 16 Volts, exhibited more significant weight loss and corrosion than those subjected to lower voltages.

3. ***Chloride Concentration Effect***: The corrosive effect of chloride ions becomes more pronounced as the concentration increases. Rebars subjected to higher chloride

concentrations, such as 30,000 ppm and 100,000 ppm, experienced more rapid degradation and weight loss.

4. ***Corrosion Progression***: Throughout the testing period, the remaining weight and diameter of the rebars decreased gradually. The rate of degradation varied depending on the chloride concentration and voltage applied.

5. ***Critical Thresholds***: There are critical thresholds at which rebars reach a point of severe corrosion and weight loss. For example, rebars subjected to 12 Volt at 2,000 ppm exhibited significant corrosion after 14 days, while rebars subjected to 16 Volt at 30,000 ppm and 100,000 ppm lost all their weight within a few days.

Comparing the results between different chloride concentrations and voltage levels allows for finding the critical corrosion condition that leads to rapid degradation.

3.1.3. SEM & EDX

Scanning Electron Microscopy (SEM) and Energy Dispersive X-ray spectroscopy (EDX) are widely utilized techniques for the microscopic analysis of specimens in various scientific disciplines (Gupta and Singh, 2020). SEM offers the advantage of capturing high-resolution magnified microstructure images, enabling detailed visualization of the sample's surface morphology (Goldstein et al. 2017). Using a focused electron beam, SEM scans the sample's surface and generates signals that carry valuable information about the sample's composition and structure (Kawasaki et al., 2018). Modern SEM machines predominantly utilize secondary electrons to construct images with enhanced contrast and resolution.

In parallel, EDX is a complementary analytical technique to SEM, enabling the investigation of specimens' chemical composition and elemental analysis. By integrating an additional detector

into the SEM chamber, EDX detects the presence of various materials on the surface of the specimens and provides valuable insights into their mass and distribution. It is worth noting that applying a higher voltage during EDX analysis maximizes the efficiency and accuracy of the probing process.

The application of SEM and EDX to study the progression of oxidation on the surface of steel rods has yielded significant findings. Figures 14-18 in the accompanying documentation portray the evolution of oxidation in the control specimen (without voltage) and the specimens subjected to different voltages. Additionally, Figure 13 showcases the results of surface spectroscopy, effectively illustrating the formation of oxide on the surface of the examined specimens.

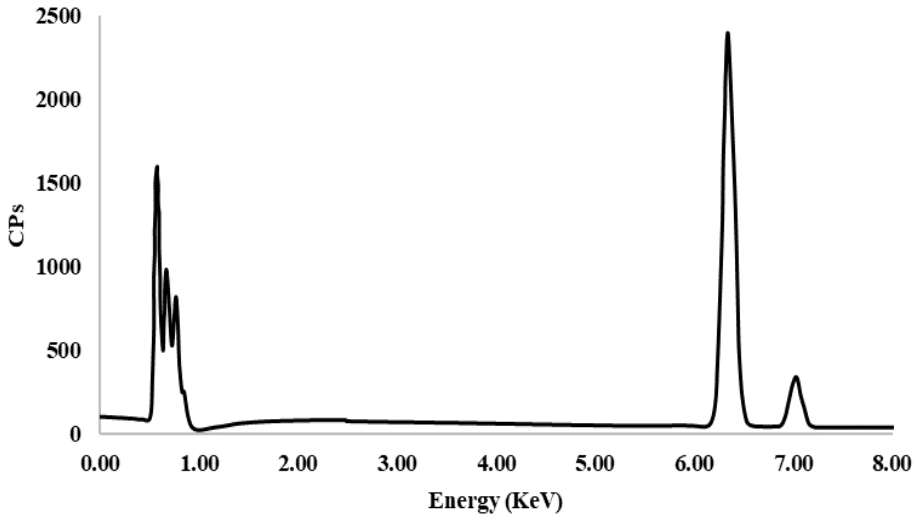

Figure 13. Oxidation Level of Surface in EDX Results.

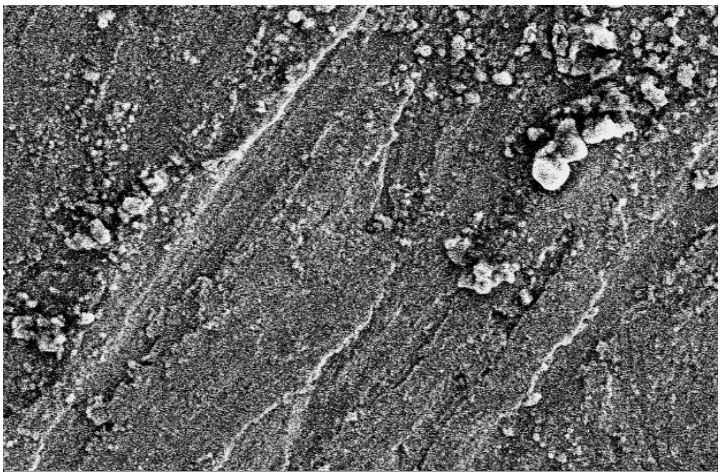

Figure 14. Microscopic Surface Image of Specimens at Control With 500x Magnification.

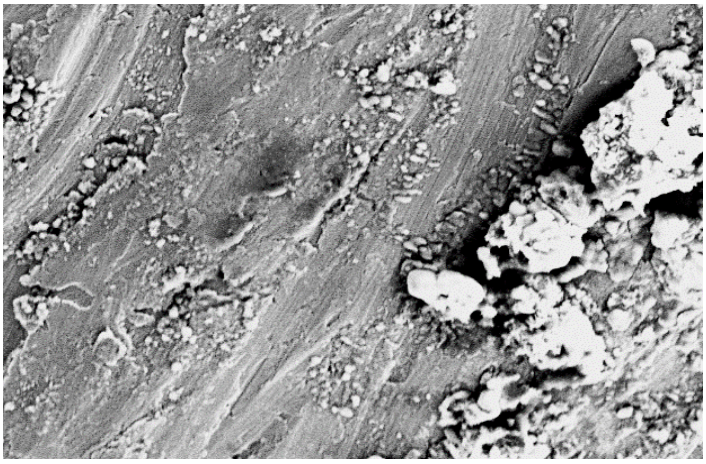

Figure 15. Microscopic Surface Image of Specimens at 2 Volt With 500x Magnification.

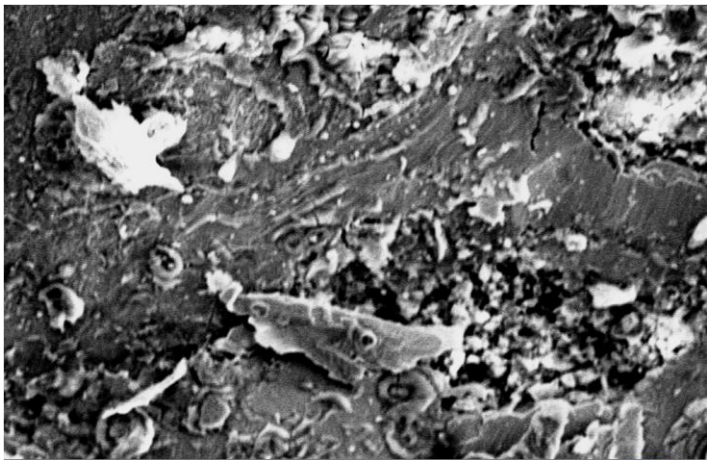

Figure 16. Microscopic Surface Image of Specimens at 4 Volt With 500x Magnification.

Figure 17. Microscopic Surface Image of Specimens at 8 Volt With 500x Magnification.

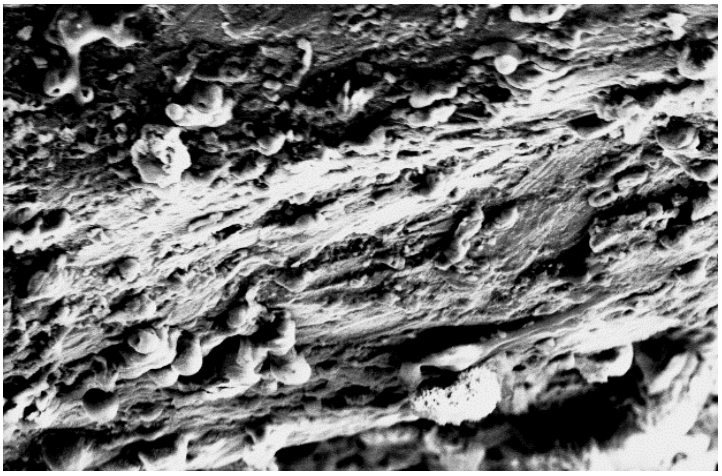

Figure 18. Microscopic Surface Image of Specimens at 12 Volt With 500x Magnification.

In Figure 19, the relationship between the applied voltage and the steel content at the surface of the specimen is depicted. It is evident from the figure that an increase in the applied voltage leads to a reduction in the amount of steel present at the surface. Simultaneously, the corresponding increase in oxygen detected at the sample's surface indicates a higher degree of oxidation. This finding suggests a direct correlation between the applied voltage, the reduction of steel content, and the increase in oxidation levels.

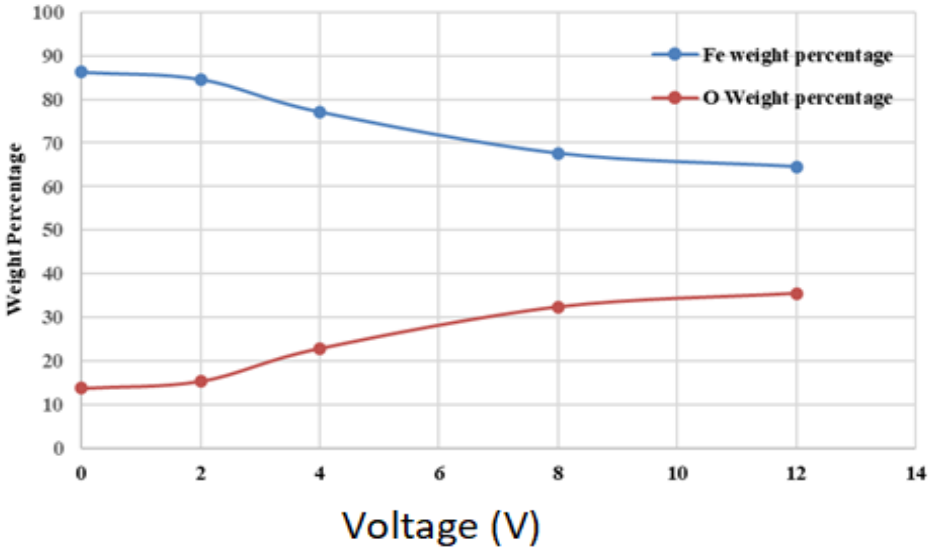

Figure 19. Change of the Weight of Iron and Oxygen at the Sample's Surface.

3.2. Accelerated Corrosion of Bars Embedded in Concrete Cylinders

3.2.1. Overview

This experimental procedure aims to assess the impact of accelerated corrosion on steel bars embedded within concrete cylinders measuring 6 inches by 12 inches. The cylinders were fully immersed in chloride solutions of varying concentrations. The cylinders will be notched perpendicular to the embedded bars to simulate a crack commonly observed in Reinforced Concrete Pipe (RCP), as depicted in Figure 20. Considering the outcomes of the preliminary investigation conducted on bare wires, three electrical potentials of 2 Volt, 4 Volt, and 8 Volt were employed. These voltage levels have been determined to induce reasonable rates of accelerated corrosion in the presence of chloride concentrations at 2,000 ppm, 30,000 ppm, and 100,000 ppm. Selecting these specific voltages and chloride concentrations ensures that the reactions will neither result in excessively rapid nor extremely slow corrosion rates. Furthermore, to account for the influence of wire size variations, an additional set of cylinders with steel reinforcement

corresponding to wire sizes used in 96-inch (0.226 inches diameter) will be subjected to an applied voltage of 8 Volt.

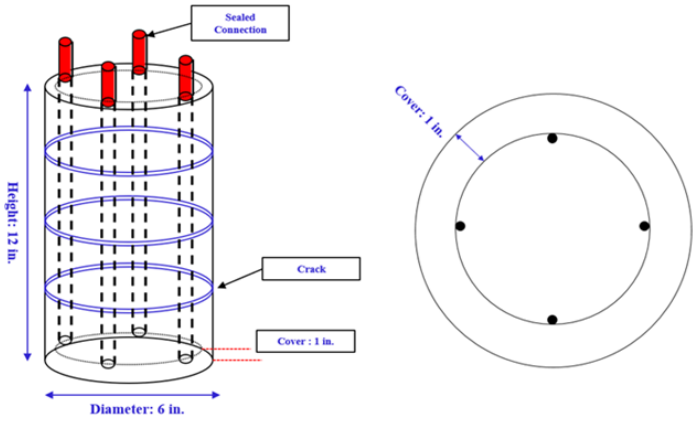

Figure 20. Steel Bars Embedded in a Concrete Cylinder with a Crack.

The concrete mix design will be carefully selected to meet a specific compressive strength requirement of 5,000 psi. The test schedule is outlined in Table 5. In order to examine the impact of crack widths on the corrosion rate, four different levels of crack widths were considered: 0.01, 0.03, 0.05, and 0.1 inches.

To assess the corrosion state of the embedded steel, Half-Cell Potentials were recorded following ASTM C876. This will provide valuable information about the extent of corrosion. Additionally, the wires' corresponding weight loss values were measured monthly for six (6) months. This data helps to determine the degree of corrosion experienced.

Furthermore, Scanning Electron Microscopy (SEM) and Energy Dispersive X-ray spectroscopy (EDX) analyses were conducted on the samples. These analyses allowed for a quantitative assessment of the levels of corrosion and oxidation present in each sample. These techniques provide insight into corroded materials' microscopic characteristics and elemental composition.

Table 5. Test Schedule and the Corresponding Numbers of Cylinder Specimens

Chloride Solution Concentration	Voltage Level (V)	Number of Required Concrete Cylinders
2,000 ppm Wire Size for 24 inches. Pipe	*Control (No Voltage)*	*72*
	2	*72*
	4	*72*
	8	*72*
2,000 ppm Wire Size for 96 inches. Pipe	*8*	*72*
30,000 ppm Wire Size for 24 inches. Pipe	*Control (No Voltage)*	*72*
	4	*72*
	8	*72*
	8	*72*
30,000 ppm Wire Size for 96 inches. Pipe	*8*	*72*
100,000 ppm Wire Size for 24 inches. Pipe	*Control (No Voltage)*	*72*
	2	*72*
	4	*72*
	8	*72*
100,000ppm Wire Size for 96 inches. Pipe	*8*	*72*
		Total: 1,080

3.2.2. Scope and Goals

The overall testing plan for this study involves evaluating the effects of different crack sizes, chloride concentrations, and applied voltages on the corrosion behavior of the concrete specimens. Combining these factors will allow for a comprehensive analysis of the corrosion performance. Here is a summary of the overall testing plan:

Crack Sizes: Four different crack sizes were considered: 0.01", 0.03", 0.05", and 0.1". These crack sizes mimic the typical cracks found in reinforced concrete pipes.

Chloride Concentrations: Three different chloride concentrations were used: 2,000 ppm, 30,000 ppm, and 100,000 ppm. These concentrations represent varying levels of chloride exposure that concrete specimens may experience in real-world scenarios.

Applied Voltages: Three different voltages will be applied to the specimens: 2 Volt, 4 Volt, and 8 Volt. These voltages have been determined to yield reasonable accelerated corrosion rates for the given chloride concentrations.

3.3. Autogenous Healing

Autogenous healing is the phenomenon that occurs when hairline cracks that develop in concrete repair themselves through reactions with constituents in water and the paste. The impact of this phenomenon on steel corrosion needs to be evaluated to isolate corrosion due to electrical current. Water chemistry determines whether the crack heals autogenously, thus limiting the potential for corrosion. Autogenous healing is mainly produced by continuing hydration or carbonation. This phenomenon might affect the service life prediction using the accelerated corrosion test. In an accelerated test, rebars deteriorate quickly, while autogenous healing takes longer. The repair is done by mechanical blocking by particles carried into the crack with the water and the deposition of calcium carbonate from the cementitious material. The well-known practical phenomenon of autogenous healing in cracks significantly concerns the functional reliability of structures subjected to water pressure loads. Due to autogenous healing, the water flow through the cracks gradually reduces with time, and in extreme cases, the cracks seal completely.

Principle of Autogenous Self-Healing of Concrete

The process of autogenous healing is higher in the early stages of concrete strength gain as it is the period when there is a more substantial content of un hydrated cement. This phase involves compressive strength gain and wet-dry cycles that further improve the healing performance of concrete. The primary healing process in autogenous self-healing of a matured concrete is the crystallization of calcium carbonate within the crack. The process can be explained; carbonates are obtained when carbon dioxide in the atmosphere dissolves in water.

$$H_2O+CO_2 \leftrightarrow H_2CO_3 \leftrightarrow H^+ + HCO_3^-$$

These carbonates react with the calcium in the concrete to form calcium carbonates. The main five reasons why concrete undergoes autogenous self-healing are:

a) The reaction of un hydrated cement particles present in the concrete.

b) The expansion of concrete in the crack flanks

c) The crystallization of calcium carbonates

d) The cracks are filled with fine particles that are present in the water.

e) The loose particles resulting from cracking, close the cracks.

The variations in concrete mix designs or production methods are another factor that contributes to the result of the study.

The amount of cementitious material in concrete varies between manufacturers, which might be necessary when comparing the impact of autogenous healing. Thus, 72 additional cylinders with reinforcing wire were fabricated with 0.01 in., 0.03 in., and 0.05 in. cracks with two cementitious

contents. The cementitious content for this test will correlate with the current practice of the manufacturers. Table 6 shows this test's schedule and the corresponding number of concrete cylinders. Each cylinder will be tested monthly for six months using Microscope Crack measurements and a sensitive Caliper to measure crack closure.

Table 6. Test Schedule and the Corresponding Number of Cylinder Specimens for Autogenous Healing

Cementitious Content	Crack Width (in.)	Number of Required Concrete Cylinders
Low Cement Ratio	*0.01*	*12*
	0.03	*12*
	0.05	*12*
High Cement Ratio	*0.01*	*12*
	0.03	*12*
	0.05	*12*
		Total: 72

3.4. Test Methodology

3.4.1. Half-Cell Potential

The testing parameters will include measuring the Half-Cell Potentials according to ASTM C876 to assess the corrosion state of the embedded steel. The weight loss of the wires will be measured monthly for up to six (6) months to quantify the level of corrosion.

The Half Cell Potential (HCP) method has gained recognition due to its practical applicability in the field and its establishment of clear criteria for assessing the probability of corrosion. The testing procedure for half-cell potential is outlined in ASTM C-876, which serves as the Standard Test Method for Corrosion Potentials of Uncoated Reinforcing Steel in Concrete. The designated test area must be electrically connected to ensure accurate results and may require pre-wetting.

The measurements obtained from half-cell potential readings provide valuable insights into the relative likelihood of corrosion. At the same time, the assessment of resistivity indicates the relative susceptibility of the system to corrosion. Even if the resistivity is high, indicating a less conductive environment, corrosion can still occur, albeit slower. Conversely, lower resistivity values suggest a higher probability of accelerated corrosion. Figure 21 illustrates the schematic testing procedure of the Half-Cell Potential method.

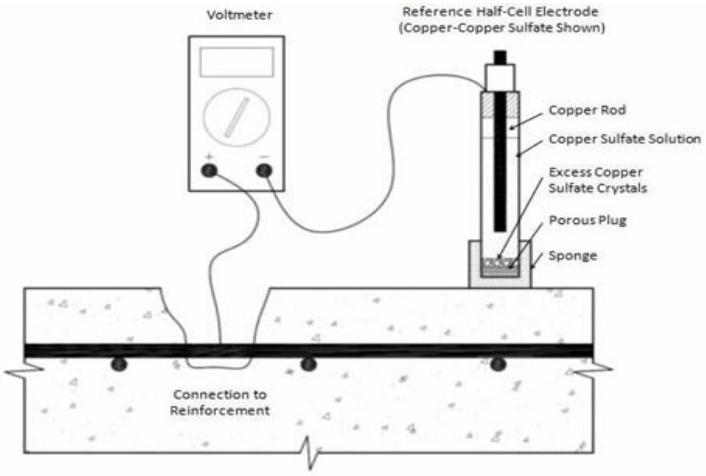

Figure 21. Schematic of Half-Cell Potential Testing (Piyush et al. 2016)

The test is based on the principle that the electrical potential of the steel electrode changes depending on its corrosion state. A more negative potential indicates a higher likelihood of active corrosion, while a more positive potential suggests a more passive or non-corroding state.

A reference electrode (typically a copper/copper sulfate electrode) is placed on the concrete surface during the test. In contrast, a probe electrode (a silver/silver chloride electrode) is connected to the embedded steel. The potential difference between the two electrodes is measured using a Voltmeter. In the experimental setup, illustrated in Figure 22a, a cell is depicted wherein each side is referred to as a half-cell. Each half-cell comprises an electrode immersed in an electrolyte

solution, and both half-cells are interconnected. Due to a difference in corrosion tendencies, one of the electrodes, known as the anode, undergoes oxidation and donates electrons. A reference electrode with a known potential is required to apply this concept to concrete and interpret corrosion potential results. This reference electrode is connected to the other half-cell, represented by the embedded rebar in Figure 22b. Establishing a connection between the reference electrode and the reinforcing steel and placing it on the concrete surface makes it possible to measure the potential difference between the two half-cells. This measurement aids in evaluating the corrosion potential of the concrete system.

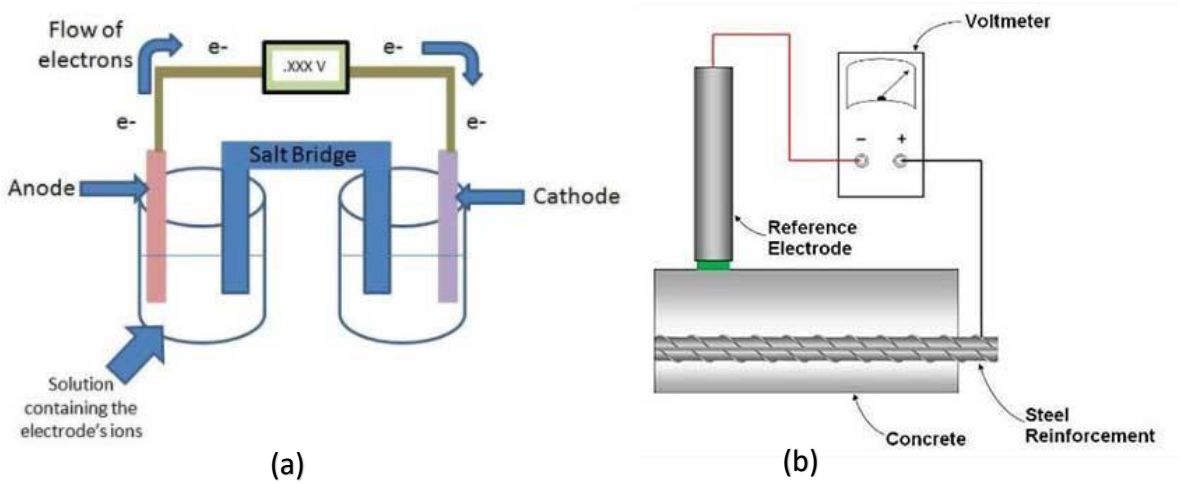

Figure 22. (a) Anode and Cathode Cells, and (b) Setup of Half-Cell Potential Measurement. (GIATEC Web, 2023)

ASTM C876 is a valuable resource for conducting measurements using the Half Cell Potential method, outlining the procedures, and establishing a correlation between the measured potential values and the likelihood of corrosion. The interpretation of the results obtained through this method is qualitative and relies on using a copper sulfate electrode (CSE) as a reference.

To aid in interpreting the measured potential values, ASTM has proposed a general guideline, presented in Table 7. This guideline categorizes the measured potential ranges into three distinct

categories, indicating the corrosion probability associated with each range. The categories include a greater than 90% chance of corrosion, a less than 10% chance of corrosion, or an uncertain chance of corrosion.

Table 7. Potential Measured Values (mV) and Corrosion Probability (Adapted from ASTM C876)

Measured Potential (mV CSE)	Probability of Steel Corrosion Activity
>-200	Less than 10%
-200 to -350	Uncertain
<-350	More than 90%

Measuring Principle

Under normal circumstances, the reinforcement steel in concrete structures is shielded from corrosion through a thin, protective layer known as the hydrated iron oxide passive film. However, this passive film can be compromised by certain factors. One such factor is carbon dioxide (CO2) in the atmosphere, which can cause the film to break down through carbonation. Additionally, the penetration of aggressive substances, particularly chlorides from de-icing salt or saltwater, can also lead to the degradation of the passive film.

In the presence of corrosion-inducing conditions, an electrochemical process occurs. At the anode, ferrous ions (Fe^{++}) are dissolved into the surrounding environment while electrons are released. These electrons then migrate through the steel to the cathode, combining water and oxygen to form hydroxide ions (OH^-). This electrochemical reaction generates a potential difference, which can be quantified using the half-cell method.

The half-cell method involves using a reference electrode with the corroding steel surface. The level of corrosion activity can be determined by measuring the potential difference between the reference electrode and the steel. This method is a valuable tool for assessing the corrosion status

of reinforced concrete structures and aiding in developing appropriate maintenance and repair strategies. Figure 23 depicts the principle of steel corrosion in concrete.

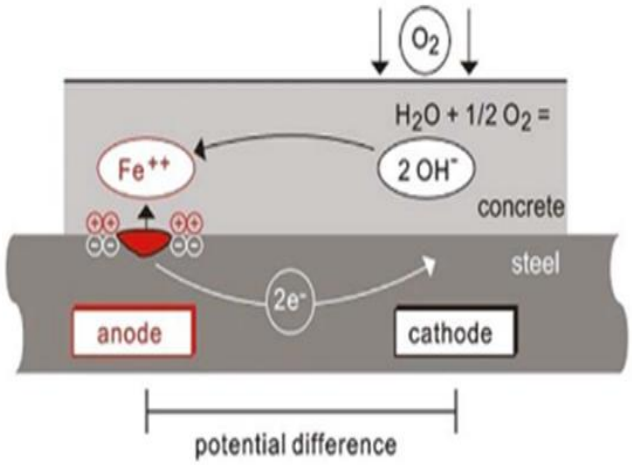

Figure 23. Principle of Steel Corrosion in Concrete with Oxygen Availability (Proceq Profometer Operation Instructions)

The fundamental concept of potential field measurement is to assess the corrosion state of steel reinforcement within the concrete by measuring potentials at the surface. This approach employs a reference electrode connected to the steel reinforcement through a high-impedance Voltmeter and systematically traverses over the concrete surface in a grid pattern.

The reference electrode in the Profometer Corrosion system is a half-cell of copper (Cu) immersed in a saturated copper sulfate ($CuSO_4$) solution. This configuration ensures a constant and well-defined potential. The copper rod is the electrode, while the saturated copper sulfate solution maintains the desired potential. By comparing the potentials measured at different points on the concrete surface with the reference electrode, valuable information regarding the corrosion condition of the steel reinforcement can be obtained.

The Proceq Profometer Corrosion is designed to evaluate the corrosion of reinforced concrete structures. The Profometer Corrosion utilizes the Half-Cell Potential method to assess the corrosion activity on reinforcing steel bars within concrete. It measures the electrical potential difference between the reinforcement and a reference electrode to determine the likelihood of corrosion. Additionally, it provides corrosion rate measurements based on the polarization resistance technique. By mapping the half-cell potential and measuring corrosion rates at various locations on the concrete surface, the Profometer Corrosion helps identify areas prone to corrosion. It assists in assessing the overall corrosion condition of the reinforced concrete structure, as illustrated in Figure 24.

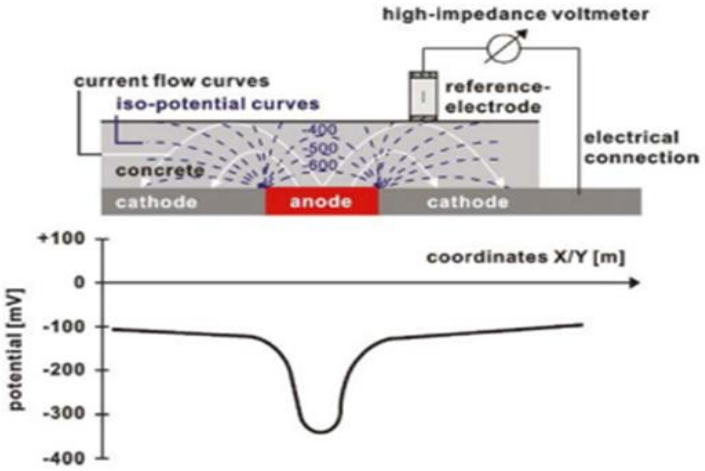

Figure 24. Measuring Principle (Proceq Profometer Operation Instructions)

By referring to this guideline, the corrosion probability of the tested concrete system can be qualitatively assessed based on the measured potential values, aiding in the evaluation and decision-making process regarding corrosion prevention and mitigation strategies.

The Profometer Corrosion has various electrode options, including the primary electrode (rod or wheel) that utilizes a Copper/Copper sulfate half-cell. Additionally, the instrument offers unique

one-wheel and four-wheel electrodes, enhancing productivity for measuring large areas. The Profometer Corrosion offers immediate on-site data interpretation with its corrosion scan and statistical views. The instrument allows for customizable and cumulative distribution views and chipping graph views. These features aid in the on-site mapping of the corrosion potential in the reinforced concrete structure.

Figure 25. Proceq Profometer

Figure 25 depicts the Proceq Profometer. This instrument is utilized for corrosion analysis based on the half-cell method, facilitating the identification of active corrosion in reinforced concrete structures.

The Rod Corrosion Electrode is an essential component for the Profometer Corrosion Meter, facilitating the accurate detection of active corrosion within steel-reinforced concrete structures through the half-cell method. The Rod Corrosion Electrode includes a copper sulfate and a cap with a wooden plug. Rod Electrodes are typically employed for individual corrosion readings or when implementing a manually defined grid pattern. These electrodes offer a versatile approach

to corrosion analysis, allowing for precise measurements in various scenarios. Figure 26 visually represents the specific design and appearance of the rod electrode.

Figure 26. Rod Corrosion Electrode

Several factors should be considered when interpreting Half-Cell Potential data to ensure accurate and meaningful results. The following steps are crucial in the interpretation process:

1. Identify the location of the reinforcing bars within the concrete structure. This information is necessary for making proper connections and obtaining reliable measurements.
2. Establish a connection with the reinforcement. Multiple connections may be required if discontinuities or multiple reinforcement layers are present.
3. Prepare the concrete surface by wetting it. This step ensures proper electrical contact and improves the accuracy of the potential readings.

It is important to note that various factors can influence the Half-Cell Potential readings and shift the measured potentials toward more positive or negative values. These factors include the condition of the concrete (dry or wet), the presence of chloride ions, the absence of oxygen at the rebar surface (due to saturation), the concrete cover's thickness, the concrete's resistivity, and the temperature. These influences are summarized in Table 8. Considering these factors, interpreting Half-Cell Potential data can become challenging, mainly when using the guidelines provided in ASTM C876, especially within the uncertain measurement ranges.

Table 8. Typical Ranges of Half-Cell Potential of Rebars in Concrete (Adopted from RILEM TC-154,2003)

Conditions	Potential Values (mV/CSE)
Humid, Chloride-Free Concrete	*-200 to +100*
Wet, Chloride-Contaminated Concrete	*-600 to -400*
Water-Saturated Concrete Without Oxygen	*-1000 to -900*
Humid, Carbonated Concrete	*-400 to +100*
Dry, Carbonated Concrete	*0 to +200*
Dry Concrete	*0 to +200*

Therefore, it is essential to carefully analyze the collected data, considering the specific conditions and factors influencing the measurements. Consulting experienced professionals and considering additional testing methods may be necessary to ensure accurate interpretation and reliable assessments of corrosion probability in the given concrete system.

3.4.2. Scanning Electron Microscope

Scanning Electron Microscopy (SEM) is a powerful imaging technique widely used for analyzing and characterizing materials, including studying corrosion. SEM provides high-resolution, detailed images of the surface morphology and microstructure of materials. It offers valuable insights into the corrosion processes, such as the formation of corrosion products, the extent of surface degradation, and the morphology of corrosion features.

The SEM instrument comprises an electron source, electromagnetic lenses, a sample chamber, and detectors. In SEM, a beam of electrons is generated and focused onto the sample surface. The electrons interact with the atoms in the sample, resulting in the emission of various signals.

Secondary electrons (SE) are low-energy electrons emitted from the sample's surface due to interacting with the incident electron beam. These secondary electrons are collected by a detector, forming the primary image in SEM. SE imaging provides topographical information, highlighting surface features and variations in height or texture.

Backscattered (BSE) are high-energy electrons that undergo scattering when interacting with the sample's atoms. The intensity of the backscattered electrons depends on the atomic number of elements in the sample. BSE imaging provides compositional contrast, differentiating different materials or phases within the sample.

When applied to the study of corrosion, SEM can provide insights into the morphology and extent of corrosion damage, the presence of corrosion products, and the mechanisms involved in the degradation of materials. It can help identify localized corrosion phenomena such as pitting, crevice corrosion, or intergranular attack. SEM analysis can also be used to evaluate the effectiveness of corrosion protection measures and the performance of different materials or coatings in corrosive environments.

3.4.3. Energy Dispersive X-Ray

Energy Dispersive X-ray spectroscopy (EDX) is a valuable analytical technique for studying steel corrosion. EDX is often employed with Scanning Electron Microscopy (SEM) to investigate the chemical composition and elemental analysis of corrosion products and surface deposits on steel. EDX works by detecting characteristic X-rays emitted by the sample when bombarded with an

electron beam. These X-rays are emitted due to the interaction between the incident electrons and the atoms in the sample. The emitted X-rays have specific energies characteristic of the elements present in the sample. By measuring the energy and intensity of these X-rays, EDX can determine the elemental composition of the corrosion products and surface deposits.

When applied to steel corrosion studies, EDX analysis can provide insights into the types and distribution of elements in corrosion products. It can help identify corrosion-inducing elements such as chlorides, sulfides, or carbonates and the composition of protective layers or passive films that may form on the steel surface. EDX analysis can also investigate the fundamental changes during the corrosion process. Furthermore, EDX mapping can be performed to visualize the distribution of specific elements across the surface of the steel. This mapping technique can provide valuable information on the localization of certain elements or the formation of corrosion products in specific steel regions.

In the context of Energy Dispersive X-ray Spectroscopy (EDX) machines, crucial aspects of spectroscopic analysis are denoted by the terms "KLM lines" and "keV." The KLM lines signify characteristic X-ray emission lines arising from electron transitions between energy levels within an atom. These lines are named after the atomic shells implicated in the transitions, namely, K, L, and M. Notably, the KLM lines correspond to transitions involving electrons situated in the innermost electron shells of an atom.

The most significant KLM lines are the Kα and Kβ lines. The Kα line originates from an electron transitioning from the L shell to the K shell, while the Kβ line entails transitioning from the M shell to the K shell. These lines exhibit distinct energy signatures that are intrinsic to the analyzed element. Leveraging the capacity to detect and quantify the energy of these characteristic X-rays, EDX machines enable the identification of elements present in a given sample.

Furthermore, the unit "keV" signifies kilo-electron Volts, serving as a standard measure of energy in EDX spectroscopy. This unit quantifies the energy of X-rays emitted during electron transitions within the atomic structure. In an EDX spectrum, the X-axis typically represents the energy of the detected X-rays, expressed in keV.

The energy of the X-rays manifests a correlation with the atomic structure of the elements constituting the sample. Each element displays distinctive X-ray energy levels, leading to discernible peaks in the EDX spectrum. By scrutinizing the positions and intensities of these peaks, researchers can accurately ascertain the sample's elemental composition. Figure 27 shows the SEM machine that was used in this project.

Figure 27. SEM & EDX Machine

3.4.4. Crack Measuring Microscope

The crack measuring microscope is a meticulously crafted instrument designed specifically for precise crack measurements in concrete. This sophisticated microscope offers high-definition imaging capabilities and is equipped with an adjustable light source to accommodate varying

lighting conditions. To focus on the image, the microscope features a knurled knob on its side, allowing for precise adjustments. The eyepiece scale can also be rotated 360 degrees to align with the crack's direction. The measurement scale for crack width, which spans approximately 0.1575 inches (or 5/32 inches), is displayed on a lower scale. This scale is divided into 0.00787-inch increments (or 1/128 inches), further enabling precise and accurate crack width measurements. The microscope is in a sturdy wooden case for easy storage and transportation. Figure 28 depicts the specialized microscope for measuring crack sizes in autogenous healing samples. This microscope is designed to measure crack dimensions accurately and precisely in self-healing concrete.

Figure 28. Crack Measuring Microscope

3.5. Material Properties

3.5.1. Concrete

This study involved the creation of two wet mix designs as part of the project. Both designs incorporated a combination of materials. Specifically, they were wet mix designs characterized by different cement ratios: one design featured a high cement ratio, while the other utilized a low

cement ratio. The high cement ratio was employed in constructing all cylinders, while the cylinders intended for autogenous healing were prepared using the low cement ratio.

The materials used in both mix designs include:

Holcim Type I-L Cement from Midlothian, TX: This cement variety, manufactured by Holcim, was obtained from their facility in Midlothian, Texas. It served as a primary binding agent in the mix designs.

EM Eco Materials Pozzolanic Slag from Jewett, TX: The pozzolanic slag supplied by EM Eco-Materials, located in Jewett, Texas, was included in the mix designs. This material possesses pozzolanic properties that enhance the performance and durability of concrete.

Hanson Bridgport CR Limestone 3/4": Hanson, a supplier of construction materials, provided limestone sourced from Bridgport, which was crushed to a particle size of 3/4". This limestone aggregate was incorporated into the mix designs for structural strength and stability.

Hanson Bristol Pea Gravel: Another material supplied by Hanson was the Bristol pea gravel. This rounded, small-sized gravel was utilized in the mix designs to enhance workability and improve the overall performance of the concrete.

Hanson Bristol Natural Sand: The Bristol natural sand was also provided by Hanson as an exemplary aggregate component in the mix designs. Its inclusion helped to achieve the desired consistency and workability of the concrete.

Sika Plastocrete 161: Sika Plastocrete 161, a product from Sika, was used as an admixture in the mix designs. This admixture aids in improving the workability and cohesiveness of the concrete, enhancing its overall performance.

Sika SVC 1,000 Super: Sika SVC 1,000 Super, another admixture from Sika, was incorporated into the mix designs. This admixture provides high early strength to the concrete, enabling faster development of strength properties.

Sika Set NC-4 Accelerator: Sika Set NC-4 Accelerator, also provided by Sika, was included as an admixture in the mix designs. This accelerator promotes the rapid setting and early strength development of the concrete.

The primary objective of this investigation was to examine whether the increased cementitious content in the high cement ratio design resulted in a more significant, similar, or lesser potential for autogenous healing.

The proportions of each material in the concrete mix design were determined with careful consideration of the desired characteristics. The provided proportions are based on one cubic yard (SSD) batch and may be subject to adjustment and optimization following specific project requirements. The primary objective of the mix design is to achieve a target strength of 5,000 psi in 28 days. It is crucial to highlight that all the concrete materials used in this mix design have been approved by Rinker and are supplied by Forterra, ensuring their compliance with quality standards. Table 9 presents the proportions of the concrete mix design with a high ratio of cement:

Table 9. Proportions of Concrete Mix Design with High Cement Ratio

Material	The portion at one cubic yard (SSD wt.)	Units @ One Cubic Yard (SSD wt.)
Type I-L Cement	*700*	*Lbs*
Limestone	*1,620*	*Lbs*
Natural Sand	*1,501*	*Lbs*
Water	*243*	*Lbs*
Sika Plastocrete	*3-6*	*Fl. Ozs/100 cmt*
Sika SVC 1000 Super	*6-14*	*Fl. Ozs/100 cmt*
Sika Set NC-4 Accelerator	*10-20*	*Fl. Ozs/100 cmt*
Total	*4,069*	*Lbs*

In this mix design, the water-to-cement (w/c) ratio is 0.354, indicating the proportion of water relative to the cement content. The air pressure requirement for the concrete is set at 1.5% with a tolerance of ±0.5%. The desired slump, a measure of concrete consistency, is approximately 7 inches with a tolerance of ±2 inches. Additionally, the unit weight of the concrete mix is targeted to be 150.7 pounds per cubic foot.

These specifications are essential factors considered in the mix design to ensure the desired performance and characteristics of the concrete. The w/c ratio influences the strength and workability of the concrete, while the air pressure requirement controls the air content to enhance durability. The slump requirement indicates the concrete's workability and ease of placement. Finally, the unit weight determines the density and structural properties of the hardened concrete. Table 10 illustrates the mix design proportions with a low cement ratio, designed to achieve a target strength of 5,000 psi at 28 days. The mix design incorporates adjustments to the water-to-cement (w/c) ratio, air content, slump, and unit weight to meet specific requirements.

Table 10. Proportions of Concrete Mix Design with Lower Cement Ratio

Material	The portion at one cubic yard (SSD wt.)	Units @ One Cubic Yard (SSD wt.)
Type I-L Cement	*547*	*Lbs*
Limestone	*1,670*	*Lbs*
Natural Sand	*1,626*	*Lbs*
Water	*237*	*Lbs*
Sika Plastocrete	*3-6*	*Fl. Ozs/100 cmt*
Sika SVC 1000 Super	*6-14*	*Fl. Ozs/100 cmt*
Sika Set NC-4 Accelerator	-	*Fl. Ozs/100 cmt*
Total	*4,080*	*Lbs*

The w/c ratio for this mix design is 0.4333, indicating a slightly higher proportion of water relative to the cement content than the previous mix design. This adjustment allows for a different balance between water and cement, which can influence the workability and strength characteristics of the

concrete. The air content in the mix is targeted at 1.5%, with a tolerance of ±0.5 to enhance durability. Adequate air entrainment helps improve the concrete's freeze-thaw resistance and overall durability. The desired slump for the mix design remains consistent, with a target of around 7 inches and a tolerance of ±2 inches. A slump is an essential indicator of concrete's workability and ease of placement during construction.

Figure 29 (a) depicts the slump test conducted on specimens with a high cement content, resulting in a measured slump value of 6 inches. In contrast, Figure 29 (b) illustrates the slump test performed on samples featuring a lower cement content, yielding a measured slump of 5.5 inches.

(a) (b)

Figure 29. (a) Slump Test for High Cement Content and (b) Low Cement Content

Furthermore, the expected unit weight for this mix design is 151.1 pounds per cubic foot. Unit weight, or density, is an important property affecting the hardened concrete's structural performance. The prepared concrete material, supplied by Forterra, is transported using compact delivery vehicles, as illustrated in Figure 30.

Figure 30. Concrete Provided at Forterra

3.5.2. Rebars

General properties of steel rebars commonly used in reinforced concrete pipes include:

Grade: Steel rebars for reinforced concrete pipes are typically specified by their grade, indicating the material's minimum yield strength. Common grades include Grade 40, Grade 60, and Grade 75, with corresponding yield strengths of 40,000 psi, 60,000 psi, and 75,000 psi, respectively. The grade selection depends on the design requirements and anticipated loads on the pipe.

***Ductility*:** Steel rebars used in reinforced concrete pipes should possess good ductility to accommodate deformation without sudden failure. Ductility allows the rebars to yield and elongate before reaching their ultimate tensile strength, which enhances the overall toughness and resistance to cracking.

Corrosion Resistance: Reinforced concrete pipes may be exposed to various environmental conditions, including moisture and aggressive chemicals. The steel rebars are often coated with

materials like epoxy or galvanized to protect them from corrosion and increase corrosion resistance.

Bond Strength: The bond strength between the steel rebars and the surrounding concrete is crucial for transferring stresses and ensuring the pipe's structural integrity. Proper surface preparation of rebars and appropriate reinforcement detailing help promote a strong bond between the steel and the concrete.

Weldability: Weldability is essential if the reinforcement requires welding during fabrication. Steel rebars used in reinforced concrete pipes should exhibit good weldability to enable efficient and reliable joining of rebars, ensuring structural continuity.

Dimensional Accuracy: Steel rebars used in reinforced concrete pipes should conform to specified dimensional tolerances to ensure proper fit and alignment within the pipe. Accurate diameters, lengths, and straightness of rebars facilitate their proper placement during construction (ASTM A706, ACI 318).

This project uses two different diameter rebars for the reinforced concrete pipes. The diameter of the rebars for the 24 inches pipe is 0.194 inches (4.95 mm), illustrated in Figure 31 (a), while the diameter for the 96 inches pipe is 0.226 inches (5.75 mm), illustrated in Figure 31 (b).

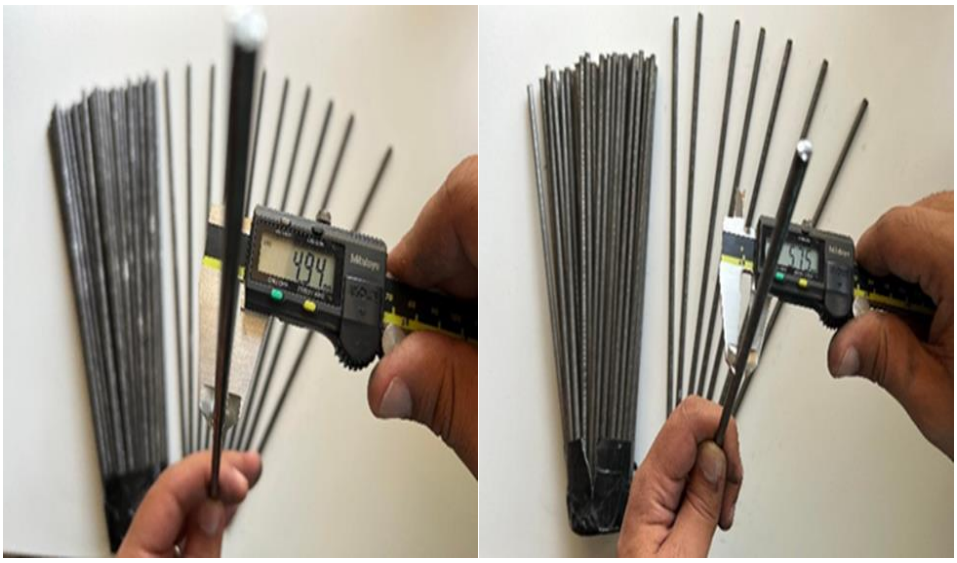

(a) (b)

Figure 31. (a) Rebars Used in 24" Pipe, and (b) Rebars Used in 96" Pipe

The steel coils serve as the source material from which the rebars are cut and fabricated to the desired lengths and diameters. It is worth noting that Forterra follows industry best practices and quality control measures to ensure that the rebars used in their pipes meet the necessary standards for strength, ductility, and corrosion resistance. This helps to ensure the overall quality and structural integrity of the reinforced concrete pipes produced by Forterra. Figure 32 depicts the steel wires obtained from a coil, precisely cut to a length of 12 inches. These steel wires are intended for utilization within a reinforced concrete pipe with a diameter of 24 inches.

Figure 32. Wires for 24 inches of Pipe

3.5.3. Spacers

In this experimental study, rectangular sections of stainless-steel sheets with varying widths, measuring 0.01", 0.03", 0.05", and 0.1", were cut into small pieces measuring 2x1.5 inches. These small stainless-steel pieces were implemented as spacers within the cylindrical specimens, inserted at a depth of 1 inch from the concrete cover. These spacers were used to create uniform crack sizes within the specimens. The spacers were meticulously removed once the concrete was cast, inducing deliberate and controlled artificial cracks of consistent dimensions.

Figure 33 illustrates the specific dimensions and characteristics of the 0.03-inch cut pieces used for further analysis and evaluation.

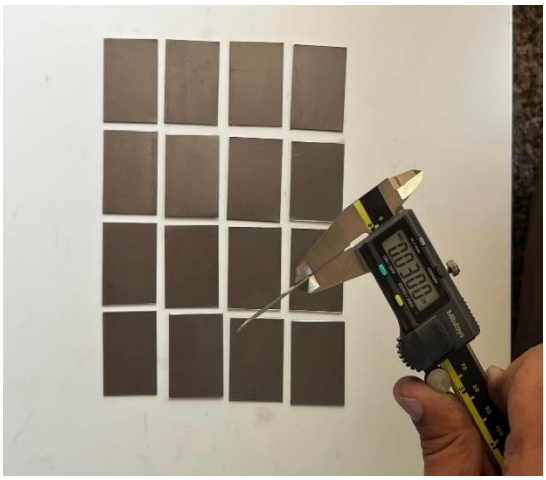

Figure 33. Spacers with the Width of 0.03"

3.5.4. Chloride Sodium

Sodium chloride, commonly known as table salt, is a chemical compound with a NaCl formula. It is an essential mineral and one of the most widely used salts in various applications.

a) Physical Properties:

Sodium chloride appears as a white crystalline solid with a cubic crystal structure. It has a high melting point of 801 degrees Celsius and a boiling point of 1,413 degrees Celsius. It is soluble in water, forming a clear and colorless solution.

b) Chemical Properties:

Sodium chloride is an ionic compound of positively charged sodium ions (Na+) and negatively charged chloride ions (Cl-). It is a stable compound and does not readily undergo chemical reactions under normal conditions. However, it can dissociate into its constituent ions when dissolved in water, making it an electrolyte capable of conducting electricity. Figure 34 indicates the Sodium chloride (NaCl) specifications used in this project.

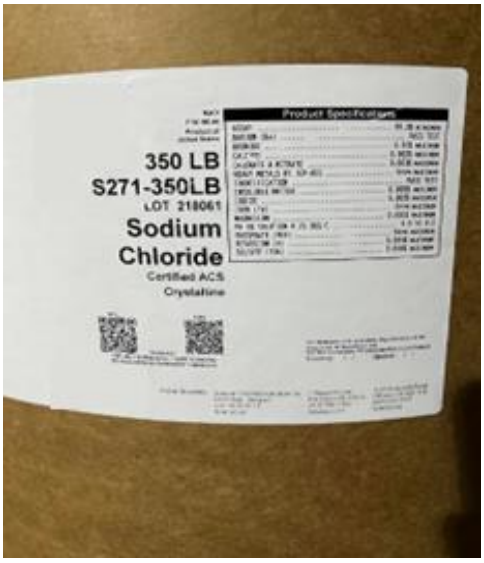

Figure 34. Sodium Chloride

CHAPTER 4. PREPARATION OF TEST

4.1. Experimental Process

In order to initiate the marking process, the cap of the cylinders was initially partitioned into four equal quarters, represented in Figure 35 (a). This partitioning served as a reference point for the subsequent division of the cylinders into the necessary sections for creating cracks intended for spacer placement. A scale was constructed using a (1) foot wooden piece to ensure that all cutting lines were straight and accurate. The wooden piece was divided into four equal parts with three (3) inch spacing, enabling precise and consistent markings illustrated in Figure 35 (b). The marking procedure involved drawing a straight line aligned with the reference cap and marking the specific positions where cracks were to be cut for spacer placement, illustrated in Figure 35 (c). This systematic approach ensured the desired spacing and alignment of the cracks on the cylinders for subsequent steps in the experimental process.

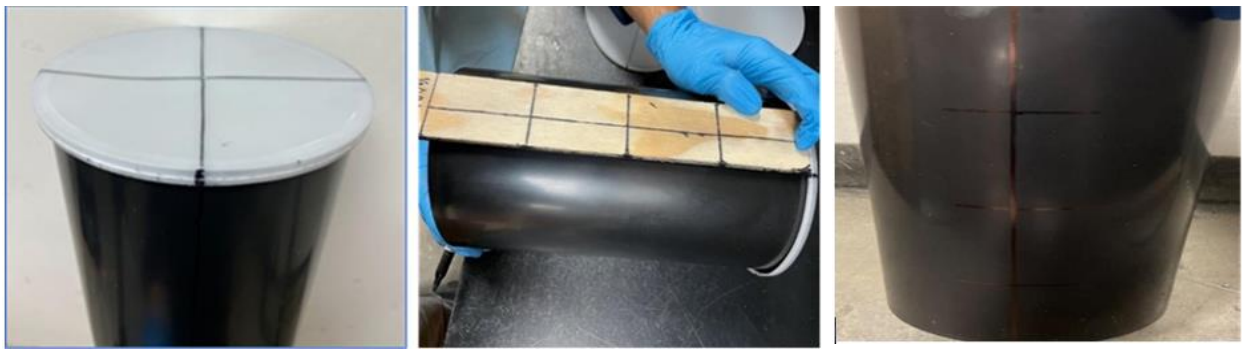

(a) (b) (c)

Figure 35. (a) Partitioned Cap in Four Equal Sections, (b) Wooden Pieces as a marker to Divide in Four Equal Parts, and (c) Marking the Cylinders

The subsequent step involves cutting the cylinders, focusing on the previously marked positions. At each marked point on the cylinder, a horizontal cut of approximately 1.5 inches is made on both sides to create adequate space for placing spacers with the specified thickness. This process entails

cutting at 12 points on a single cylinder, maintaining a vertical spacing of 3 inches between each point. By implementing this procedure, the cylinders are appropriately modified to accommodate the necessary spacers. The cutting process is illustrated in Figure 36.

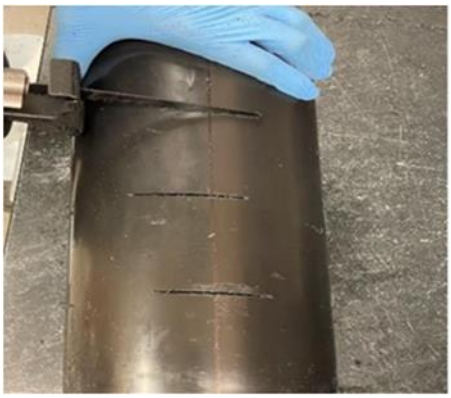

Figure 36. Cutting the Cylinders

In order to facilitate the demolding process of the cylinders after the concrete casting, holes were strategically drilled at the bottom of each cylinder, as indicated in Figure 37. The purpose of these holes was to enable the application of air pressure, which would aid in detaining the cylinders from the concrete. One thousand two hundred ninety-six holes were carefully drilled across the cylinder surfaces to ensure effective demolding.

Figure 37. Making a Hole at the Bottom of the Cylinders

Stainless steel sheets were employed as spacers. These spacers play a crucial role in creating predetermined crack dimensions. Following the proposed experimental design, four distinct spacer sizes were utilized, with crack thicknesses measuring 0.01", 0.03", 0.05", and 0.1", as indicated in Figure 38 (a), 38 (b), 38 (c), and 38 (d) respectively. Each spacer shared a uniform dimension of 1.5" x 2".

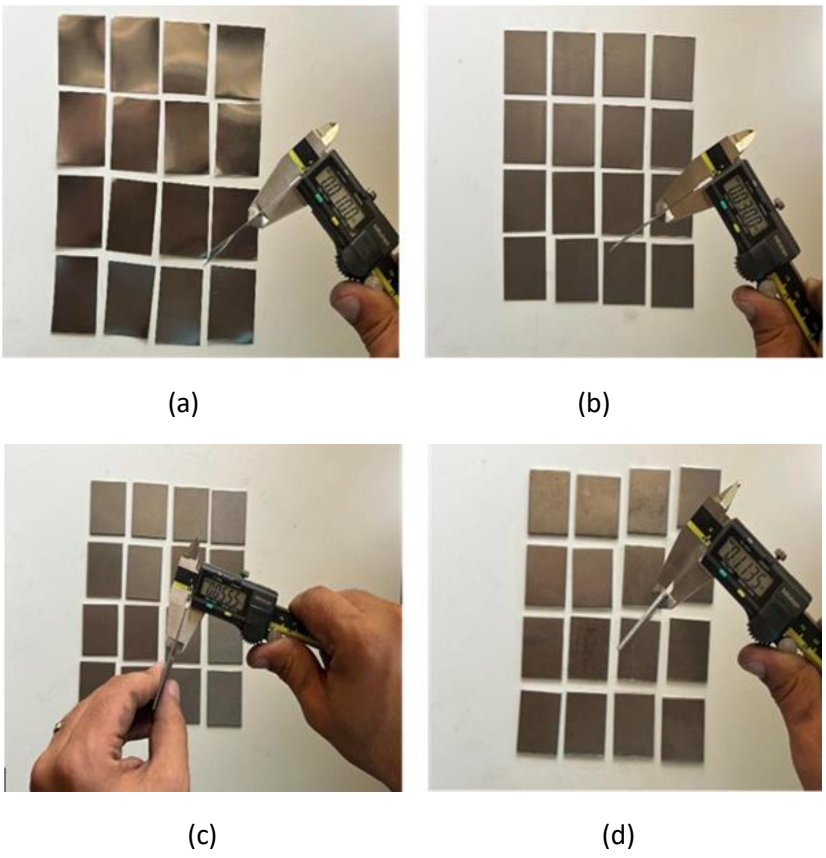

Figure 38. Spacers with (a) 0.01", (b) 0.03", (c) 0.05", and (d) 0.1" Widths

The next step involved carefully placing the spacers into the previously cut cylinders. As mentioned, these spacers are deliberate crack inducers within concrete specimens. Each cylinder was outfitted with 12 spacers, distributed evenly throughout its length. A total of 324 cylinders

were designated to accommodate 0.01" spacers, resulting in the insertion of 3,888 spacers overall. Similarly, an equal number of cylinders were assigned for 0.03", 0.05", and 0.1" spacers, yielding a total of 15,552 spacers distributed among 1,296 cylinders across the four distinct sizes as indicated in Figure 39.

Figure 39. Placing the Spacers

The rebar weight measurements for both the 24-inch pipe and 96-inch pipe were conducted individually, ensuring accurate determination of their respective weights. Each rebar was meticulously measured and labeled for identification purposes.

The average weight of the rebars used in the 24-inch pipe was approximately 46 grams. Similarly, the rebars utilized in the 96-inch pipes exhibited an average weight of approximately 61 grams, as indicated in Figure 40 (a). These precise measurements and corresponding labeling of the rebars allowed for accurate documentation and subsequent analysis of their weights, as indicated in Figure 40 (b).

(a) (b)

Figure 40. (a) Measuring the Rebar's Weight, and (b) Labeling

The proposed plan determined that the cylinders should have a concrete cover of 1 inch at the bottom. So, concrete cubes were prepared specifically for this purpose. These cubes were made using ready concrete with a high strength of 5,000 psi. The concrete cubes were carefully crafted to ensure their structural integrity and to meet the required strength specifications. Once the cubes were prepared, the wires were placed on top, ensuring they were positioned securely and aligned with the designated locations within the cylinders, as indicated in Figure 41.

Figure 41. Concrete Cubes for Cover

The placement of the wires in the cylinders represents the final step before the casting process. In each cylinder, four wires, each measuring 12 inches long, are carefully positioned. The wires are

placed within concrete cubes, ensuring they encounter the previously inserted spacers. Each wire should have a 1-inch cover on the sides, which is achieved by the presence of spacers. This arrangement ensures the appropriate positioning and alignment of the wires within the concrete matrix.

Additionally, all the wires should be securely tied at the top of the cylinders, ensuring they remain fixed during the casting process and subsequent testing. This step guarantees that the wires will not shift or move within the concrete, as indicated in Figure 42, allowing for accurate and consistent measurement of their behavior during the experimental phase.

Figure 42. Placing the Wires in Cylinders

Once the cylinders have been prepared with spacers and rods, it is time to proceed with the casting process. This experiment used a high cement ratio for all cylinders. All the cylinders were lubricated with WD-40 for the demolding process, allowing easy removal of the spacers and cylinders, as indicated in Figure 43 (a).

The next step involves pouring the concrete into the cylinders. This step requires careful attention to ensure all the rods encounter the spacers. The casting process is carried out in three layers. After filling the first layer, the cylinder is placed on a vibrating machine to minimize the presence of air voids. The second and third layers are filled and compacted simultaneously using a rod.

Continuous concrete vibration is applied throughout the casting process, as indicated in Figure 43 (b). The average slump test conducted for the concrete mixture was 6".

After the casting, the cylinders are covered with plastic for a specified period, typically a couple of hours. This cover helps maintain the necessary moisture and temperature conditions for properly curing the concrete. After the designated time, the spacers were carefully removed from the cylinders, typically after 5-6 hours.

(a) (b)

Figure 43. (a) Using WD-40, and (b) Casting Cylinders

The next step in the experimental procedure involves demolding the concrete cylinders and transferring them to the designated pools. A total of 15 pools have been prepared, arranged in 5 rows, with each row assigned specific voltage conditions. The rows include a control group, two, four, and eight voltages. The final row consists of concrete cylinders containing thicker wires, which will be subjected to the highest voltage level (8 Volt) to investigate the corrosion rates compared to cylinders with the same voltage conditions but different wire diameters corresponding to the 24" pipes.

Three individual pools have been established within each row, each with a specific chloride sodium concentration of 2,000 ppm, 30,000 ppm, or 10,000 ppm. The pools have dimensions of 8 feet 5 inches in length, 5 feet 6 inches in width, and 2 feet in depth, as indicated in Figure 44.

Figure 44. Setup Pools.

The volume of the pools was determined through a systematic calculation process; all the dimensions from feet and inches were converted to inches.

Length: 8 feet + 5 inches = 8 × 12 inches + 5 inches = 96 inches + 5 inches = 101 inches

Width: 5 feet + 6 inches = 5 × 12 inches + 6 inches = 60 inches + 6 inches = 66 inches

Depth: 1 foot = 1 × 12 inches = 12 inches

Calculate the volume in cubic inches:

Volume = Length × Width × Depth

Volume = 101 inches × 66 inches × 12 inches

Volume = 79,872 cubic inches

The amount should divide by 61.024 (since one cubic inch is approximately equal to 0.0163871 liters):

Volume in liters = 79,872 cubic inches / 61.024

Volume in liters ≈ 1,308 liters

The necessary amount of salt that needs to create a specific solution in 1307 liters of water, the following calculation can be used:

PPM = (Mass of Solute / Mass of Solution) × 1,000,000

For example, to create a concentration of 100,000 ppm in 1,307 liters of water, assume the mass of the solution is the sum of the mass of water and salt.

Rearranging the formula:

Mass of Solute = (PPM × Mass of Solution) / 1,000,000

Mass of Solute = (100,000 ppm × 1,307 liters) / 1,000,000

Mass of Solute = 130.7 kilograms

Table 11 shows the chloride sodium required to reach different concentrations (2,000 ppm, 30,000 ppm, and 10,000 ppm).

Table 11. Salt Mass Required to Achieve Different Concentrations in the Pool

Concentration (ppm)	The volume of Water (liters)	Chloride Sodium required (kg)
2,000	*1,307*	*2.7*
30,000	*1,307*	*40*
100,000	*1,307*	*131*

The final test procedure is connecting the power supply to the cylinders. As mentioned, each pool is assigned specific voltages applied to the cylinders. Figure 45 illustrates the configuration wherein 8 Volt was applied to the reinforcement bars. Following the accelerated corrosion test and utilizing the electrochemical corrosion test, all the rebars within the cylinders are connected to the anode. In contrast, the cathode section is connected to copper bars. This configuration enables the initiation and monitoring of the corrosion process during the experiment.

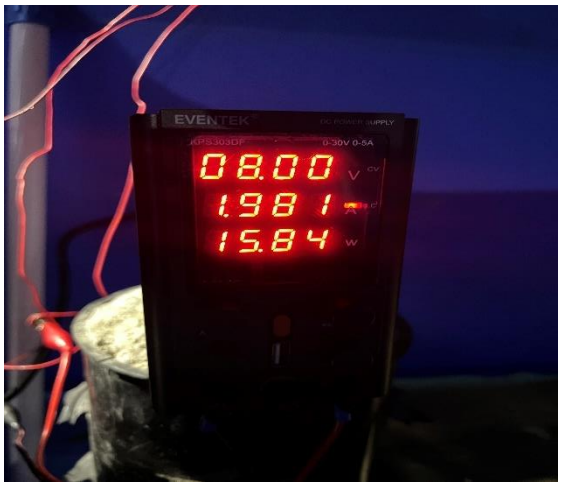

Figure 45. Voltage Application Setup

CHAPTER 5. RESULTS

5.1. Overview

This chapter presents the results of the experimental investigation to assess the corrosion behavior of immersed cylinders in different solutions. The study focused on evaluating the probability of corrosion and measuring the corrosion rates by employing the half-cell potential test method and examining the remaining weight percentage, respectively.

The immersed cylinders, varying in crack sizes (0.01", 0.03", 0.05", and 0.1"), were subjected to monthly testing. Two cylinders from each crack size were selected for testing. The experiment encompassed different solutions with varying concentrations (2,000, 30,000, and 100,000 ppm) and applied voltages (Control or zero, 2, 4, and 8).

To initiate the testing process, a Profometer Proceq corrosion meter was utilized to determine the probability of corrosion. Subsequently, all the cylinders were broken to remove their residual rebars. A steel brush was then used to eliminate rust, cleaning the cylinders. The remaining weight of the rebars was measured to evaluate the extent of corrosion.

1. Half-Cell Potential Test Method by using Profometer corrosion rate:

The Profometer Proceq corrosion meter provided valuable measurements for evaluating the corrosion probability. The measurements obtained from the 12 points on each cylinder were averaged for further analysis. The obtained data were compared with the remaining weight values to ensure compliance with ASTM C876 requirements. The obtained results were reported in millivolts (mV).

2. Remaining Weight:

The remaining weight percentages of the rebars were calculated and analyzed to determine the corrosion rates. The measured values were compared to the rebars' initial weight to assess the corrosion extent. Furthermore, the corrosion rates were determined for each parameter combination, considering the crack width, concentration solutions, and applied voltages.

Statistical methods were applied to analyze the obtained data. Variance (ANOVA) was analyzed to determine significant differences among the concentration solutions, voltages, and crack width for the remaining weight percentages results. Post hoc tests, specifically Tukey's Honestly Significant Difference (HSD) test, were conducted to identify specific pairwise differences between the concentration solutions and voltages.

5.2. Results from Profometer

As previously mentioned, the Profometer provides corrosion probability results in millivolts (mV) for the tested sample sections. According to the ASTM C876 standard, a more negative mV value on the Profometer indicates higher corrosion in the tested samples. In this study, the samples were initially cast without immersion in any solutions and exhibited an average Profometer reading of -120 mV, indicating no corrosion. However, these values changed over time as crack widths and voltages varied.

The maximum Profometer value recorded was -592 mV at 8 Volt, 30,000 ppm chloride concentration, and crack widths of 0.1". At this combination, approximately 99% of the reinforcement bars exhibited corrosion. The complete corrosion rate, defined as -600 mV on the Profometer, was observed at two months for 8 Volt, 100,000 ppm chloride concentration, and crack widths of 0.1" and 0.05".

In this study, the average Profometer reading of -195 mV corresponded to a corrosion level of 10%. Furthermore, the target corrosion level of 50% was associated with an average Profometer reading of -285 mV. It is worth noting that all the Profometer values obtained in the study fell within the range specified by ASTM C876. These findings indicate a correlation between the Profometer readings and the observed corrosion levels, supporting the validity of the ASTM C876 standard.

Figure 46 illustrates the correlation between Profometer readings and remaining weights throughout the six-month test duration, encompassing all the test results.

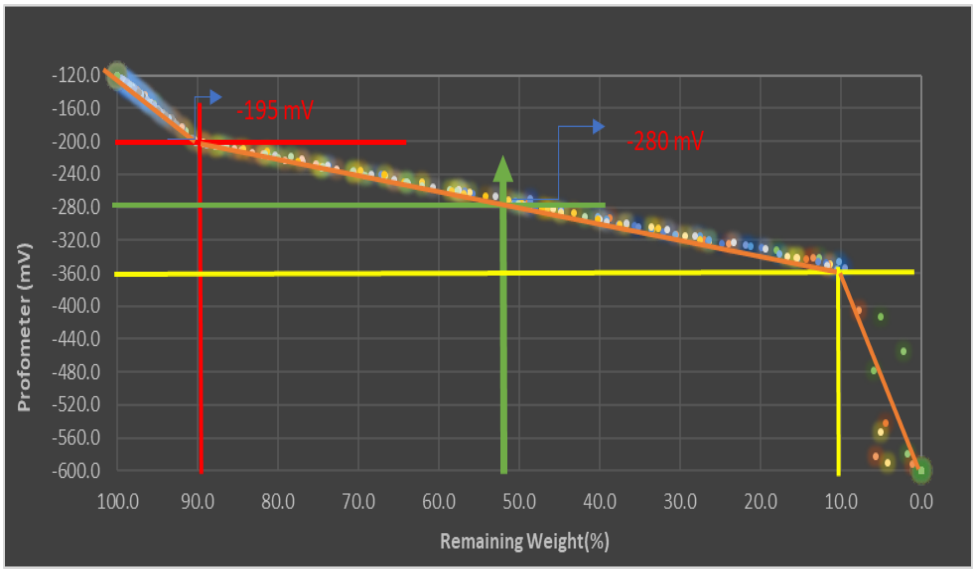

Figure 46. Profometer Reading (mV) & Remaining Weight (%)

5.3. Results from Remaining Weight

This study investigated rebar corrosion rate based on the samples' remaining weight. The research design used samples with varying crack widths, namely 0.01, 0.03, 0.05, and 0.1 inches. These samples were fully immersed in solutions containing chloride concentrations of 2,000, 30,000, and 100,000 parts per million (ppm), with three different voltages applied. Additionally, control

samples were tested without any voltage applied to the rebars. The corrosion rate was monitored monthly for six months, examining the relationship between the corrosion rate and the percentage of remaining weight.

This section aims to elucidate the impact of each variable on the corrosion rate. Specifically, the influence of crack width, chloride concentration, voltage, and the absence of applied voltage will be discussed about the observed corrosion rates. By analyzing the corrosion rates in conjunction with the corresponding remaining weight percentages, insights into the effect of each variable on the corrosion process can be obtained.

5.3.1. Effect of Voltages on Corrosion Rate

The voltage, or more precisely, the difference in electrical potential between different points in the reinforced concrete, can influence the corrosion rate of rebars. This phenomenon is commonly referred to as corrosion or open-circuit potential. The corrosion potential is the voltage between the rebars and the surrounding concrete without external electrical forces. In reinforced concrete, the corrosion of rebars is an electrochemical process that involves anodic and cathodic reactions. The anodic reaction occurs at the metal surface of the rebar, where iron atoms are oxidized, producing ferrous ions (Fe^{++}) and releasing electrons. The cathodic reaction occurs on the concrete surface, where oxygen and water combine with the released electrons to form hydroxyl ions (OH^-) or react with other substances in the concrete (Poursaee and Hansson 2010).

Table 12 presents the results for cylinders immersed in a 2,000-ppm solution with different applied voltages and a crack size of 0.01".

Table 12. Effect of Voltages at 2,000 ppm and 0.01"Crack Width.

0.01"			0	30	60	90	120	150	180
2,000 ppm	*0 V*	*Remaining Weight (%)*	*100.0*	*99.7*	*99.4*	*99.2*	*98.9*	*98.5*	*98.2*
	2 V	*Remaining Weight (%)*	*100.0*	*97.5*	*95.8*	*93.5*	*91.5*	*89.4*	*87.7*
	4 V	*Remaining Weight (%)*	*100.0*	*87.0*	*76.9*	*69.4*	*63.8*	*57.4*	*50.6*
	8 V	*Remaining Weight (%)*	*100.0*	*66.6*	*57.5*	*47.1*	*36.6*	*26.3*	*11.3*

After 180 days of testing, the remaining weight of rebars for the cylinders without electricity applied was 98.2% of the initial weight. This indicates that only 1.8% of the rebars' weight was corroded during testing. On the other hand, the cylinders with 2, 4, and 8 Volts applied showed a significant reduction in remaining weight.

For the cylinders with 2 Volt applied, the remaining weight decreased to 87.7% after 180 days. This represents corrosion of approximately 12.3% of the rebars' weight. Similarly, the cylinders with 4 Volt applied experienced a more substantial reduction in remaining weight, reaching 50.6% after 180 days, indicating corrosion of approximately 49.4% of the rebars' weight. The most significant corrosion was observed in the cylinders with 8 Volt applied, where the remaining weight dropped to 11.3% after 180 days. This indicates corrosion of approximately 88.7% of the rebars' weight. Notably, the cylinders with 8 Volt applied experienced rapid weight loss, losing 50% of their weight within 60 days of testing as is evident, higher voltages accelerating the corrosion process, leading to a more significant weight loss. Figure 47 depicts the remaining values observed on different voltages applied on the cylinders subjected to the immersion of 2,000 (ppm) and cylinders with a crack width of 0.01 inches.

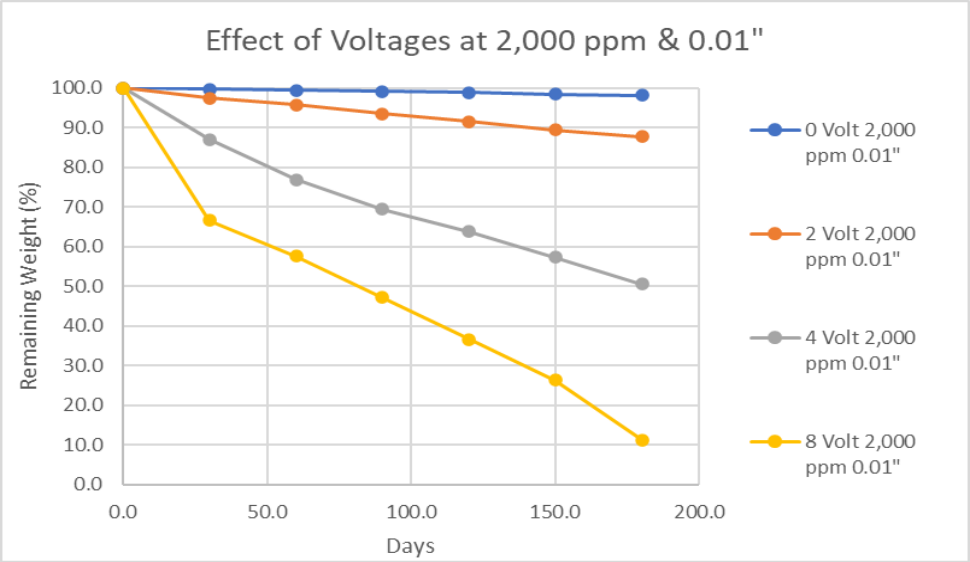

Figure 47. Effect of Voltages at 2,000 ppm & 0.01" Crack Width

Table 13 presents the outcomes of the analysis of variance (ANOVA). The "Source" column identifies the investigated factors, while "DF" denotes the degrees of freedom. The "SS" column indicates the sum of squares, and "MS" represents the mean square. The "F Value" column presents the computed F statistic, and the "p-value" column signifies the significance level associated with the analysis.

Table 13. ANOVA Results.

Source	DF	SS	MS	F Value	P-Value
Voltage	*3*	*10,813*	*3604*	*12.4*	*<0.001*
Residuals	*24*	*6,974*	*291*	-	-

The ANOVA test indicates a significant effect of voltage on the remaining weight of the cylinders ($p < 0.05$).

Table 14 represents the results of the HSD test. Tukey's HSD test shows the differences in means between the voltage levels. In Tukey's HSD test results table, the "Comparison" column indicates the comparison between different voltage levels. "Diff" represents the difference in meaning,

"Lower" and "Upper" represent the lower and upper bounds of the confidence interval, and "p adj" represents the adjusted p-value.

Table 14. HSD Results.

Comparison	Diff	Lower	Upper	p adj
2 V – 0 V	*-5.5000*	*-30.637*	*19.637*	*0.9300*
4 V – 0 V	*-26.971*	*52.108*	*-1.835*	*0.0323*
8 V – 0 V	*-49.786*	*-74.922*	*-24.649*	*<0.001*
4 V – 2 V	*-21.47143*	*-46.60795*	*3.665096*	*0.1132937*
8 V – 2 V	*-44.28571*	*-69.4222*	*-19.149190*	*0.0003252*
8 V – 4 V	*-22.81429*	*-47.95081*	*2.322239*	*0.08478*

The p-values for the comparisons are as follows:

Two Volt vs. 0 Volt: There is no significant difference in the remaining weight between these two voltage levels (p = 0.9299).

Four Volt vs. 0 Volt: The remaining weight is significantly lower at 4 Volt compared to 0 Volt (p = 0.0323).

Eight Volt vs. 0 Volt: The remaining weight is significantly lower at 8 Volt compared to 0 Volt (p = 0.0001).

Four Volt vs. 2 Volt: There is no significant difference in the remaining weight between these two voltage levels (p = 0.1133).

Eight Volt vs. 2 Volt: The remaining weight is significantly lower at 8 Volt compared to 2 Volt (p = 0.0003).

Eight Volt vs. 4 Volt: There is no significant difference in the remaining weight between these two voltage levels (p = 0.0848).

These results suggest that as the voltage level increases, the remaining weight of the samples decreases significantly. The post-hoc test indicates significant differences between 0 Volt, 4 Volt, and 8 Volt, indicating that higher voltages have a more detrimental effect on the remaining weight. However, there is no significant difference between 2 Volt and 0 Volt.

Table 15 presents the data depicting the percentage of remaining weight for samples with a crack width of 0.01 inches immersed in a solution containing a chloride concentration of 30,000 ppm.

Table 15. Effect of Voltages at 30,000 ppm and 0.01" Crack Width.

0.01"			**0**	**30**	**60**	**90**	**120**	**150**	**180**
30,000 ppm	*0 V*	*Remaining Weight (%)*	*100.0*	*99.5*	*99.1*	*98.5*	*97.9*	*97.4*	*97.0*
	2 V	*Remaining Weight (%)*	*100.0*	*95.4*	*90.7*	*87.4*	*81.1*	*75.1*	*70.5*
	4 V	*Remaining Weight (%)*	*100.0*	*73.7*	*64.1*	*55.7*	*44.8*	*32.1*	*19.9*
	8 V	*Remaining Weight (%)*	*100.0*	*48.9*	*38.7*	*27.0*	*11.6*	*0.0*	*0.0*

Based on the data obtained, it is evident that the corrosion rate of rebars is influenced by the voltage levels applied. After 180 days without an electricity connection, only 3% of the total rebar weight exhibited signs of corrosion. However, when voltages 2, 4, and 8 were applied, the corresponding percentages of corroded rebar weight were 29.5%, 71.1%, and 100%, respectively. Furthermore, in the case of 0 and 2 Volts, more than 50% of the total weight of the rebars remained unaffected. However, for a voltage of 4 Volt, approximately 50% of the rebar weight remained intact for 90 days of immersion. However, within an additional two months, more than 50% of the total rebar weight had corroded.

The absolute differences between the voltage levels were also calculated. The differences in remaining weights between voltage_2 and voltage_0, voltage_4 and voltage_0, voltage_8 and voltage_0, voltage_4 and voltage_2, voltage_8 and voltage_2, and voltage_8 and voltage_4 were found to be 12.7, 42.7, 66.1, 29.9, 53.4, and 23.4 respectively. These values represent the absolute

disparities in remaining weights between each pair of voltage levels, which can be used to evaluate the effect of different voltage levels on the corrosion rate of the rebars.

The results of the analysis of variance (ANOVA) revealed a significant effect of voltage on the remaining weights ($F(3, 24) = 11.99$, $p < 0.001$), indicating that the different voltage levels have a substantial impact on the corrosion rate of the rebars. A post hoc test using Tukey's honest significant difference (HSD) was conducted to examine the pairwise differences between voltage groups further.

The post hoc test results indicate statistically significant differences in the means of certain voltage comparisons. Specifically, the comparisons between voltage_4 and voltage_0 ($p = 0.009$) and voltage_8 and voltage_0 ($p = 0.00008$) show significant mean differences. The difference between voltage_8 and voltage_2 ($p = 0.001$) is also statistically significant. On the other hand, the differences between voltage_2 and voltage_0 ($p = 0.724$), voltage_4 and voltage_2 ($p = 0.092$), and voltage_8 and voltage_4 ($p = 0.244$) are not statistically significant.

From these findings, it can be concluded that the voltage level significantly affects the remaining weights of the rebars. As the Voltage level increases, there is a notable decrease in the remaining weights. The most substantial reduction is observed when comparing voltage_8 with voltage_0, indicating that applying a higher voltage (8 Volts) significantly reduces the remaining weights.

Figure 48 shows the remaining values observed on different voltages applied on the cylinders subjected to the 30,000 (ppm) and cylinders with a crack width of 0.01 inches.

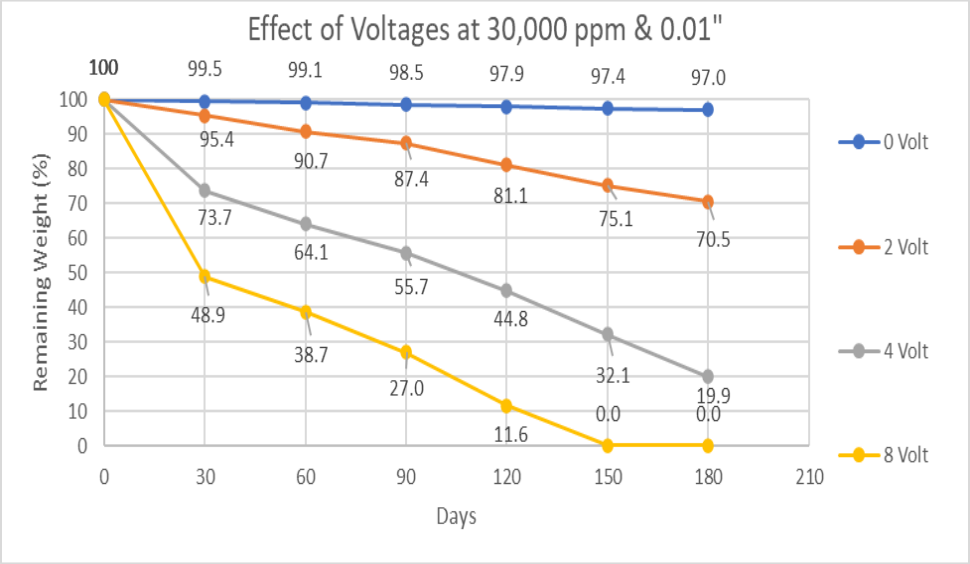

Figure 48. Effect of Voltages at 30,000 ppm and 0.01" Crack Width.

The results obtained from samples immersed in 100,000 ppm solutions and crack width of 0.01" for different voltages are indicated in Table 16.

Table 16. Effect of Voltages at 100,000 ppm and 0.01" Crack Width.

0.01"			**0**	**30**	**60**	**90**	**120**	**150**	**180**
100,000 ppm	*0 V*	*Remaining Weight (%)*	*100.0*	*98.7*	*97.5*	*96.3*	*94.3*	*93.0*	*91.8*
	2 V	*Remaining Weight (%)*	*100.0*	*84.3*	*74.7*	*62.1*	*56.8*	*51.4*	*46.5*
	4 V	*Remaining Weight (%)*	*100.0*	*40.2*	*30.6*	*17.6*	*10.5*	*0.0*	*0.0*
	8 V	*Remaining Weight (%)*	*100.0*	*12.7*	*1.7*	*0.0*	*0.0*	*0.0*	*0.0*

After 180 days, it was found that 7.4% of the total weight of the rebars was corroded in the 0-Volt samples, while 50% of the weight remained intact in the 2-Volt samples. However, the corrosion was complete for the 4-Volt and 8-Volt samples, with no remaining weight observed after six months. In the case of samples exposed to 100,000 ppm solutions with 4-Volt, 50% weight loss occurred within the second month, while for the 8-Volt, only 18% of the weight remained after 30 days of immersion. Figure 49 visually depicts the weight loss for different voltage levels.

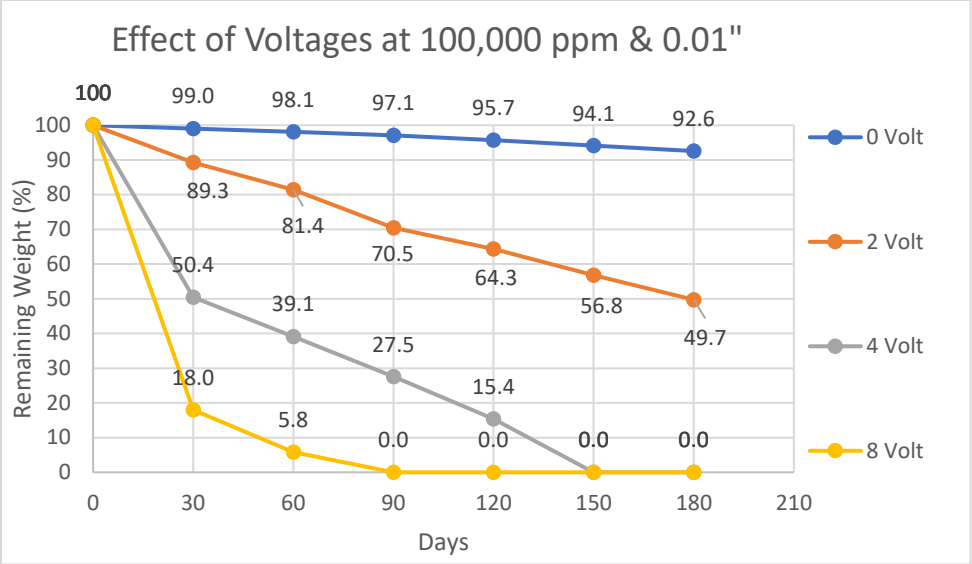

Figure 49. Effect of Voltages at 100,000 ppm and 0.01" Crack Width.

The results of the analysis of variance (ANOVA) indicate that the voltage level has a significant effect on the corrosion rate of the rebars ($p < 0.001$). Tukey's honest significant difference (HSD) test was conducted further to investigate the pairwise differences between the voltage groups. The HSD test results show statistically significant differences in the means of specific voltage comparisons. The mean difference between the 4-Volt and 0-Volt groups ($p = 0.001$) and between the 8-Volt and 0-Volt groups ($p = 0.0001$) are statistically significant. The mean difference between the 8-Volt and 2-Volt groups ($p = 0.004$) is also statistically significant. However, there is no statistically significant difference between the 2-Volt and 0-Volt groups ($p = 0.382$), between the 4-Volt and 8-Volt groups ($p = 0.708$), and between the 2-Volt and 4-Volt groups ($p = 0.049$).

Based on these results, it can be concluded that increasing the voltage level significantly affects the corrosion rate of the rebars. Significant differences exist between the 0-Volt and 4-Volt, and 8-Volt groups, indicating that higher voltage levels lead to more excellent corrosion. A significant difference is observed between the 2-Volt and 8-Volt groups, suggesting that an increase from 2

to 8 Volts intensifies the corrosion process. However, no significant differences were found between the 2-Volt and 0-Volt groups, the 4-Volt and 8-Volt groups, and the 2-Volt and 4-Volt groups.

5.3.2. Effect of Crack Width on Corrosion Rates

The experimental findings indicate that cracks in concrete specimens significantly impact the corrosion of embedded reinforcement. Although crack width may not immediately affect the extent of reinforcement corrosion in the early stages of reinforced concrete structures, it becomes significant in the long term, particularly when considering the width, frequency, and location of cracks. Cracking in the tensile zone of loaded reinforced concrete structures exhibits a more significant influence on reinforcement corrosion than cracking in the compressive zone of loaded structures. This is attributed to the detrimental effects of increased strain intensity on the paste-aggregate interface, facilitating the penetration of chloride ions into the concrete. (Neave 1995).

The corrosion rate of rebars at zero voltages and 2,000 ppm was investigated, and the results are represented in Table 17. The corrosion process was evaluated by monitoring the rebars' remaining weight over 180 days. Different crack widths (0.01, 0.03, 0.05, and 0.1 inches) were considered, and measurements were taken at regular intervals of 30 days.

Table 17. Effect of Crack Width on Corrosion Rate at 2,000 ppm and 0 Volt

Days	**0**	**30**	**60**	**90**	**120**	**150**	**180**
Remaining Weight of 0.1"	*100*	*98.8*	*97.9*	*97.0*	*96.3*	*95.4*	*94.7*
Remaining Weight of 0.05"	*100*	*99.2*	*98.6*	*97.9*	*97.3*	*96.5*	*95.8*
Remaining Weight of 0.03"	*100*	*99.5*	*99.1*	*98.6*	*98.3*	*97.8*	*97.4*
Remaining Weight of 0.01"	*100*	*99.7*	*99.4*	*99.2*	*98.9*	*98.5*	*98.2*

At the initial time (0 days), all crack widths showed the same remaining weight of 100%. However, as the days progressed, the corrosion became more evident. For the crack width of 0.1", the remaining weight decreased to 94.66% at 180 days. Decreasing the crack width to 0.05 inches results in a slightly higher remaining weight of 95.81%. Further reducing the crack width to 0.03 inches leads to a higher remaining weight of 97.41%. The smallest crack width of 0.01 inches corresponds to the highest remaining weight of 98.18%.

The correlation coefficient for each crack width can be calculated to find the relationship between each crack width. Calculating correlation coefficients requires mathematical computations that are typically implemented in statistical software. The equation for the correlation coefficient is:

$$\boldsymbol{Correlation\ Coefficient} = (n \times \sum(XY) - (\sum X)(\sum Y)) \Big/ \sqrt{((n \times \sum X^2 - (\sum X)^2) \times (n \times \sum Y^2 - (\sum Y)^2)}$$

X represents the crack width values

Y represents the remaining weight values

n is the number of observations

$\sum$ denotes the sum of values, and $\sum$(XY)

$\sum X^2$ and $\sum Y^2$ are the sum of cross-products squared X and Y values, respectively. Table 18 presents the Correlation Coefficient about varying crack dimensions observed at 2,000 ppm and 0 Volt conditions.

Table 18. Correlation Coefficient for Different Crack Sizes at 2,000 ppm and 0 Volt

Crack Width	0.1"	0.05"	0.03"	0.01"
Correlation Coefficient	*-0.984*	*-0.982*	*-0.967*	*-0.948*

The correlation coefficients range from -1 to 1, where -1 represents a strong negative correlation, 0 represents no correlation, and 1 represents a strong positive correlation.

The crack width of 0.1 inches shows a significant decrease in remaining weight over time, indicating a higher corrosion rate than the other crack widths.

The crack width of 0.05 inches also exhibits a noticeable decrease in remaining weight, suggesting a relatively high corrosion rate.

The crack width of 0.03 inches demonstrates a decrease in remaining weight, indicating a moderate corrosion rate.

The crack width of 0.01 inches shows a smaller decrease in remaining weight, suggesting a lower corrosion rate than the other crack widths.

Figure 50 illustrates the graphical representation of the samples immersed in a solution with a concentration of 2,000 ppm and no applied voltage. The graph demonstrates the relationship between crack width and corrosion rate.

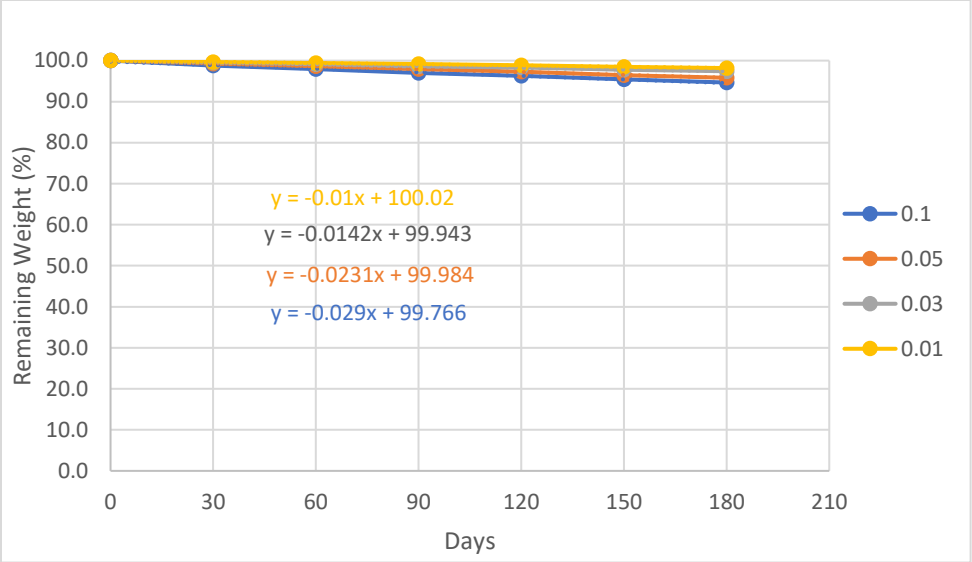

Figure 50. Effect of Crack Width at 2,000 ppm and 0 Volt

Table 19 presents the results regarding the remaining weight of various samples with different crack widths subjected to two applied voltages at a concentration of 2,000 ppm.

Table 19. Effect of Crack Width on Corrosion Rate at 2,000 ppm and 2 Volt

Days	**0**	**30**	**60**	**90**	**120**	**150**	**180**
Remaining Weight of 0.1"	*100*	*91.9*	*83.1*	*79.2*	*75.3*	*70.5*	*65.6*
Remaining Weight of 0.05"	*100*	*94.7*	*89.4*	*85.5*	*81.8*	*77.0*	*72.6*
Remaining Weight of 0.03"	*100*	*96.6*	*93.1*	*90.4*	*87.6*	*84.6*	*81.9*
Remaining Weight of 0.01"	*100*	*97.5*	*95.8*	*93.5*	*91.5*	*89.4*	*87.7*

The findings indicate that after a 180-day testing period, the samples with crack widths of 0.1", 0.05", 0.03", and 0.01" retained 65.58%, 72.63%, 81.88%, and 87.72% of their initial weight, respectively. A correlation analysis was also performed to assess the relationship between crack size and remaining weight.

The correlation coefficients for the crack sizes are as follows:

The correlation coefficient for 0.1" crack size: -0.994

The correlation coefficient for 0.05" crack size: -0.997

The correlation coefficient for 0.03" crack size: -0.998

The correlation coefficient for 0.01" crack size: -0.999

These coefficients demonstrate a strong negative correlation between crack size and remaining weight, indicating that the remaining weight decreases as the crack size increases.

To further investigate the significance of the crack sizes concerning remaining weight, an Analysis of Variance (ANOVA) test was conducted.

The ANOVA results are as follows:

F-value: 158.76

p-value: < 0.001

The obtained p-value, which is lower than the significance level of 0.05, signifies significant differences in remaining weight among the crack sizes.

Subsequently, an HSD (Tukey's Honestly Significant Difference) test was performed to determine which crack sizes exhibit statistically significant differences in remaining weight.

The HSD test results are as follows:

Comparison between 0.1" and 0.05" crack sizes: p-value = 0.005 (Reject H0)

Comparison between 0.1" and 0.03" crack sizes: p-value < 0.001 (Reject H0)

Comparison between 0.1" and 0.01" crack sizes: p-value < 0.001 (Reject H0)

Comparison between 0.05" and 0.03" crack sizes: p-value < 0.001 (Reject H0)

Comparison between 0.05" and 0.01" crack sizes: p-value < 0.001 (Reject H0)

Comparison between 0.03" and 0.01" crack sizes: p-value = 0.074 (Fail to reject H0)

Based on the HSD test results, all crack sizes exhibit significant differences in remaining weight, except for the comparison between 0.03" and 0.01" crack sizes, where the difference is not statistically significant. Therefore, the crack size with the most significant effect on remaining weight is 0.1".

The HSD test outcomes suggest that the remaining weight for the 0.1" crack size significantly differs from the remaining weights of all other crack sizes (0.05", 0.03", and 0.01"). Conversely, the remaining weights of the other crack sizes (0.05", 0.03", and 0.01") may exhibit significant differences from each other but not from the remaining weight of the 0.1" crack size.

Hence, the 0.1" crack size demonstrates the most significant impact on remaining weight compared to the other crack sizes.

To determine the decrease in remaining weight and the percentage weight loss as the crack size increases from 0.01" to 0.1", the values at a specific time point, such as 180 days, can be compared.

At 180 days:

The remaining weight for the 0.01" crack size is 87.72.

The remaining weight for the 0.1" crack size is 65.58.

Decrease in remaining weight = Remaining weight for 0.01" - Remaining weight for 0.1" =

87.72 - 65.58 = 22.14

The decrease in remaining weight when the crack size increases from 0.01" to 0.1" is 22.14 units.

Percentage weight loss = (Decrease in remaining weight / Initial remaining weight) × 100

For the 0.01" crack size:

Percentage weight loss = (22.14 / 100.00) × 100 = 22.14%

This implies that as the crack size increases from 0.01" to 0.1", the remaining weight experiences a substantial reduction of 22.14%, indicating a significant weight loss due to corrosion. Figure 51 illustrates the results of various crack widths at a concentration of 2,000 ppm and under the application of 2 Volt.

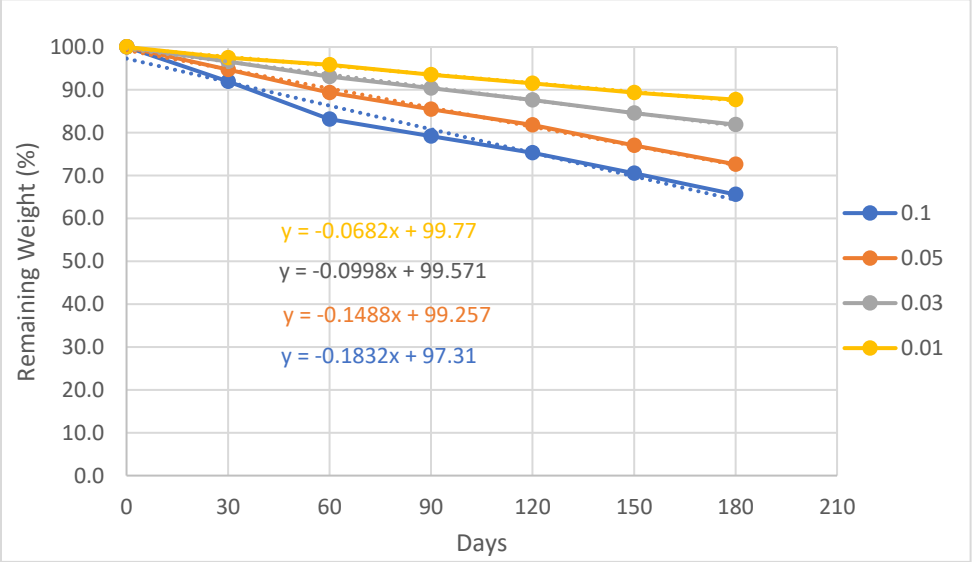

Figure 51. Effect of Crack width at 2,000 ppm and 2 Volt

5.3.3. Effect of Sodium Chloride on Corrosion Rates

Accelerated Corrosion: Sodium chloride is hygroscopic and absorbs environmental moisture, creating an electrolyte solution on the metal surface. This solution facilitates the flow of ions, leading to increased electrochemical reactions and accelerated corrosion rates (Song and Atrens, 1999). Chloride ions from sodium chloride can penetrate the protective oxide layer on the metal

surface, exposing the underlying metal to corrosion. Chlorides can disrupt passivation, making the metal more susceptible to corrosion attacks (Alavi et al., 2007). Sodium chloride is mainly known for promoting pitting corrosion, which involves a localized attack on the metal surface. Chloride ions initiate pit formation; once initiated, the pits can propagate, leading to extensive damage. Table 20 presents the outcomes regarding the remaining weight percentage of samples with a crack width of 0.01" and no applied voltages.

		0.01						
	Days	***0***	***30***	***60***	***90***	***120***	***150***	***180***
0 Voltage	**remaining weight of 2,000 ppm**	*100*	*99.7*	*99.4*	*99.2*	*98.9*	*98.5*	*98.2*
	remaining weight of 30,000 ppm	*100*	*99.5*	*99.1*	*98.5*	*97.9*	*97.4*	*97.0*
	remaining weight of 100,000 ppm	***100***	***99.0***	***98.1***	***97.1***	***95.7***	***94.1***	***92.6***

After 180 days, the samples exposed to a concentration of 2,000 ppm experienced a weight loss of 1.8%, with 98.2% of the weight remaining. Similarly, the samples subjected to 30,000 ppm exhibited a 3% weight loss. In contrast, the samples exposed to 100,000 ppm showed a weight loss of 7.4%, four times higher than the 2,000 ppm concentration and 2.47 times higher than the 30,000 ppm concentration. These results indicate a correlation analysis between the solution concentration and the remaining weight at each time point. The Pearson correlation coefficient can be employed to determine the strength and direction of the linear relationship.

The obtained correlation coefficients are as follows and illustrated in Table 21.

Table 20. Pearson Correlation Coefficient for Different Solutions

	0	30	60	90	120	150	180
2,000 ppm	*1.000*	*-0.992*	*-0.990*	*-0.988*	*-0.985*	*-0.981*	*-0.979*
30,000 ppm	*1.000*	*-0.998*	*-0.997*	*-0.996*	*-0.995*	*-0.993*	*-0.992*
100,000 ppm	*-0.999*	*-0.999*	*-0.999*	*-0.998*	*-0.998*	*-0.997*	*-0.997*

The negative correlation coefficients observed for all time points between the solution concentration and remaining weight suggest that increasing concentration decreases remaining weight.

To further analyze the data, an analysis of variance (ANOVA) was conducted to determine if significant differences exist in the remaining weight among the various solution concentrations. This analysis helps identify the concentration with the most significant impact on remaining weight. The ANOVA test examines whether there are significant differences in means between groups (i.e., different solution concentrations). The p-value resulting from the ANOVA test determines the presence of significant differences among the concentrations.

The ANOVA test indicates a significant difference among the solution concentrations (p-value < 0.05), confirming that the concentrations influence the remaining weight.

Post-hoc tests such as the Tukey HSD (Honestly Significant Difference) test were performed to compare pairwise and identify which concentrations significantly differ regarding remaining weight. The Tukey HSD test yielded the following results, and is presented in Table 22.

Table 21. Tukey HSD Results for Different Solutions

Group 1	Group 2	mean diff	p-adj	reject
2,000 ppm	*30,000 ppm*	*-0.385*	*0.001*	*True*
2,000 ppm	*100,000 ppm*	*-0.739*	*0.001*	*True*
30,000 ppm	*100,000 ppm*	*-0.354*	*0.001*	*True*

The Tukey HSD test demonstrates that all pairwise comparisons between solution concentrations exhibit statistically significant differences (p-value < 0.05). This implies that significant disparities in remaining weight exist between all pairs of solution concentrations.

So, the ANOVA test confirms a significant difference in remaining weight among the solution concentrations. The Tukey HSD test further reveals that each solution concentration significantly differs from the others. Based on the Tukey HSD test results, it can be determined which solution concentration exerts a greater influence on remaining weight and corrosion rate.

When comparing the mean differences between the solution concentrations, the following observations can be made:

These mean differences represent the average variation in remaining weight between the solution concentrations. Since the mean differences are negative, it indicates that as the solution concentration increases, the remaining weight decreases, suggesting a higher corrosion rate.

The percentage weight loss between the lowest concentration (2,000 ppm) and the highest concentration (100,000 ppm) can be calculated to quantify the difference. The percentage weight loss formula is as follows:

Percentage weight loss = (Remaining weight difference / Initial weight) × 100

For the comparison between 2,000 ppm and 100,000 ppm:

Remaining weight difference = 0.739 Initial weight = 100 = (0.739 / 100) × 100 = 0.739%. Therefore, the percentage of weight loss is approximately 0.739%. This indicates that the corrosion rate at 100,000 ppm is approximately 0.739% higher than the corrosion rate at 2,000 ppm.

Figure 52 illustrates the graphical representation of the results and their corresponding differences.

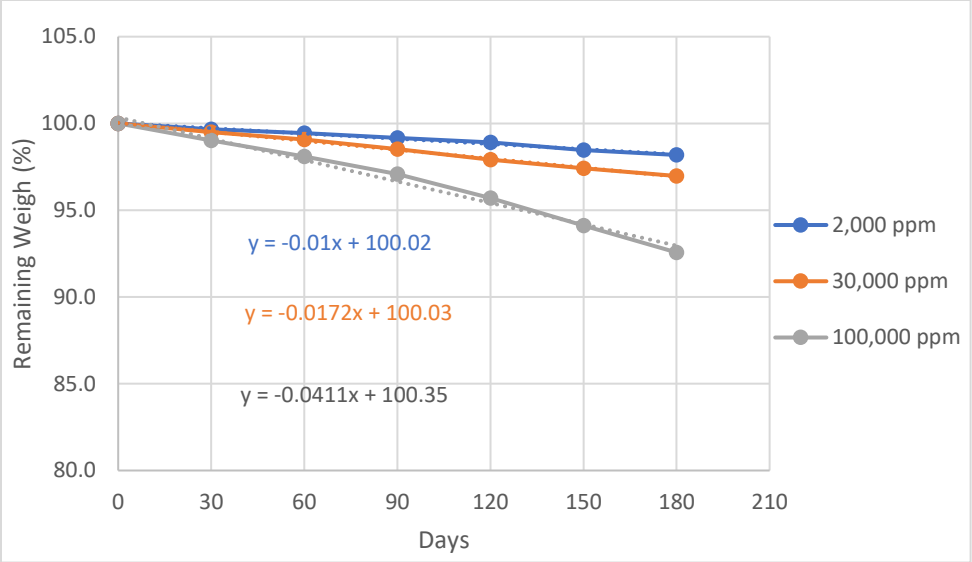

Figure 52. Effect of Sodium Chloride on Corrosion Rate at 0 Volt and 0.01" Crack Width

5.4. Results from SEM & EDX

In this project, the elemental analysis of the samples was conducted using the Energy Dispersive X-ray Spectroscopy (EDX) method. EDX is a detector that employs X-ray fluorescence excitation to identify and quantify the chemical composition of a given sample. It enables both qualitative and quantitative analysis of elements present in the sample. So, a series of steps were undertaken to investigate the samples. After each immersion period, Profometer and remaining weight tests were performed to assess the corrosion rate of the samples. Subsequently, wires were extracted from the cylinders and subjected to Scanning Electron Microscopy (SEM) analysis. The SEM analysis provided visual information about the surface characteristics of the wires. Following the SEM analysis, the samples underwent EDX analysis, which enabled the determination of the chemical composition and quantitative measurements of each element present.

5.4.1. SEM Results

Figure 53-58 presents the surface condition of steel bars obtained from samples immersed in solutions with varying concentrations without applying any voltages. The surface condition is depicted at different magnification levels to provide detailed visual information.

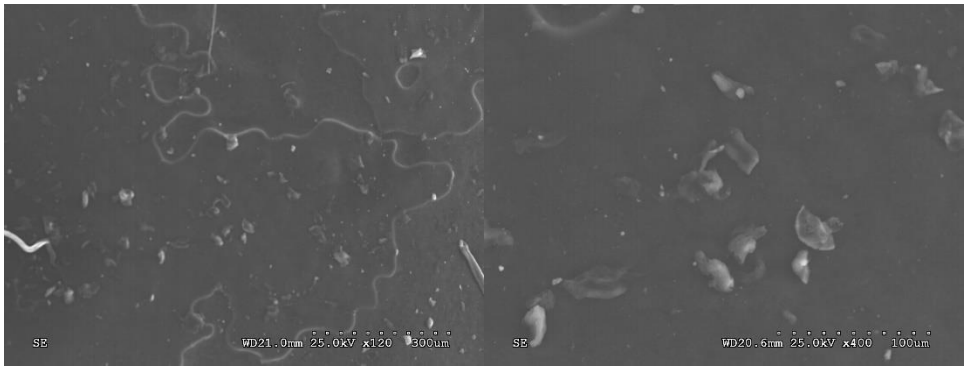

(a) (b)

Figure 53. SEM for 0.01" Crack Width at the Control and 2,000 ppm Under (a) 120x and (b) 400x Magnification

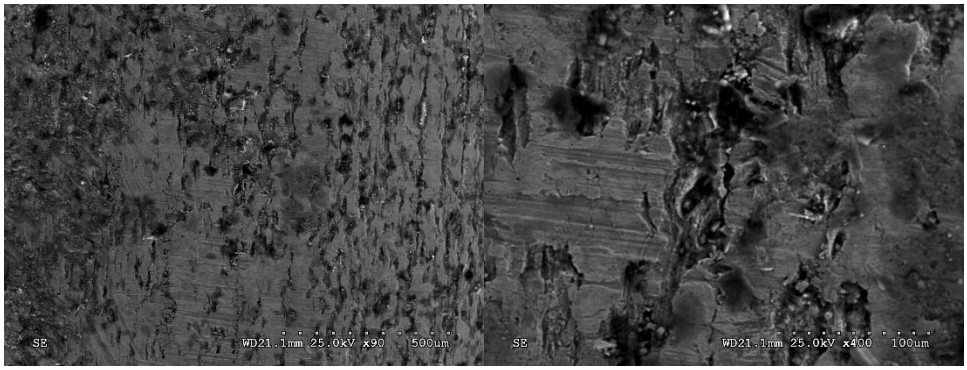

(a) (b)

Figure 54. SEM for 0.01" Crack Width at the Control and 30,000 ppm Under (a) 90x and (b) 400x Magnification

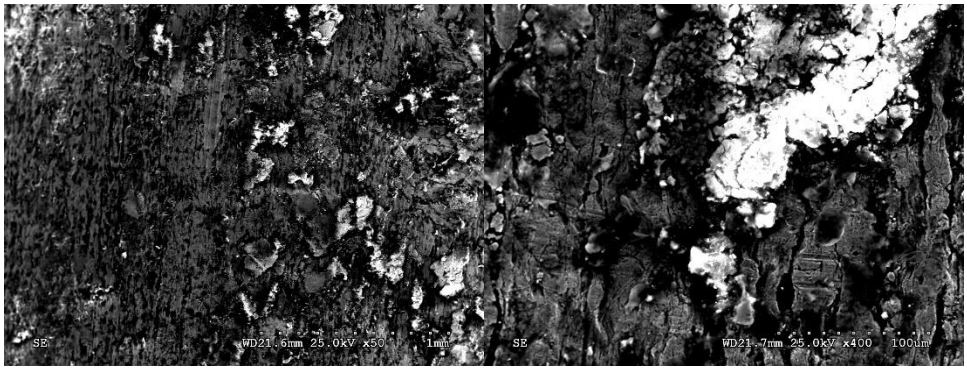

(a) (b)

Figure 55. SEM for 0.01" Crack Width at the Control and 100,000 ppm Under (a) 50x and (b) 400x Magnification

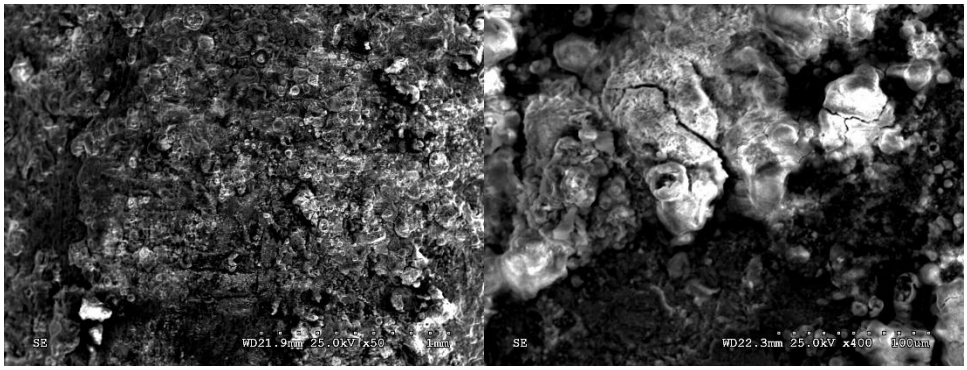

(a) (b)

Figure 56. SEM for 0.1" Crack Width at the Control and 2,000 ppm Under (a) 50x and (b) 400x Magnification

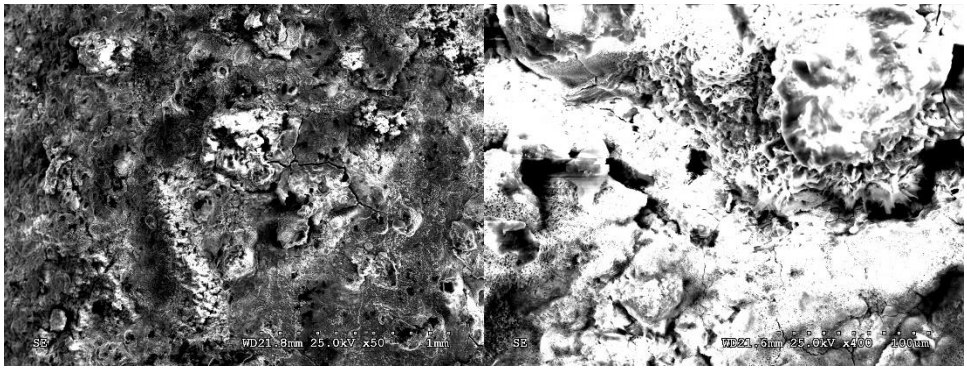

(a) (b)

Figure 57. SEM for 0.1" Crack Width at the Control and 30,000 ppm Under (a) 50x and (b) 400x Magnification

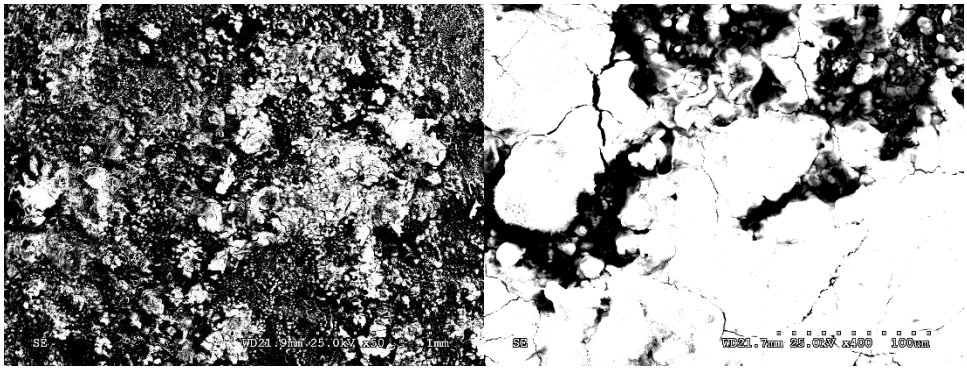

(a) (b)

Figure 58. SEM for 0.1" Crack Width at the Control and 100,000 ppm Under (a) 50x and (b) 400x Magnification

The SEM results and corresponding graphs illustrate the presence of small spots on the images, which indicate the rust spots. These spots reflect the localized corrosion areas on the steel bars' surface. Upon closer analysis, it is observed that as the crack width and concentration of the solution increase, the density of these spots becomes more pronounced. This indicates a higher rate of corrosion in those specific regions. The increased density of these spots signifies a greater extent of localized corrosion occurring on the surface of the steel bars.

This phenomenon can be attributed to several factors. Firstly, an increase in crack width provides more exposure of the steel surface to the corrosive environment, thereby facilitating the initiation and progression of corrosion processes. Secondly, an increase in the concentration of the solution introduces more corrosive agents, such as chloride ions, which accelerate the corrosion rate by promoting electrochemical reactions.

5.4.2. EDX Results

Within the context of corrosion analysis utilizing Energy-Dispersive X-ray Spectroscopy (EDX), the reported relative percentages of carbon (C), oxygen (O), and iron (Fe) in the analyzed sample

provide insights into the elemental composition. Carbon content significantly influences the corrosion behavior of steel, as higher levels can diminish corrosion resistance and increase vulnerability to corrosion mechanisms like galvanic or localized pitting corrosion. Oxygen's role is closely tied to forming corrosion products on steel surfaces. When steel is exposed to oxygen and moisture, the initial stages of corrosion involve the creation of iron oxide (commonly referred to as rust) on the surface. Iron, the primary constituent of steel, typically represents the highest proportion in such compositions. Table 23 presents the numerical results of samples with 0.01" crack width immersed in 2,000 ppm obtained from the EDX analysis, providing information on the measured quantities of each element. Figure 59 accompanies the numerical results, offering a graphical representation of the EDX data, which aids in visualizing the elemental composition and any variations within the samples.

Table 22. Element Analysis of 0.01" Crack Width at Control and 2,000 ppm

Element Line	Net Counts	Weight %	Norm. Wt.%	Atom %
C K	13826	21.52	21.52	45.99
O K	26028	14.13	14.13	22.67
Na K	2007	1.14	1.14	1.28
Al K	1581	0.29	0.29	0.28
Si K	5250	0.73	0.73	0.67
S K	2941	0.31	0.31	0.24
Cl K	2391	0.24	0.24	0.18
K K	1066	0.10	0.10	0.07
Ca K	21398	2.13	2.13	1.36
Cr K	845	0.10	0.10	0.05
Mn K	1787	0.32	0.32	0.15
Fe K	312436	58.18	58.18	26.74
Ni K	1099	0.29	0.29	0.13
Cu K	1714	0.52	0.52	0.21
Total		100.00	100.00	100.00

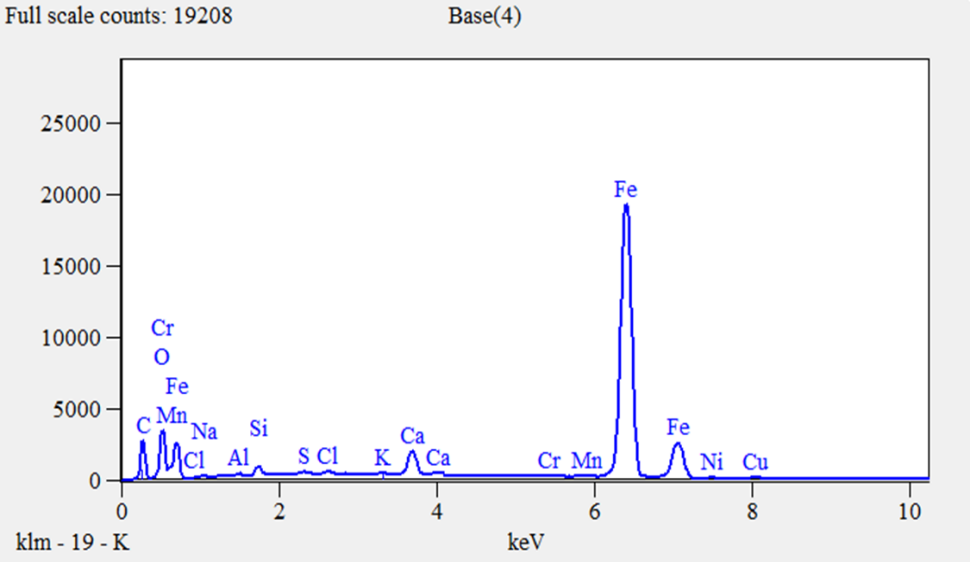

Figure 59. Element Analysis of 0.01" Crack Width at Control and 2,000 ppm

The sample exhibits a carbon content of 21.52%, potentially indicating an enhanced susceptibility to corrosion-related concerns. The presence of 14.13% oxygen in the analyzed sample implies the existence of an oxide layer or rust on the steel surface. In the analyzed sample, iron (Fe) accounts for 58.18%. Iron is the foundation for forming protective oxide layers on steel surfaces as a barrier against further corrosion.

Table 24 presents the numerical results of samples with 0.01" crack width immersed in 30,000 ppm obtained from the EDX analysis, providing information on the measured quantities of each element. Figure 60 accompanies the numerical results, offering a graphical representation of the EDX data, which aids in visualizing the elemental composition and any variations within the samples.

Table 23. Element Analysis of 0.01" Crack Width at Control and 30,000 ppm

Element Line	Net Counts	Weight %	Norm. Wt.%	Atom %
C K	28159	19.03	19.03	40.48
O K	51663	27.74	27.74	27.37
Na K	8193	2.35	2.35	2.15
Mg K	0	0.00	0.00	0.00
Al K	1587	0.15	0.15	0.12
Si K	5564	0.41	0.41	0.31
S K	3213	0.18	0.18	0.12
Cl K	16604	0.94	0.94	0.56
K K	1831	0.10	0.10	0.05
Ca K	41085	2.37	2.37	1.25
Cr K	1101	0.08	0.08	0.03
Mn K	2099	0.22	0.22	0.08
Fe K	376568	45.19	45.19	15.58
Ni K	1129	0.17	0.17	0.06
Cu K	1549	0.27	0.27	0.09
Total		100.00	100.00	100.00

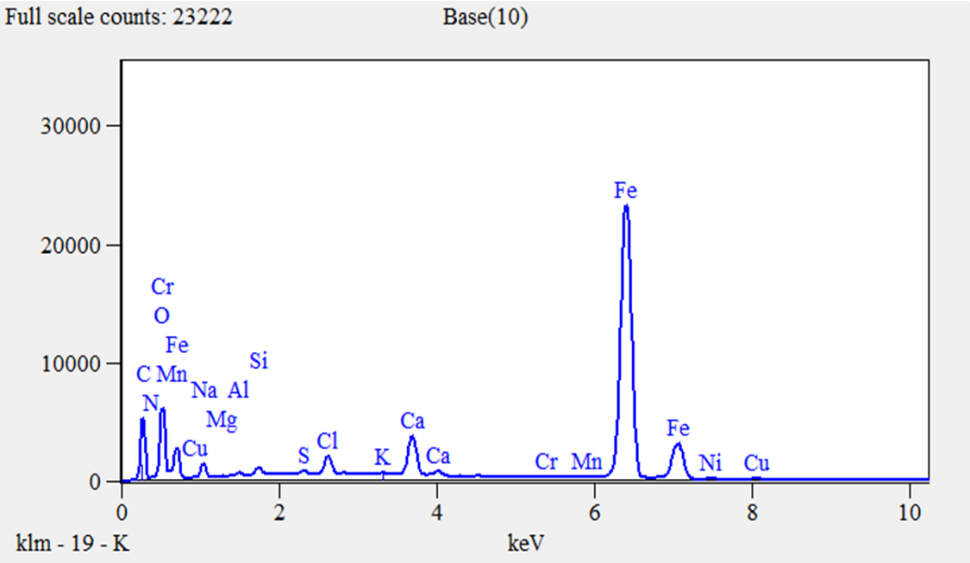

Figure 60. Element Analysis of 0.01" Crack Width at Control and 30,000 ppm

Table 25 presents the numerical results of samples with 0.01" crack width immersed in 100,000 ppm obtained from the EDX analysis, providing information on the measured quantities of each element. Figure 61 accompanies the numerical results, offering a graphical representation of the EDX data, which aids in visualizing the elemental composition and any variations within the samples.

Table 24. Element Analysis of 0.01" Crack Width at Control and 100,000 ppm

Element Line	Net Counts	Weight %	Norm. Wt.%	Atom %
C K	11072	14.04	14.04	21.93
O K	125310	35.75	35.75	53.28
Na K	1853	0.65	0.65	0.67
Mg K	310	0.05	0.05	0.05
Al K	4764	0.54	0.54	0.48
Si K	11656	1.00	1.00	0.85
S K	3811	0.25	0.25	0.19
Cl K	11951	0.77	0.77	0.52
K K	2959	0.18	0.18	0.11
Ca K	61976	4.03	4.03	2.40
Cr K	1503	0.13	0.13	0.06
Mn K	2353	0.27	0.27	0.12
Fe K	369223	40.19	40.19	19.30
Cu K	777	0.15	0.15	0.06
Total		100.00	100.00	100.00

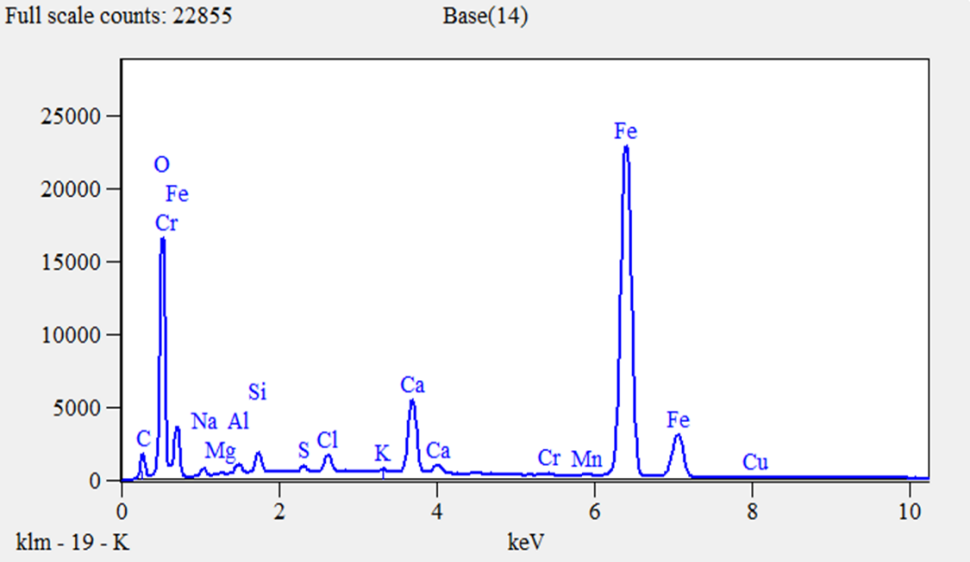

Figure 61. Element Analysis of 0.01" Crack Width at Control and 100,000 ppm

Based on the information provided, Figures 62 and 63 illustrate the chemical composition of Oxygen, Iron, and Carbon for different concentration solutions at zero Volts.

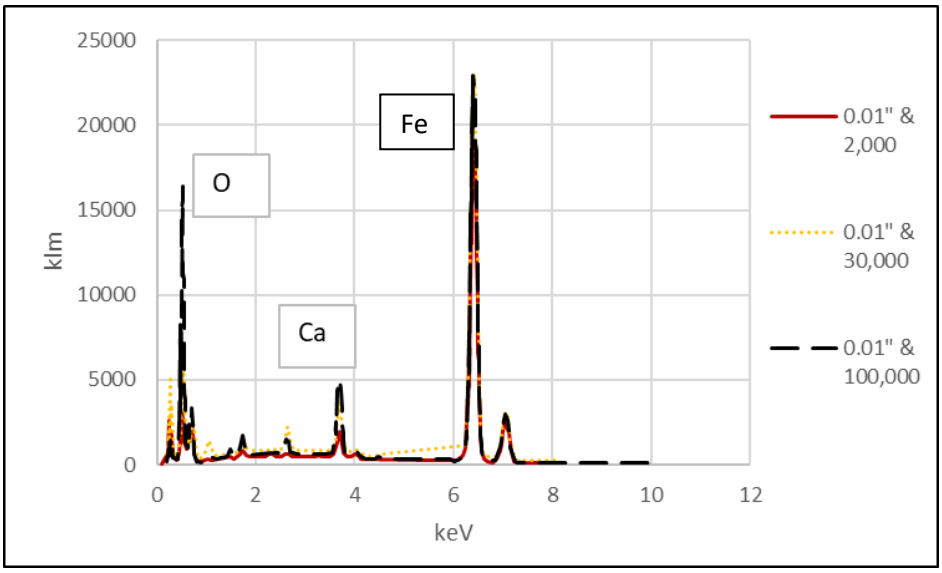

Figure 62. Elemental Analysis of 0.01" with Different Concentration Solutions at 0 Volt

The graph indicates that as the concentration of the solution increases from 2,000 ppm to 100,000 ppm, the percentage of oxygen increases from 15% to 36%, while the percentage of iron decreases from 59% to 41%.

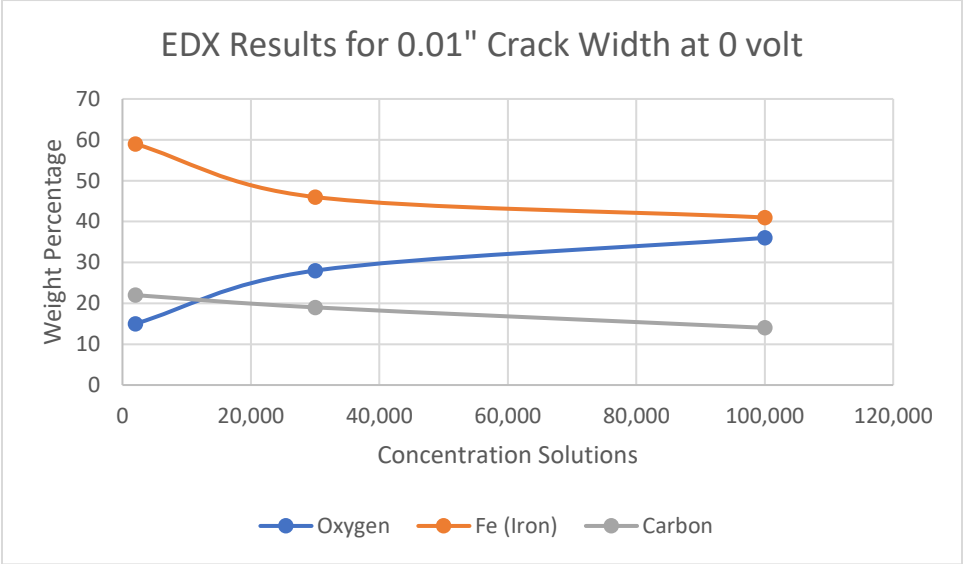

Figure 63. EDX Results for 0.01" Crack Width and 0 Volt

The observed increase in the percentage of oxygen with increasing solution concentration suggests that a higher concentration leads to greater oxygen availability. This can be attributed to the increased dissolved oxygen in the solution. The dissolved oxygen can then interact with the metallic surface, potentially in corrosion processes. However, Regarding the corrosion rate, a high oxygen content observed in EDX results has the potential to indicate an accelerated corrosion rate. Oxygen is required for corrosion, and higher oxygen levels provide a more conducive environment for oxidation reactions.

Conversely, the decrease in the percentage of iron with increasing concentration of the solution indicates a reduction in the iron content relative to other elements in the system. This could be due to the formation of corrosion products or the preferential dissolution of iron ions into the solution. The reduction in iron content suggests that iron corrosion is occurring, resulting in the depletion of iron atoms from the metallic surface. This indicates that the material has undergone more extensive oxidation reactions, forming iron oxides (such as rust).

The observed trend in the graph indicates that as the concentration of the solution increases, the corrosion potential also increases. The increased availability of oxygen can promote the corrosion processes, while the decrease in iron content signifies iron loss due to corrosion.

Figures 64-67 present the results obtained from the Energy Dispersive X-ray (EDX) analysis, which displays the graphical representation of chemical components at concentrations of 2,000 ppm and 100,000 ppm for various crack widths. The purpose of comparing different crack widths in different solutions is to examine the relationship between crack width, solution concentration, and the presence of oxygen, which contributes to higher corrosion rates and accelerates the corrosion process.

The results of the EDX analysis indicate the presence and quantity of oxygen in the tested samples. Oxygen plays a crucial role in the corrosion process, as it is involved in various electrochemical reactions that lead to the degradation of the reinforced steel. Oxygen is an important factor in determining the corrosion rate and the rate at which the process progresses. The results reveal that as the crack width increases and the chloride concentration in the solution rises, the amount of detected oxygen also increases. This relationship suggests that wider cracks and higher chloride concentrations lead to higher oxygen availability within the system.

Consequently, this higher oxygen level increases the corrosion rate and accelerates the overall corrosion process. This finding aligns with prior knowledge that elevated oxygen levels are associated with increased corrosion activity and a more rapid progression of the corrosion process.

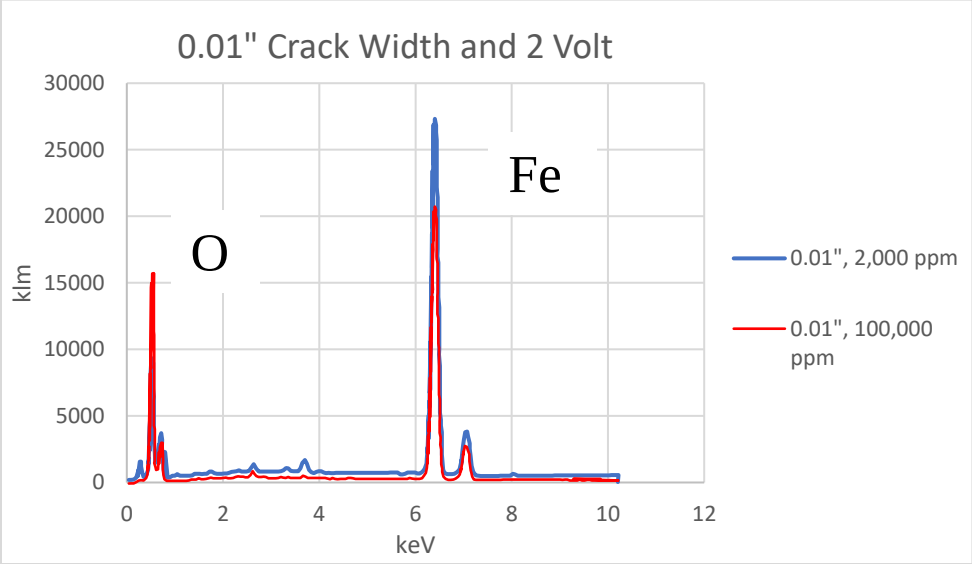

Figure 64. EDX Results for 0.01" Crack Width and 2 Volt

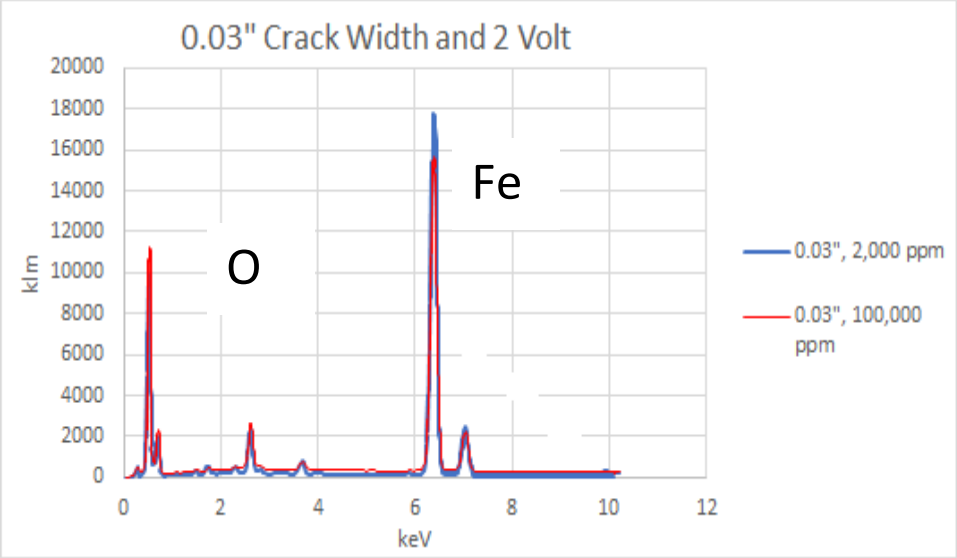

Figure 65. EDX Results for 0.03" Crack Width and 2 Volt

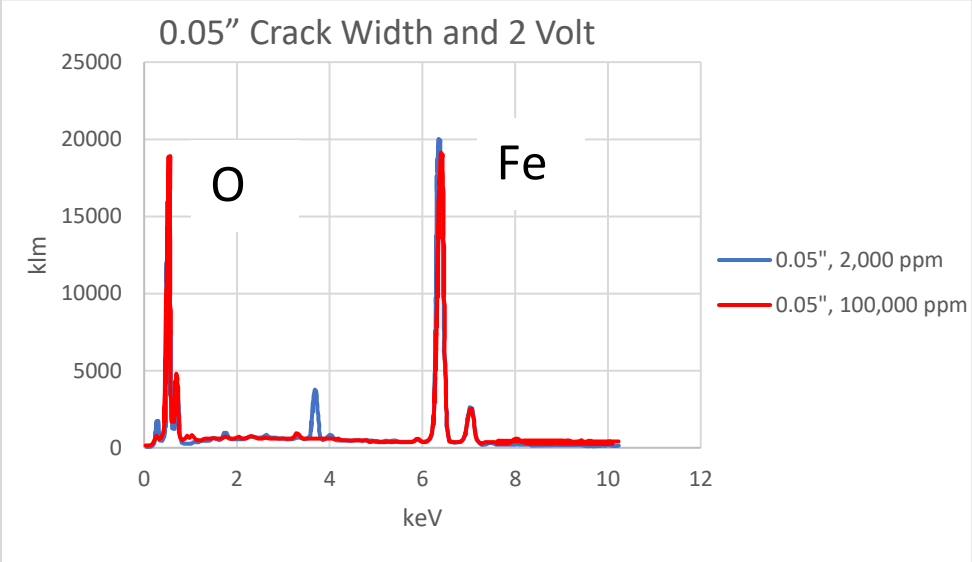

Figure 66. EDX Results for 0.05" Crack Width and 2 Volt

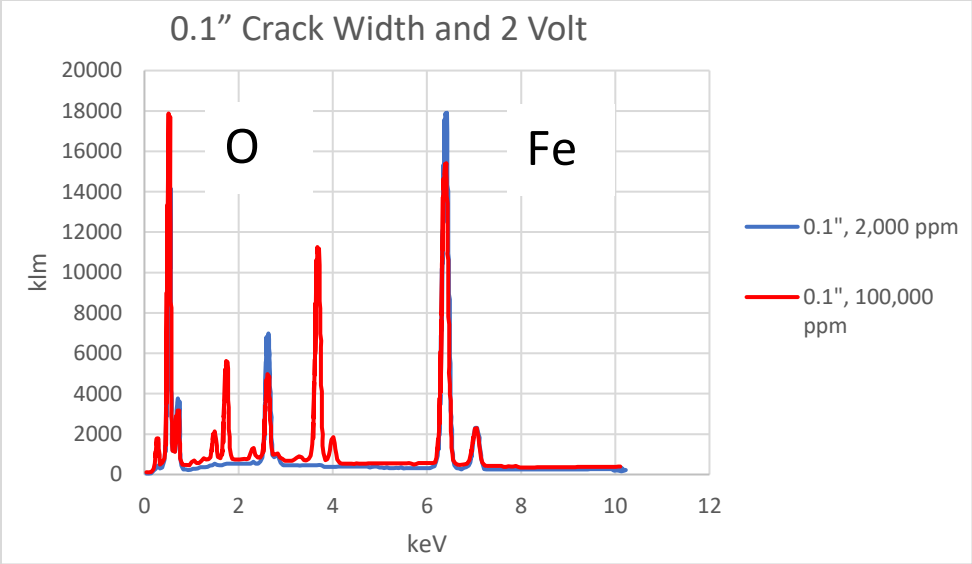

Figure 67. EDX Results for 0.1" Crack Width and 2 Volt

5.5. Results from Different Rebar Sizes

The corrosion rates between two different sizes of rebar used in the project (0.194" diameter for the 24" pipe and 0.226" diameter for the 96" pipe) subjected to 8 Volt are presented in Table 26.

Days	**0**	**30**	**60**	**90**	**120**	**150**	**180**
Remaining Weight for 8 Volt 24"	*100*	*66.6*	*57.5*	*47.1*	*36.6*	*26.3*	*11.3*
Remaining Weight for 8 Volt 96"	***100***	***73.4***	***68.4***	***61.3***	***46.4***	***39.0***	***21.9***

Based on the tabulated data, the weight loss of samples with a rebar diameter of 0.226 inches after 180 days was 78%. In contrast, samples with a rebar diameter of 0.194 inches exhibited a weight loss of 88.7%. This indicates that larger-sized rebars experienced comparatively 11.36% lower levels of corrosion under identical time and environmental conditions. Figure 68 displays a graphical representation of the corrosion rate concerning distinct rebar sizes.

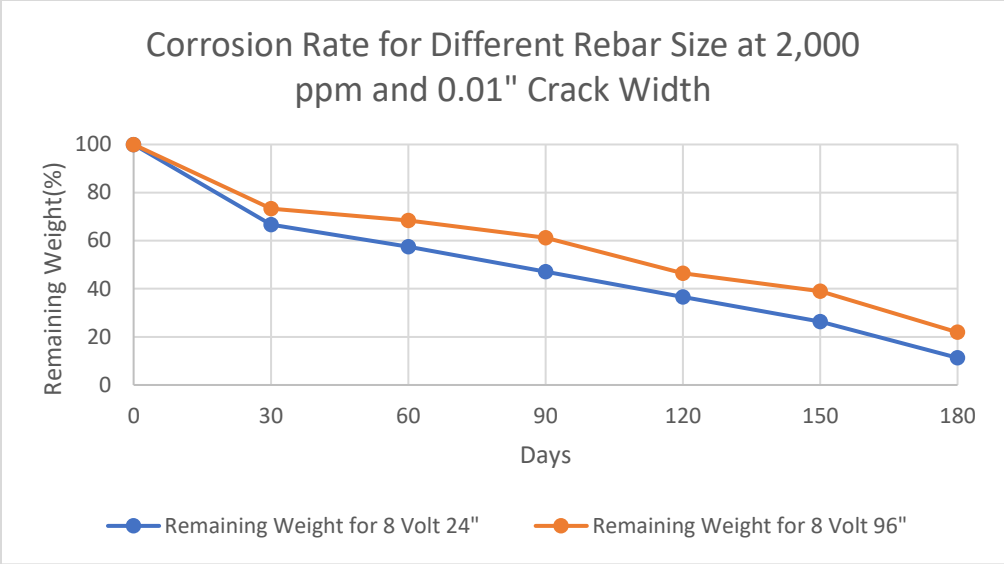

Figure 68. Effect of Rebar Size on Corrosion Rate at 2,000 ppm and 0.01" Crack Width.

5.6. Results from Autogenous Healing

This study involved a set of samples with varying cement ratios in their mix design. These samples were immersed in a 2,000-ppm solution and tested monthly for up to six months. The objective was to examine the closure of cracks with widths of 0.01", 0.03", and 0.05" over time. The results presented in Table 27 indicate that samples with higher cement content exhibit greater crack closure than those with lower cement ratios.

Table 25. Crack Closer Measurements for High and Low Cement Content

		0	30	60	90	120	150	180
0.01"	*HC Ratio*	*0.01*	*0.0097*	*0.0095*	*0.0092*	*0.0088*	*0.0085*	*0.0083*
	LC Ratio	*0.01*	*0.0098*	*0.0096*	*0.0094*	*0.0092*	*0.0089*	*0.0087*
0.03"	*HC Ratio*	*0.03*	*0.0294*	*0.0289*	*0.0282*	*0.0276*	*0.0271*	*0.0266*
	LC Ratio	*0.03*	*0.0296*	*0.0291*	*0.0286*	*0.0281*	*0.0277*	*0.0272*
0.05"	*HC Ratio*	*0.05*	*0.0496*	*0.0491*	*0.0485*	*0.048*	*0.0476*	*0.0471*
	LC Ratio	*0.05*	*0.0497*	*0.0494*	*0.049*	*0.0486*	*0.048*	*0.0476*

For the 0.01" crack width, after six months, the high cement ratio samples displayed a 17% closure due to autogenous healing. In contrast, the low cement ratio samples achieved a 13% closure. Similar trends were observed for the 0.03" and 0.05" crack widths. The high cement ratio samples exhibited 11.3% and 5.8% closure after six months, respectively, while the low cement ratio samples displayed lower closure percentages of 9.3% and 5% for the respective crack widths.

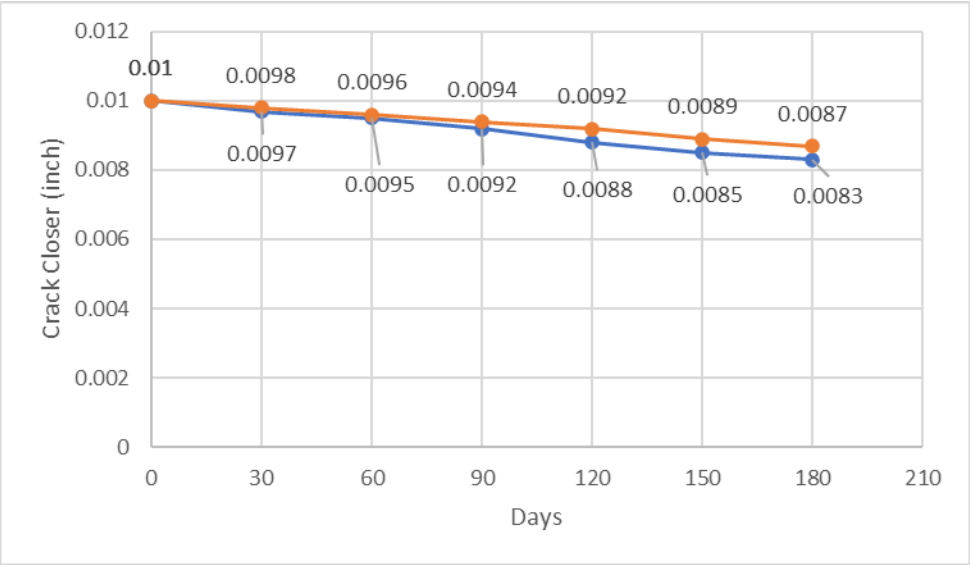

Figure 69. Effect of Cement Amount on Autogenous Healing

The results illustrated in Figure 69 revealed that the healing process was more effective and faster for lower crack widths (0.01") than wider cracks. At a crack width of 0.01", the amount of crack healing for a high cement ratio is found to be 4.8% higher than the healing observed in a low cement ratio. Moreover, for crack widths of 0.03" and 0.05", the healing percentage for the high cement ratio is 2.2% and 1.06% higher than that for the lower cement ratio.

CHAPTER 6. STATISTICAL ANALYSIS

6.1. Overview

The statistical analysis conducted in this study aimed to assess the corrosion rate of reinforced concrete samples under different conditions. The study considered four variables: Days, Concentration Solutions, Crack Width, and Voltages. The output variable of interest was the Remaining Weight percentage of the samples, which indicates the corrosion extent.

Several statistical techniques were applied to analyze these data, such as:

ANOVA:

An analysis of variance (ANOVA) can be performed to determine the significant effects of the variables on the remaining weight percentage. ANOVA assesses whether there are significant differences in the corrosion rates among different levels of the variables. For example, it can reveal whether there are significant variations in the remaining weight percentage based on different crack widths or applied voltages.

Post-Hoc tests:

Following ANOVA, post-hoc tests such as Tukey's HSD (Honest Significant Difference) can be conducted to make pairwise comparisons between the levels of the variables. These tests help identify specific combinations of crack widths, voltages, or concentration solutions that exhibit significant differences in corrosion rates.

Regression analysis:

Regression models can quantify the relationships between the variables and the remaining weight percentage. Multiple regression analysis can be used to assess the combined effects of crack width,

applied voltage, and concentration solutions on the corrosion rate. The regression analysis can provide insights into the relative contributions of each variable to the corrosion process.

Interaction effects:

Examining the interaction effects between the variables is essential. For example, the interaction between crack width and applied voltage can indicate whether the corrosion rate is affected differently depending on the crack width. Interaction effects can be analyzed through ANOVA or regression analysis, providing a deeper understanding of the complex relationships among the variables.

6.2. Analysis of Variance

An analysis of variance (ANOVA) was conducted to examine whether significant differences exist among the variable levels under consideration. The ANOVA process involves several steps to evaluate the null hypothesis (H0), which assumes no significant difference in the means of the variable levels, against the alternative hypothesis (HA), which suggests a significant difference exists.

Hypotheses:

The null hypothesis (H0) states that there are no significant differences in the means of the variable levels.

$$(H0): \mu_1 = \mu_2 = \mu_3 = ... = \mu_k$$

Where:

μ represents the population means of each group or level.

While the alternative hypothesis (HA) asserts that there is a significant difference among the means.

Calculation of Sums of Squares (SS):

The sums of squares are calculated to understand the variability in the data. The total sum of squares (SST) represents the overall variation in the data, the sum of squares between (SSB) measures the variation between the different groups or levels of the variable, and the sum of squares error (SSE) quantifies the variation within each group.

$$SST = \sum (X_{ij} - \bar{X})^2$$

Where:

X_{ij} is each observation.

$\bar{X}$ is the overall mean.

$$SSB = \sum (n_j \times (\bar{X}_j - \bar{X})^2)$$

Where:

n_j is the number of observations in each group or level.

$\bar{X}_j$ is the mean of each group or level.

$$SSE = \sum \sum (X_{ij} - \bar{X}_j)^2$$

Where:

X_{ij} is each observation.

$\bar{X}_j$ is the mean of each group or level.

Calculation of Degrees of Freedom (DF)*:*

Degrees of freedom are computed to determine the appropriate critical values. The degrees of freedom between (DFB) equals the number of variable levels minus one. In contrast, the degrees of freedom error (DFE), is calculated by subtracting the total number of observations from the number of variable levels.

$$DFB = k - 1$$

k is the number of groups or levels.

$$DFE = N - k$$

N is the total number of observations.

Calculation of Mean Squares (MS):

The mean squares are computed by dividing the respective sums of squares by their corresponding degrees of freedom. The mean square between (MSB) is obtained by dividing SSB by DFB, and the mean square error (MSE) is derived by dividing SSE by DFE.

$$MSB = SSB / DFB$$

$$MSE = SSE / DFE$$

Calculation of the F-value and p-value:

The F-value in ANOVA is the ratio of the between-group variance to the within-group variance. It is calculated by dividing the mean square between (MSB) by the mean square error (MSE). The

F-value measures the extent to which the differences between groups exceed the differences expected by chance within the groups.

$$F = MSB / MSE$$

The p-value, calculated based on the F-distribution table, provides information about the level of significance associated with the observed F-value. It represents the probability of obtaining the observed F-value or a more extreme value if the null hypothesis (no difference among the groups) is accurate. A smaller p-value indicates more substantial evidence against the null hypothesis. Table 28 illustrates the F distribution table for four degrees of freedom. The complete F distribution table is in the Statistical Tables for the Social, Biological, and Physical Sciences book.

Table 26. F- Distribution Table

Degrees of Freedom (df_1, df_2)	**α = 0.05**	**α = 0.01**	**α = 0.001**
(1, 1)	*161.45*	*647.79*	*3,841.00*
(1, 2)	*18.51*	*164.41*	*1,964.79*
(2, 1)	*4.35*	*9.88*	*31.60*
(2, 2)	*3.19*	*7.38*	*22.16*
(3, 1)	*3.28*	*6.94*	*18.51*
(3, 2)	*2.61*	*5.54*	*14.26*
(3, 3)	*2.37*	*4.75*	*12.92*
(4, 1)	*2.78*	*5.61*	*14.97*
(4, 2)	*2.44*	*4.89*	*12.75*
(4, 3)	*2.27*	*4.46*	*11.66*
(4, 4)	*2.16*	*4.04*	*10.92*

df_1 (Degrees of Freedom in the Numerator):

It represents the number of groups or conditions being compared. In the context of ANOVA, it is typically the number of treatment groups minus 1.

df_2 (Degrees of Freedom in the Denominator):

It represents the degrees of freedom associated with the error term or residual variability. In ANOVA, it is the total number of observations minus the total number of treatment groups.

Alpha (α) represents the significance level or the probability of committing a Type I error. It is typically set before conducting a hypothesis test or statistical analysis. The significance level, alpha, determines the threshold for rejecting the null hypothesis. Suppose the p-value (probability value) obtained from the statistical test is less than or equal to alpha. In that case, the null hypothesis is rejected in favor of the alternative hypothesis. Commonly used alpha values are 0.05 (5%) and 0.01 (1%).

It is considered statistically significant if the p-value does not exceed the chosen significance level (e.g., 0.05). In such cases, the null hypothesis is rejected, and it can be concluded that there are significant differences among the groups. Conversely, suppose the p-value is more significant than the significance level. In that case, it is not statistically significant, implying that the observed differences between groups could be due to random chance.

Determination of the Critical F-value:

To compare the calculated F-value, a critical F-value is determined from the F-distribution table based on the degrees of freedom for between-groups (DFB) and error (DFE) at the desired significance level (e.g., alpha = 0.05).

Comparison of the Calculated F-value with the Critical F-value:

The calculated F-value is compared to the critical F-value. The null hypothesis is rejected if the calculated F-value exceeds the critical F-value, indicating a significant difference among the variable levels.

6.3. Post-Hoc Tests (Tukey's HSD)

If the ANOVA indicates a significant difference among the variable levels, a post hoc test, such as Tukey's honestly significant difference (HSD) test, compares the means pairwise and identifies which groups differ significantly.

The HSD value is calculated using the critical value (q) from the Studentized Range Distribution table or statistical software to determine the significance of differences between the means, the mean square error (MSE), and the number of observations per group (n). By comparing the absolute difference between the means of each pair to the HSD value, it is possible to identify significantly different means.

$$HSD = q \times \sqrt{(\frac{MSE}{n})}$$

Where:

q is the critical value from the Studentized Range Distribution table or statistical software.

MSE is the mean square error.

n is the number of observations per group.

Example of ANOVA and HSD Calculation for this study project

Table 29 presented the remaining weight percentage of samples immersed at 30,000 ppm and a crack width of 0.01 inches across different voltage levels. Analysis of variance (ANOVA) and a post hoc test (Tukey's HSD) were performed to compare the impact of various voltages on the samples.

Table 27. Effect of Voltages at 30,000 ppm and 0.01" Crack Width

0.01"			0	30	60	90	120	150	180
30,000 ppm	*0 V*	*Remaining Weight (%)*	*100.0*	*99.5*	*99.1*	*98.5*	*97.9*	*97.4*	*97.0*
	2 V	*Remaining Weight (%)*	*100.0*	*95.4*	*90.7*	*87.4*	*81.1*	*75.1*	*70.5*
	4 V	*Remaining Weight (%)*	*100.0*	*73.7*	*64.1*	*55.7*	*44.8*	*32.1*	*19.9*
	8 V	*Remaining Weight (%)*	*100.0*	*48.9*	*38.7*	*27.0*	*11.6*	*0.0*	*0.0*

Step 1: Calculation of the overall mean

The overall mean is computed by summing the individual values and dividing by the total number of observations:

Overall Mean = 70

Step 2: Calculation of the sum of squares total (SST)

The sum of squares total measures the total variation in the data from the overall mean:

SST = 39,402.6

Step 3: Calculation of the sum of squares between (SSB)

The sum of squares between quantifies the variation between the group means and the overall mean:

SSB = 9,826

Step 4: Calculation of the sum of squares within (SSW) or (SSE)

The sum of squares within measures the variation within each group:

SSE=SSW = 29,576.5

Step 5: Calculation the degrees of freedom

The degrees of freedom are determined based on the number of groups and the total number of observations:

DF(Between) = Number of Groups - 1 = 4 - 1 = 3

DF(Within) = Total Number of Observations - Number of Groups = 28 - 4 = 24

DF(Total) = Total Number of Observations - 1 = 28 - 1 = 27

Step 6: Calculation of the mean squares

The mean squares are obtained by dividing the sum of squares by their respective degrees of freedom:

MS(Between) = SSB / DF(Between) = 9,826 / 3 = 3,275.3

MS(Within) = SSW / DF(Within) = 29,576.5 / 24 = 1,232.3

Step 7: Calculation of the F-statistic

The F-statistic is computed as the ratio of the mean square between to the mean square within:

F = MS(Between) / MS(Within) = 3,275.3 / 1,232.3 = 2.65

Step 8: Determination of the critical value and p-value

Using the F-distribution table for a significance level of alpha = 0.05 and degrees of freedom DF(Between) = 3 and DF(Within) = 24:

The critical value for the F-statistic is 3.35.

The associated p-value for the F-statistic is approximately 0.0708. This value obtained from the Rstudio software, and the corresponding code used to perform the calculations is as follows:

```
# Reshape the data into long format
library(tidyr)
data_long <- data %>%
pivot_longer (cols = -Days, names_to = "Voltage", values_to = "Remaining_Weight")
```

```
# Perform ANOVA
library(stats)
anova_result <- aov (Remaining_Weight ~ Voltage + Days, data = data_long)
summary(anova_result)
```

Step 9: Performance of Tukey's HSD test

The results rejected the null hypothesis since the calculated F-statistic is lower than the critical value. Consequently, Tukey's HSD test did not proceed.

```
# Perform pairwise comparisons using emmeans
library(emmeans)
pairwise_result <- emmeans (anova_result, ~ Voltage, adjust = "tukey")
pairwise_result
```

6.4. Regression Analysis

Regression analysis is a statistical technique to model the relationship between a dependent variable (Remaining Weight Percentage) and one or more independent variables (Days, Concentration Solutions, Crack Width, and Voltages). It is commonly used for predicting or estimating the dependent variable's value based on the independent variables' values.

The dependent variable, also known as the response variable or outcome variable, is the variable of interest that will be predicted. The independent variables, also called predictor variables or explanatory variables, are the variables that have an impact on the dependent variable.

Regression analysis aims to find the best-fitting mathematical model that describes the relationship between the dependent and independent variables.

The most common form of regression analysis is linear regression, which assumes a linear relationship between the variables. In linear regression, the relationship between the dependent and independent variables is represented by a straight line. The line is determined by estimating the coefficients (slope and intercept) that minimize the differences between the dependent variable's observed values and the model's predicted values.

Regression analysis can be used for various purposes, such as:

Prediction*:*

Given the values of the independent variables, the model can be used to predict the value of the dependent variable for new or future observations.

Estimation:

Regression analysis can provide estimates of the coefficients, which can help determine the strength and direction of the relationships between variables.

Hypothesis testing*:*

Regression analysis can test the significance of the relationships between variables and determine if they are statistically significant.

Understanding relationships*:*

Regression analysis can help identify the strength and direction of the relationships between variables, allowing to understand how changes in one variable may affect the other.

Regression analysis assumes certain assumptions, such as linearity, independence of errors, and homoscedasticity (constant variance of errors). There are also different types of regression analysis, including multiple regression (with multiple independent variables), polynomial regression (allowing for nonlinear relationships), and logistic regression (used for binary outcomes).

Python's machine-learning capabilities will be utilized for this project to develop the code and determine each variable's best model, equations, and coefficients.

6.5. Prediction Models

A prediction model, or a forecasting or predictive model, is a mathematical or computational tool used to make predictions or projections about future outcomes based on available data and patterns. It is a way of estimating what is likely to happen in the future based on what has happened in the past.

Prediction models are developed using various techniques and algorithms, depending on the nature of the problem and the available data. These models analyze historical data, identify patterns, and build a mathematical representation of the relationships between the input variables (predictors or features) and the output variable (target or outcome variable).

6.5.1. Using Python to Generate the Linear Regression Model and Equation

To commence the statistical analysis utilizing machine learning techniques in conjunction with the Python programming language, importing the requisite libraries for data manipulation, analysis, and visualization is essential.

The Pandas Library, renowned for its efficacy in data handling, provides efficient data structures and functions to facilitate comprehensive data manipulation. It enables seamless loading and handling of datasets, thereby simplifying the initial data processing stage. Numpy, a fundamental library for numerical computations, supports large, multi-dimensional arrays and an extensive array of mathematical functions. Its capabilities prove particularly advantageous for the numerical computations entailed in statistical analysis. Moreover, the Matplotlib library proves invaluable in generating visualizations, allowing for the creation of various plots and visual aids to enhance data comprehension.

Following the library imports, the subsequent step entails loading the pertinent data. The data collected encompassing the remaining weight at different voltages, crack widths, and concentration solutions throughout the 180-day testing period necessitates systematic tabulation and organization in an Excel file. To accomplish this, the Pandas library within Python is employed for efficient data manipulation and structuring. Executing the corresponding code generates a well-

structured Excel file that can be readily interpreted, serving as the foundation for subsequent analysis and examination.

Proceeding to the next step, correlation analysis explores the interrelationships between variables. One can discern the degree of relationship between the variables by calculating correlation coefficients, which quantify the magnitude and direction of linear associations between pairs of variables. The correlation matrix is computed using the "corr" method provided by the Pandas library. This process facilitates identifying significant positive or negative relationships between variables, providing insights into their potential dependencies and interactions.

Upon completion of the correlation analysis, linear regression is employed to build the prediction model. This statistical technique enables the establishment of relationships between variables and enables the prediction of outcomes based on these relationships.

Subsequently, the regression results are interpreted. After fitting the model, the coefficient values obtained represent the estimated effects of each variable and interaction term on the remaining weight. A positive coefficient signifies a positive relationship, while a negative coefficient denotes a negative relationship. Through careful interpretation of these coefficient values, valuable insights can be gained regarding the influence of variables on the remaining weight.

Visualizations are created to enhance the understanding of the model and its predictions. This involves generating plots and graphs that compare the observed and predicted values. A comprehensive understanding of the model's performance can be obtained by visualizing the alignment between observed and predicted values.

For reference, the written Python code mentioned in Appendix III provides implementation details and serves as a guide for replicating the analysis and constructing the prediction model.

By meticulously following these steps, encompassing data manipulation, correlation analysis, linear regression, interpretation of results, and result visualization, an effective prediction model can be constructed and evaluated, facilitating insightful analysis within an academic context.

6.5.2. Linear Regression Model

The linear regression model was trained, and its performance was evaluated using various statistical measures. Figure 70 depicts a scatter plot that visually represents the relationship between the predicted values from the model and the corresponding observed values. Each data point in the plot corresponds to a specific observation, allowing for a visual assessment of the alignment between the predicted and actual values.

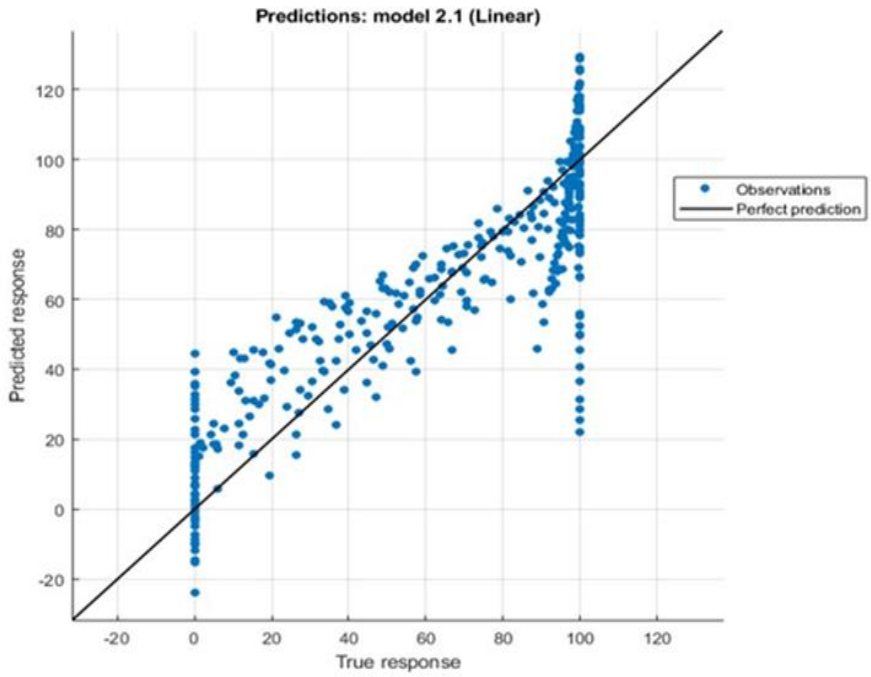

Figure 70. Observed vs. Predicted Values for Remaining Weight at Linear Regression Model

Table 30 represents the results obtained from the linear regression model.

Table 28. Linear Regression Results

RMSE	R-squared	Adjusted R-squared	F-statistic	Prob (F-statistic)
16.88	*0.763*	*0.761*	*289.7*	*5.64e-111*

In regression analysis, the R-squared (coefficient of determination) is a statistical measure that quantifies the proportion of the variance in the dependent variable that the independent variables can explain. It ranges from 0 to 1, where a value of 1 indicates that the model explains all the variability of the dependent variable. In this case, the obtained R-squared value of 0.763 suggests that the independent variables in the model can account for approximately 76.3% of the variation in the remaining weight.

The Root Mean Squared Error (RMSE) is a metric that measures the average distance between the actual values and the corresponding predicted values. In this particular analysis, the calculated RMSE is 16.88. A lower RMSE indicates better accuracy, indicating a minor average error between the predicted and actual values.

The Adjusted R-squared is a modified version that considers the number of predictors in the model. It penalizes the R-squared value for including irrelevant variables and tends to favor models with fewer predictors. In this case, the Adjusted R-squared of 0.761 suggests that approximately 76.1% of the variation in the remaining weight can be attributed to the independent variables after accounting for the number of predictors.

The F-statistic is a measure of the overall significance of the regression model. It compares the fit of the regression model with an intercept-only model (null hypothesis) and assesses whether the inclusion of predictors significantly improves the model fit. A higher F-statistic indicates a more

significant relationship between the predictors and the dependent variable. The obtained F-statistic of 289.7 in this analysis indicates that the regression model is highly significant.

The Prob (F-statistic) represents the p-value associated with the F-statistic. It indicates the probability of observing an F-statistic as extreme as the one calculated if the null hypothesis (no relationship between the predictors and the dependent variable) were true. In this case, the extremely low p-value (5.64e-111) suggests strong evidence against the null hypothesis. This supports the conclusion that the regression model is significant and provides a better fit than an intercept-only model.

The coefficient values and statistical significance of each variable are as follows:

Table 29. Coefficient Values for Each Variable

Constant	*130.43*	*p-value < 0.001*
Days	*-0.25*	*p-value < 0.001*
Concentration Solutions	*-0.0002*	*p-value < 0.001*
Crack Width	*-143.26*	*p-value < 0.001*
Voltages	*-9.14*	*p-value < 0.001*

The coefficients indicate the estimated effect of each variable on the remaining weight. The p-values represent the statistical significance of each coefficient, where a p-value less than 0.05 suggests a significant relationship with the dependent variable.

According to Table 31, the coefficient of each variable shows the effect of that variable on the corrosion rates and remaining weight which is as follows:

Days: The coefficient for Days is -0.2569. It means that for every increase in one unit of Days, the Remaining Weight is estimated to decrease by 0.2569 units.

Concentration Solutions: The coefficient for Concentration Solutions is -0.0002. It shows that the Remaining Weight is estimated to decrease by 0.0002 units for every increase in one unit of Concentration Solutions.

Crack Width: The coefficient for Crack Width is -143.2. It implies that for every increase in one unit of Crack Width, the Remaining Weight is estimated to decrease by 143.2 units.

Voltage: The coefficient for voltage is -9.1. This indicates that the Remaining Weight is estimated to decrease by 9.1 units for every increase in one voltage unit.

6.5.3. The Equation for Linear Regression

The formula for the linear regression model can be derived from the coefficients. In this case, the formula would be:

$$\boldsymbol{Remaining\ Weight} = \mathbf{130.43} - (\mathbf{0.25} \times \boldsymbol{Days}) - (\mathbf{0.0002} \times \boldsymbol{Concentration\ Solutions}) - (\mathbf{143.26} \times \boldsymbol{Crack\ Width}) - (\mathbf{9.14} \times \boldsymbol{Voltage})$$

This equation represents the estimated relationship between the independent variables (Days, Concentration Solutions, Crack Width, and Voltage) and the dependent variable (Remaining Weight) based on the coefficients obtained from the regression analysis.

6.5.4. Interaction Linear Regression

In regression analysis, an interaction effect refers to the combined effect of two or more independent variables on the dependent variable. It occurs when the presence or level of another independent variable influences the relationship between the dependent variable and one independent variable.

The regression model generates Interaction terms by multiplying the variables to include interactions between all variables (Days, Concentration Solutions, Crack Width, and Voltage) are presented in Table 32.

Table 30. Coefficient Values for Interaction Regression

Variable	Coefficient	Std Err	t-value	P > |t|	95% Conf. Interval
Constant	*101.74*	*5.145*	*19.776*	*0.000*	*91.622, 111.858*
Days	*-0.0002*	*0.048*	*-0.004*	*0.997*	*-0.094, 0.093*
Concentration solutions	*3.42e-05*	*9.35e-05*	*0.366*	*0.715*	*-0.000, 0.000*
Crack width	*9.3067*	*88.556*	*0.105*	*0.916*	*-164.866, 183.479*
Voltages	*-1.4933*	*1.219*	*-1.225*	*0.221*	*-3.890, 0.903*
Interaction$_1$	*-1.568e-06*	*8.64e-07*	*-1.818*	*0.071*	*-3.27e-06, 1.32e-07*
Interaction$_2$	*-0.7664*	*0.819*	*-0.936*	*0.350*	*-2.377, 0.844*
Interaction$_3$	*-0.0604*	*0.011*	*-5.365*	*0.000*	*-0.083, -0.038*
Interaction$_4$	*-0.0010*	*0.002*	*-0.611*	*0.541*	*-0.004, 0.002*
Interaction$_5$	*-4.85e-05*	*2.12e-05*	*-2.289*	*0.023*	*-9.02e-05, -6.83e-06*
Interaction$_6$	*-36.3653*	*20.975*	*-1.734*	*0.084*	*-77.619, 4.888*
Interaction$_7$	*1.768e-06*	*1.49e-05*	*0.119*	*0.905*	*-2.75e-05, 3.1e-05*
Interaction$_8$	*1.539e-07*	*1.96e-07*	*0.785*	*0.433*	*-2.31e-07, 5.39e-07*
Interaction$_9$	*0.0153*	*0.194*	*0.079*	*0.937*	*-0.366, 0.397*
Interaction$_{10}$	*0.0003*	*0.000*	*0.811*	*0.418*	*-0.000, 0.001*
Interaction$_{11}$	*1.632e-06*	*3.37e-06*	*0.484*	*0.629*	*-5e-06, 8.26e-06*

These coefficients represent the estimated effect of each variable and interaction term on the dependent variable (Remaining Weight). Some coefficients are not statistically significant (P > |t| > 0.05), suggesting that those variables may not significantly impact the dependent variable.

Figure 71 represents the predicted and observed values obtained from an interaction linear regression analysis. The graph visually displays the relationship between the independent variables involved in the interaction and the corresponding dependent variable.

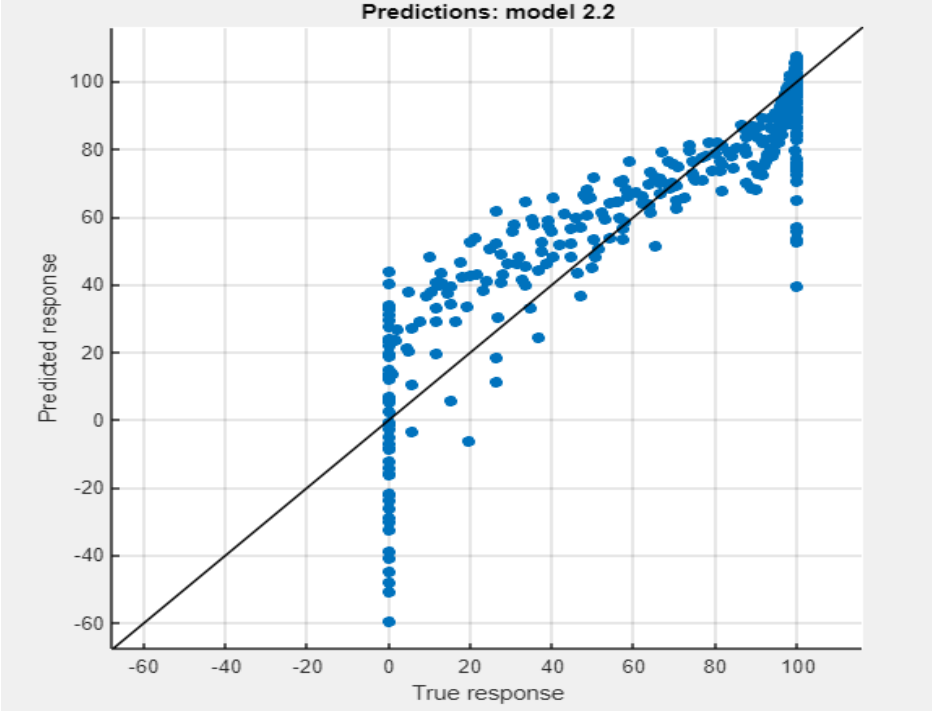

Figure 71. Observed vs. Predicted Values for Remaining Weight at Interaction Linear Regression

For this interaction linear regression model, the calculated RMSE is 16.57, indicating the average prediction error. The R-squared value is 0.81, implying that approximately 81% of the variability in the dependent variable can be explained by the predictors and their interaction. The mean squared error (MSE) is 274.8, providing additional insight into the model's predictive accuracy. The mean absolute error (MAE) is 12.14, representing the average absolute prediction error.

6.5.5. The Equation for Interaction Regression

The regression analysis of coefficients can be used to generate the formula to represent the relationship between the variables and the predicted value of the Remaining Weight. The formula would be:

$$\boldsymbol{Remaining\ Weight}$$

$$= \mathbf{101.74} - (\mathbf{0.0002} \times \boldsymbol{Days}) + \left(\mathbf{3.42}\boldsymbol{e}^{-\mathbf{5}} \times \boldsymbol{Concentration\ Solutions}\right)$$

$$+ (\mathbf{9.3} \times \boldsymbol{Crack\ Width}) - (\mathbf{1.5} \times \boldsymbol{Voltages}) - \left(\mathbf{1.57}\boldsymbol{e}^{-\mathbf{6}} \times \boldsymbol{Interaction}\mathbf{1}\right)$$

$$- (\mathbf{0.76} \times \boldsymbol{Interaction}\mathbf{2}) - (\mathbf{0.06} \times \boldsymbol{Interaction}\mathbf{3}) - (\mathbf{0.001} \times \boldsymbol{Interaction}\mathbf{4})$$

$$- \left(\mathbf{4.85}\boldsymbol{e}^{-\mathbf{5}} \times \boldsymbol{Interaction}\mathbf{5}\right) - (\mathbf{36.36} \times \boldsymbol{Interaction}\mathbf{6})$$

$$+ \left(\mathbf{1.77}\boldsymbol{e}^{-\mathbf{6}} \times \boldsymbol{Interaction}\mathbf{7}\right) + \left(\mathbf{1.54}\boldsymbol{e}^{-\mathbf{7}} \times \boldsymbol{Interaction}\mathbf{7}\right)$$

$$+ \left(\mathbf{1.54}\boldsymbol{e}^{-\mathbf{7}} \times \boldsymbol{Interaction}\mathbf{8}\right) + (\mathbf{0.015} \times \boldsymbol{Interaction}\mathbf{9})$$

$$+ (\mathbf{0.0003} \times \boldsymbol{Interaction}\mathbf{10}) + (\mathbf{1.63}\boldsymbol{e}^{-\mathbf{6}} \times \boldsymbol{Interaction}\mathbf{11})$$

Where:

$Interaction_1$= Days & Concentration Solutions

$Interaction_2$=Days & Crack Width

$Interaction_3$ = Days & Voltage

$Interaction_4$ = Concentration Solutions & Crack Width

$Interaction_5$ = Concentration Solutions & Voltage

$Interaction_6$ = Crack Width & Voltage

$Interaction_7$ = Days & Concentration Solutions & Crack Width

$Interaction_8$ = Days & Concentration Solutions & Voltage

$Interaction_9$ = Days & Crack Width & Voltage

$Interaction_{10}$ = Concentration Solutions & Crack Width & Voltage

$Interaction_{11}$ = Days & Concentration Solutions & Crack Width &Voltage

6.5.6. Neural Network Model

A neural network model is a computational model inspired by the structure and function of biological neural networks, such as the human brain. It is a machine learning model consisting of interconnected nodes, known as neurons, organized in layers. Neural networks are designed to process complex patterns and relationships in data, enabling them to learn and make predictions or classifications.

In a neural network, information flows through the network feedforward. The input layer receives the initial data, which is then passed through hidden layers of neurons. Each neuron in a hidden layer processes the input data using weighted connections and an activation function. The outputs from one layer serve as inputs to the next until the final layer, called the output layer, produces the predicted or classified output.

During the training phase, a neural network learns by adjusting the weights and biases associated with the connections between neurons. This adjustment uses optimization algorithms such as gradient descent, which minimize the difference between the predicted and actual outputs (i.e., the loss or error function).

Figure 72 displays a graphical representation depicting the comparison between the predicted values and the observed data.

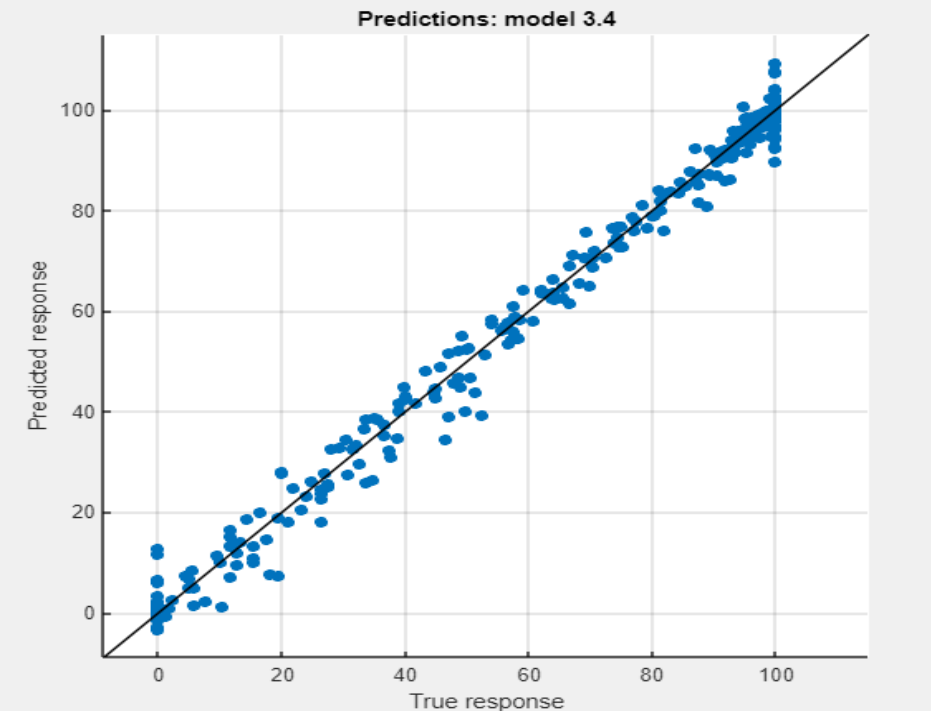

Figure 72. Predicted Values for Remaining Weight at Neural Network Model

For this neural network model, the calculated RMSE is 3.26, indicating a relatively low average prediction error. The R-squared value is 0.99, suggesting that the model's predictions can explain approximately 99% of the variability in the dependent variable. The mean squared error (MSE) is 10.634, providing additional insight into the model's predictive accuracy. The mean absolute error (MAE) measure is 2.21, representing a relatively low average absolute prediction error.

The modeling process used MATLAB software, including data preprocessing, model training, and evaluation. The specific steps undertaken throughout the process can be found in Appendix IV, providing a comprehensive guide for replicating the analysis and understanding the methodology employed.

The trained neural network model allows for predicting the dependent variable, remaining weight while keeping the values of independent parameters such as days, concentration solution, crack

width, and constant voltages. This means that regardless of changes in the independent parameters, the model can generate predictions for the remaining weight.

To assess the performance of the neural network model, a comparison between the predicted remaining weight and the actual values is presented in Figures 73-75. These figures provide a visual representation of the alignment between the predicted values from the model and the corresponding actual values.

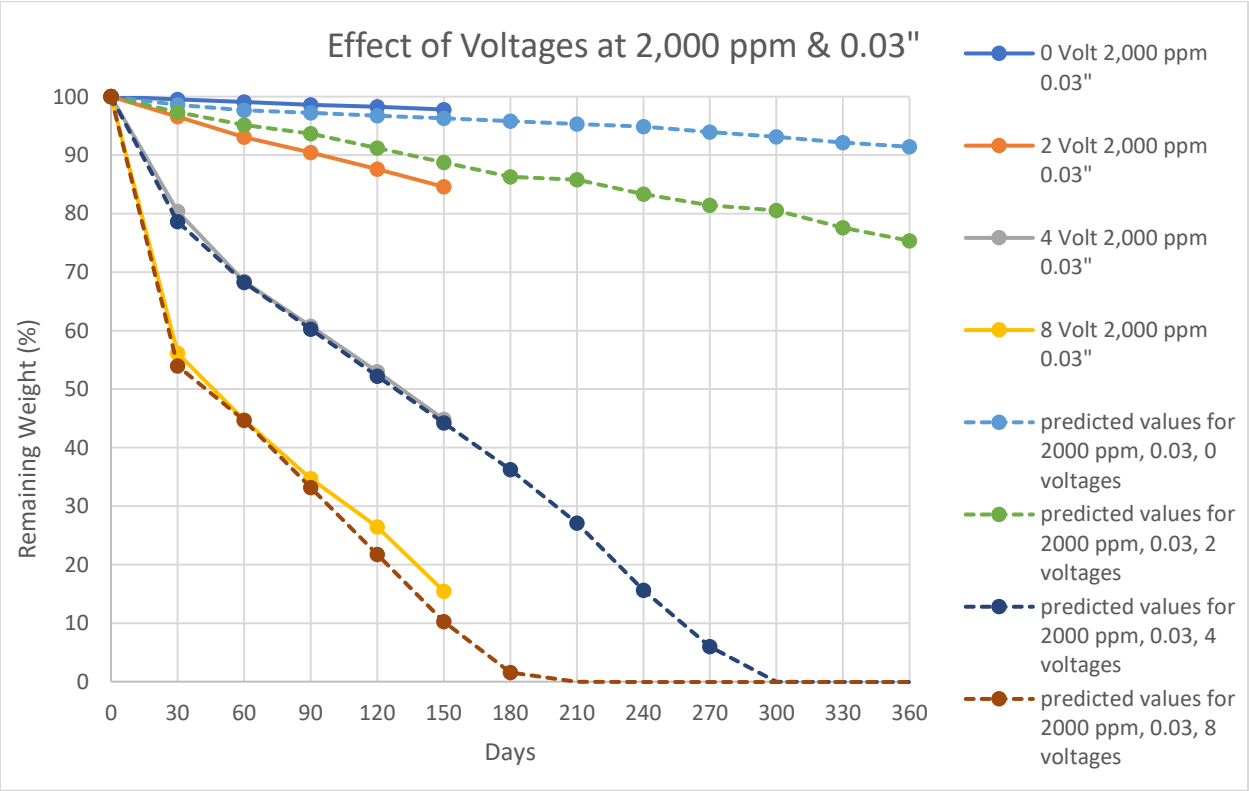

Figure 73. Effect of Voltages in Predicted and Actual Terms

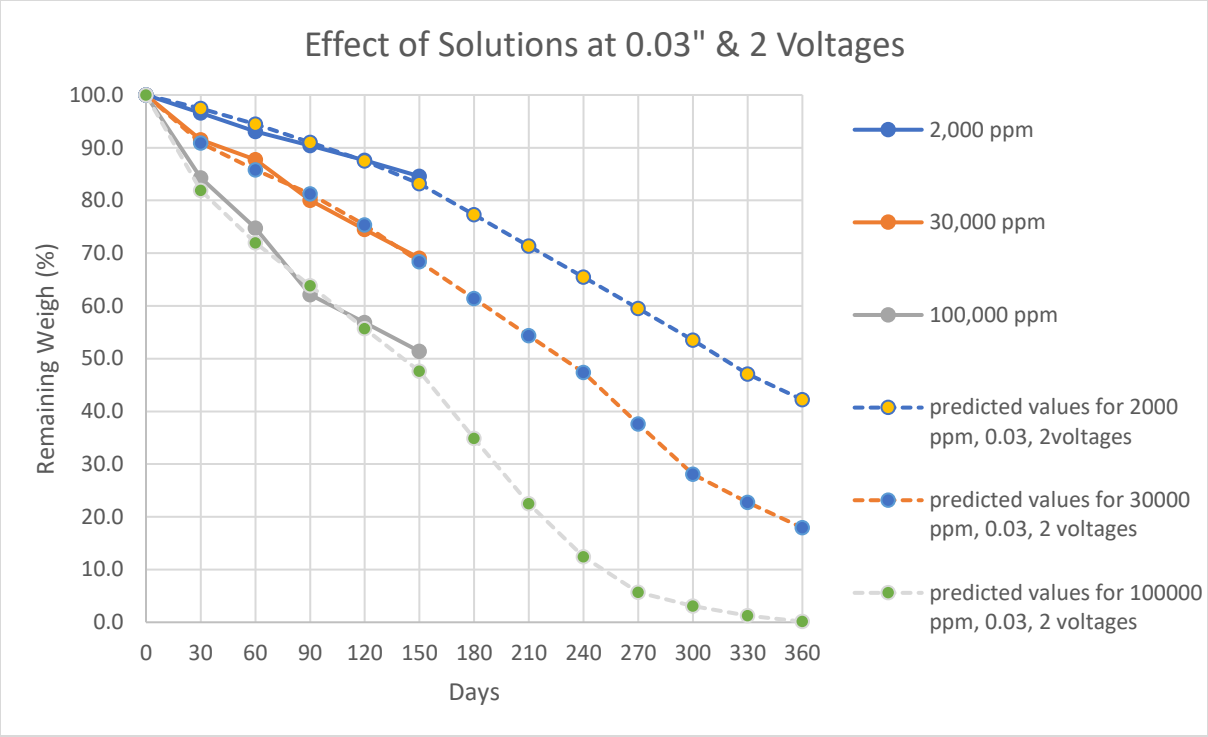

Figure 74. Effect of Solutions in Predicted and Actual Terms

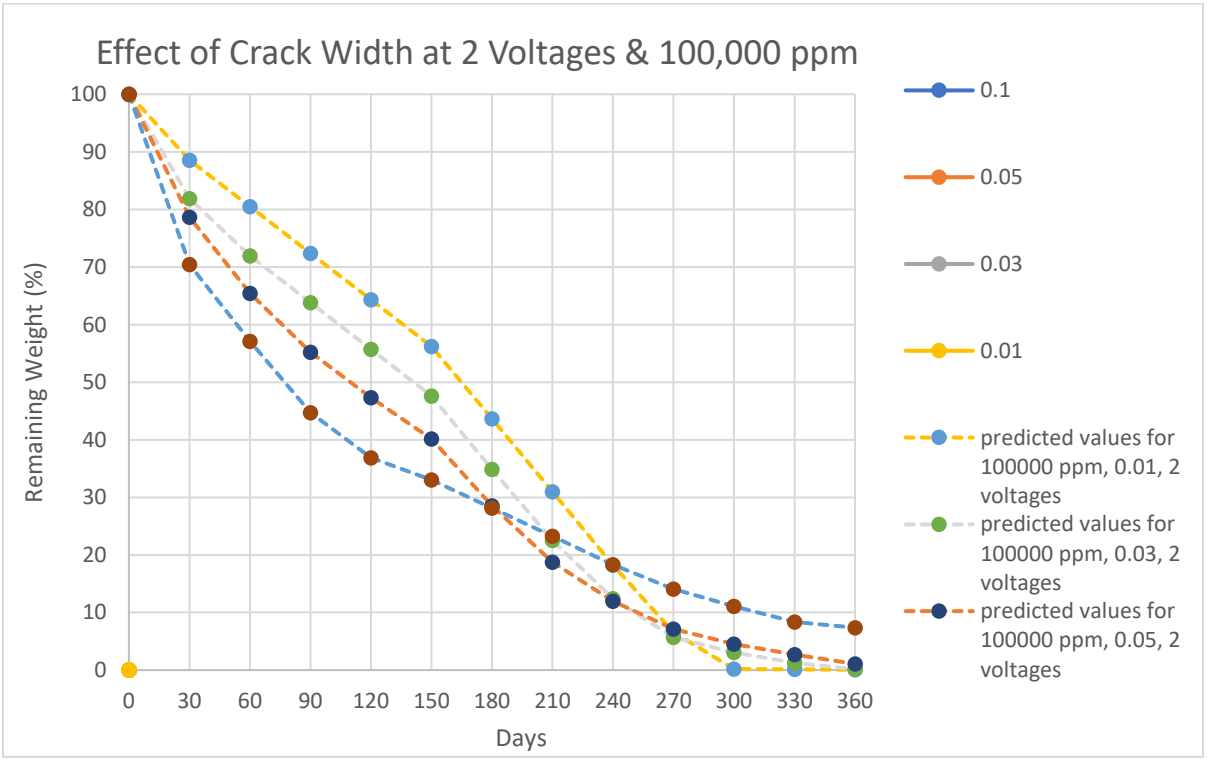

Figure 75. Effect of Crack Width in Predicted and Actual Terms

CHAPTER 7. SUMMARY AND CONCLUSION

7.1. Summary

This research conducted a comprehensive series of structural tests to investigate the effects of corrosion rate on reinforced concrete structures. The primary objective was to optimize the accelerated corrosion test method by inducing varying crack widths in concrete cylinders under different environmental conditions and applying different voltages. Specifically, the cylinders were immersed in sodium chloride solutions with concentrations of 2,000, 30,000, and 100,000 ppm and subjected to 2, 4, 8, and 0 Volts as a control. A range of mechanical and microscopic tests and analyses were performed, including electrochemical chloride reactor experiments, Profometer assessments of corrosion rate probability, measurement of remaining weight to determine corrosion rate at different stages, and scanning electron microscopy (SEM) and energy-dispersive X-ray spectroscopy (EDX) analyses to visualize corrosion spots and analyze elemental composition. Furthermore, the healing rate was evaluated for two different cement ratios, and the corrosion rate of rebars with varying sizes was investigated. This section presents the conclusions derived from immersing full-size cylinders in sodium chloride solution and applying voltages, elucidating the impact on corrosion rate and weight loss in steel specimens.

The study's first phase focused on the effects of corrosion on steel bars, where 108 samples were immersed in sodium chloride solutions of 2,000, 30,000, and 100,000 ppm, along with five different voltages, including a control group, for 14 days. Daily measurements of remaining weight and diameter were taken. The results indicate that at a chloride concentration of 2,000 ppm, rebars subjected to 12 and 16 Volts exhibited less than 50% remaining weight after a 7-day testing period. This suggests that higher voltages (12 and 16 Volts) accelerate the speed of corrosion. At 30,000

ppm, rebars subjected to 16 Volt lost their weight entirely after five days, while those subjected to 12 Volt experienced a 50% weight loss by day 7. Similarly, at 1,000,000 ppm, rebars subjected to 16 volts lost their weight within three days, and rebars subjected to 12 volts lost 50% of their weight by day 5. Increasing the voltage accelerates the corrosion process, with higher voltages (12 and 16 Volts) resulting in more significant weight loss and corrosion than lower voltages.

The study's second phase involved embedding bars in concrete cylinders and immersing them in solutions with varying concentrations for up to 6 months.

7.2. Conclusion

Based on the results obtained, the following conclusions can be drawn:

1) The Profometer readings obtained in this study align with the range specified by ASTM C876, indicating a strong correlation between the Profometer values and the observed corrosion levels. This supports the validity and reliability of the ASTM C876 standard for assessing corrosion in reinforced concrete structures. In this project, the corrosion threshold of 50% corresponded to a Profometer reading of -280 mV.

2) The investigation of the effect of voltages on corrosion levels in samples with 2,000 ppm concentration and 0.01" crack width revealed notable findings. As the voltages increased from 0 to 2, 4, and 8 Volt, the corrosion amount for the 0.01" crack width increased from 1.8% to 12.3%, 49.4%, and 88.7%, respectively. This indicates a significant correlation between voltage increment and increased corrosion, with the corrosion amount being 6.8 times higher than the control sample for 2 Volt. Moreover, the corrosion amounts for 4 and 8 Volts were 27.4 and 49.2 times higher, respectively, compared to the control sample.

For samples with a crack width of 0.03" and 2,000 ppm concentration, the corrosion amount reached 36 times higher than the control sample with 8 Volt. The samples with 8 Volt and crack widths of 0.05" and 0.1" exhibited complete corrosion. For the 2,000-ppm concentration, increasing the voltages to 2, 4, and 8 Volts resulted in average corrosion rates of 6.70, 22.8, and 32.2 times higher than the control sample, respectively. Similarly, at 30,000 ppm concentration, the average corrosion rates for 2, 4, and 8 Volts were 9.4, 22, and 24 times higher than the zero voltage samples. Additionally, for samples immersed in 100,000 ppm solutions, the corrosion rates for 2, 4, and 8 Volts were 6.7 and 11 times higher, respectively.

Higher voltages significantly impact the corrosion rates of the concrete cylinders. Increasing the voltage accelerates the corrosion process, leading to more weight loss in the cylinders. Cylinders subjected to higher voltages, particularly 4 and 8 Volts, exhibited more significant weight loss than those subjected to lower voltages of 0 and 2 Volts.

Statistical analysis using post-hoc tests revealed significant differences in the remaining weight of the cylinders between the different voltage levels. Specifically, there were significant differences between the 0-Volt and 4-Volt conditions and between the 0-Volt and 8-Volt conditions. These findings suggest that higher voltages, such as 4 and 8 Volts, have a more detrimental effect on the remaining weight of the cylinders. However, no significant difference was observed between the 2-Volt and 0-Volt conditions, indicating that a voltage level of 2 Volt had a similar impact on weight loss as no voltage was applied.

3) The effect of crack width on corrosion levels was examined while keeping the voltages and solutions constant at 0 voltage and 2,000 ppm concentration. It was observed that as the crack width increased from 0.01" to 0.03", 0.05", and 0.1", the average corrosion amounts were found to be 1.4, 2.4, and 3 times higher, respectively, compared to the 0.01" crack width. This average rate remained relatively consistent for two voltages. However, for 4 and 8 voltages, the corrosion rates were deemed unacceptable as a significant portion of the rebars corroded before the six-month mark.

   Based on the results obtained regarding the crack width, it can be concluded that an increase in crack width leads to an acceleration in the rate of weight loss in the rebars, indicating a higher corrosion rate. This finding suggests that wider cracks provide enhanced pathways for corrosive agents to penetrate the concrete and reach the embedded rebars, resulting in more significant corrosion damage. Specifically, among these crack widths, the 0.1-inch crack width exhibited a significant decrease in remaining weight over time, indicating a higher corrosion rate than the other. The crack width of 0.05 inches also demonstrated a noticeable decrease in remaining weight, suggesting a relatively high corrosion rate. Similarly, the crack width of 0.03 inches showed a decrease in remaining weight, indicating a moderate corrosion rate. On the other hand, the crack width of 0.01 inches displayed a smaller decrease in remaining weight, suggesting a lower corrosion rate compared to the other crack widths. Therefore, it can be concluded that the crack size of 0.1 and 0.05 inches significantly affects the remaining weight.

   The HSD (Honestly Significant Difference) test results support this conclusion by indicating that the remaining weight for the 0.1-inch and 0.05 inches crack size significantly differs from the remaining weights of all other crack sizes (0.03 inches and

0.01 inches). In contrast, the remaining weights of the other crack sizes may exhibit significant differences but not from the remaining weight of the 0.1 and 0.05 inches crack size.

4) Additionally, the impact of solution concentration on corrosion levels was investigated at zero voltage for all crack widths. By increasing the concentration to 30,000 and 100,000 ppm, the average corrosion amounts increased by 1.7 and 3.4 times, respectively, compared to the 2,000 ppm concentration. Similarly, when the solution concentration increased to 30,000 and 100,000 ppm, the average corrosion amounts for 2 Volt and various crack widths were 1.4 and 2.5 times higher than the 2,000 ppm concentration. However, this trend did not hold for 4 and 8 voltages. The concentration of sodium chloride directly influences the corrosion rate, with higher salt concentrations leading to more aggressive corrosion. In contrast, lower concentrations result in a relatively slower corrosion process. The Tukey HSD test on the solution concentrations demonstrates statistically significant differences in remaining weight between all solution concentrations, indicating significant disparities.
5) The results obtained from scanning electron microscopy (SEM) and energy-dispersive X-ray spectroscopy (EDX) analyses provide valuable insights. Increasing the crack size is visually correlated with increased rust spots observed through SEM. Additionally, raising the concentration of the solution leads to an increase in oxygen content. A higher oxygen content signifies a more significant proportion of elements in higher oxidation states, indicating a higher oxidation level. Since oxygen is necessary for corrosion, higher oxygen levels create a more favorable environment for oxidation reactions.

6) Based on the statistical analysis, the results indicate that the crack width variable has a more significant effect on the corrosion rate than other variables. Increasing crack width accelerates corrosion, leading to a higher corrosion rate. This suggests that wider cracks provide enhanced pathways for corrosive agents to penetrate the concrete and access the embedded rebars, resulting in more significant corrosion damage.

7) Regarding rebar size, when the rebar size is increased from 0.194" to 0.226", representing a 16% increase, the corrosion rate of the larger rebar is 11% lower compared to the corrosion rate of the smaller size. The results demonstrate that larger-sized rebars experience comparatively lower levels of corrosion. Under identical time and environmental conditions, larger-sized rebars exhibit an 11% reduction in corrosion compared to smaller-sized rebars. This suggests that the size of the rebar plays a role in influencing the corrosion resistance of the reinforced concrete structures.

8) The findings from the autogenous healing tests indicate that the cement ratio impacts the healing speed. At a crack width of 0.01", the amount of crack healing for a high cement ratio is found to be 4.8% higher than the healing observed in a low cement ratio. Moreover, for crack widths of 0.03" and 0.05", the healing percentage for the high cement ratio is respectively 2.2% and 1.06% higher than the healing percentage for the lower cement ratio. So, A higher cement ratio corresponds to a higher healing speed. The results also reveal that the healing process is more effective and faster for lower crack widths (0.01 inches) than wider cracks. This implies that more minor cracks have a higher potential for self-healing, contributing to the mitigation of corrosion damage.

Therefore, the critical parameters for this study are higher voltage (4 and 8) and higher concentration solutions (30,000 and 100,000 ppm). These factors significantly impact the corrosion rate and remaining weight of the reinforced concrete structures under investigation.

7.3. Recommendation of Future Work

Several avenues for future research are recommended to enhance the comprehensiveness and applicability of the current study. Extending the experimental timeline beyond six months can provide insights into long-term corrosion behavior. Additional environmental factors like temperature and humidity can contribute to a more realistic understanding of corrosion processes. Advanced monitoring techniques such as electrochemical impedance spectroscopy and numerical simulations can deepen the analysis. Secondly, field validation of the optimized parameters in real-world settings and exploring the effects of dynamic loads would offer practical insights. Additionally, conducting life-cycle and economic assessments can provide a holistic perspective on the sustainability and feasibility of the proposed corrosion mitigation strategy. In conclusion, by delving into these suggested areas, the study can further enrich its findings and their practical implications for improving reinforced concrete structures' durability and service life.

References

1. ACI 318. Building Code Requirements for Structural Concrete.
2. ASTM A706. Standard Specification for Low-Alloy Steel Deformed and Plain Bars for Concrete Reinforcement.
3. ASTM C1840-23 - Standard Practice for Inspection and Acceptance of Installed Reinforced Concrete Culvert, Storm Drain, and Storm Sewer Pipe.
4. ASTM C876/C876M-19 - Standard Test Method for Corrosion Potentials of Uncoated Reinforcing Steel in Concrete.
5. ASTM G48 - Standard Test Methods for Pitting and Crevice Corrosion Resistance of Stainless Steels and Related Alloys by Use of Ferric Chloride Solution.
6. Half-Cell Potential Test: Measurement and Devices (giatecscientific.com)
7. Webinar: Post-Installation Inspection of Storm Sewer Pipes and Culverts (concretepipe.org)
8. Alavi, M., Atrens, A., & Dietzel, W. (2007). Corrosion behavior of magnesium alloys in chloride environments. Materials Science and Engineering: A, 464(1-2), 277-289.
9. Al-Lami, B. (2020). Performance of Cracked Reinforced Concrete Pipes Subjected to Different Environmental Conditions. Ph.D. Dissertation, University of Texas at Arlington.
10. Angst, U., Larsen, C. K., Vennesland, O., & Elsener, B. (2010). Influence of casting direction on chloride-induced rebar corrosion. In Concrete under Severe Conditions: Environment and Loading-Proceedings of the 6th International Conference on Concrete under Severe Conditions, CONSEC'10.

11. Bard, A. J., & Faulkner, L. R. (2000). Electrochemical Methods: Fundamentals and Applications (2nd ed.). Wiley.
12. Baweja, D., Roper, H., & Sirivivatnanon, V. (1998). Chloride-induced steel corrosion in concrete: Part 1 - Corrosion rates, corrosion activity, and attack areas. ACI Materials Journal, 95(3), 329–335.
13. Bhandari, P. K., Segupta, A., & Kanawada, B. D. (2016). Advanced NDT methods for evaluation of bridges. International Journal of Advanced Research in Science and Engineering, 5(9), 2319-8354
14. Böhni, H. (2004). Corrosion of Steel in Concrete: Prevention, Diagnosis, Repair. Wiley.
15. Busba, E., & Sagüés, A. A. (2013). Localized Corrosion of Embedded Steel in Cracked Reinforced Concrete Pipe. 403-416.
16. Cao, H., Wang, H., Zheng, L., Li, X., Zhou, Y., & Zhang, L. (2019). Experimental Study on the Effect of Rebar Size on Reinforced Concrete Corrosion. Journal of Materials in Civil Engineering, 31(1), 04018381.
17. Chen, Y., Wang, X., Li, Z., & Zhang, Q. (2018). Influence of Sodium Chloride on the Corrosion Rate of Reinforced Steel in a Coastal Environment. Journal of Corrosion Science and Engineering, 15(2), 78-92.
18. Chen, Z., Liu, J., Qian, C., Wang, Q., Yang, Z., & Wang, X. (2017). Investigation on the Corrosion Characteristics of Reinforcing Steel in Chloride-Rich Environment Using SEM/EDX Analysis. Journal of Materials Science and Chemical Engineering, 5(6), 7-14.
19. Chung, D. D. L. (2012). Corrosion Control of Steel-Reinforced Concrete. Materials Engineering and Performance.

20. De Rooij, M. R., Schlangen, E., & Breugel, K. V. (2018). Autogenous Healing of Cracks in Concrete with Varying Cement Ratios. Cement and Concrete Research, 105, 127-138.
21. Garcia, A., Martinez, L., & Lopez, D. (2018). Influence of Sodium Chloride on the Corrosion Rate of Reinforced Steel in Chloride-Rich Environments. Corrosion Engineering Journal, 32(3), 150-165.
22. Gaynor, N. G. (1982). Corrosion of Steel in Concrete. Materials Performance, 21(4), 18-23.
23. Goldstein, J. I., Newbury, D. E., Joy, D. C., Lyman, C. E., Echlin, P., Lifshin, E., & Fiori, C. (2017). Scanning electron microscopy and X-ray microanalysis. Springer.
24. Gupta, A., & Singh, V. (2020). SEM, TEM, and XRD Techniques for the Analysis of Nanomaterials. In Materials Characterization Techniques (pp. 125-158). Elsevier.
25. Hearn, N. (1998). Self-sealing, autogenous healing, and continued hydration: What is the difference? Materials and Structures/Materiaux et Constructions, 31(8), 563–56
26. Kawasaki, M., Endo, T., & Maeda, H. (2018). Energy-dispersive X-ray spectroscopy for elemental analysis in transmission electron microscopy. Journal of Electron Microscopy, 67(2), 93-101.
27. Kim, S., Lee, J., Park, H., & Choi, W. (2018). Effect of Applied voltages on the Corrosion Rate of Reinforced Steel in a Simulated Corrosive Environment. Journal of Corrosion Science, 40(3), 178-190.
28. Kosmatka, S. H., Kerkhoff, B., & Panarese, W. C. (2002). Design and Control of Concrete Mixtures. Portland Cement Association.

29. Li, H., Zhang, J., Chen, X., & Wu, Y. (2019). Effect of Applied voltages on the Corrosion Rate of Reinforced Steel in a Marine Environment. Corrosion Engineering Journal, 35(4), 198-211.
30. Li, L.-Y., Xia, J., & Lin, S.-S. (2012). A multi-phase model for predicting the effective diffusion coefficient of chlorides in concrete. Construction and Building Materials, 26(1), 295–301.
31. Li, S., Wang, Z., Zhang, J., Wang, J., & Zhang, H. (2020). Effect of Crack Width on the Corrosion Rate of Reinforced Steel in Chloride-Rich Concrete Structures. Construction and Building Materials, 256, 119382.
32. Li, W., Liu, X., & Zhang, M. (2016). Influence of Rebar Size on Corrosion Rate and Corrosion Products in Reinforced Concrete Structures. Journal of Materials in Civil Engineering, 28(11), 04016109.
33. Li, W., Liu, W., & Wang, S. (2017). The Effect of Crack Width on Chloride-Induced Corrosion of Steel in Concrete. Research Article | Open Access, Article ID 3968578.
34. Maes, M., Snoeck, D., & De Belie, N. (2016). Chloride penetration in the cracked mortar and the influence of autogenous crack healing. Construction and Building Materials, 115, 114–124.
35. Martın-Pereza, B., Zibarab, H., Hootonb, R. D., & Thomas, M. D. A. (2000). A study of the effect of chloride binding on service life predictions. Cement and Concrete Research, 30(8), 1215–1223.
36. Mehta, P. K., & Monteiro, P. J. M. (2014). Concrete: Microstructure, Properties, and Materials. McGraw-Hill Education.
37. Mindess, S., Young, J. F., & Darwin, D. (2006). Corrosion of Steel in Concrete. CRC Press.

38. Neave, H. R. (1995). Statistical Tables for the Social, Biological, and Physical Sciences. CRC Press.

39. Neville, A. M., & Brooks, J. J. (2010). Concrete technology. Pearson Education.

40. Otieno, M., Beushausen, H., & Alexander, M. (2016). Chloride-induced steel corrosion in cracked concrete - Part II: Corrosion rate prediction models. Cement and Concrete Research, 79, 386–394.

41. Pacheco-Torgal, F., Ding, Y., Colangelo, F., & Tuladhar, R. (2019). Effect of Cement Ratio on the Autogenous Healing of Self-Healing Concrete. Construction and Building Materials, 211, 448-458.

42. Palin, D., Wiktor, V., & Jonkers, H. M. (2015). Autogenous healing of marine exposed concrete: Characterization and quantification through visual crack closure. Cement and Concrete Research, 73, 17–24.

43. Poursaee, A., & Hansson, C. M. (2010). Electrochemical Techniques for Corrosion Monitoring. Woodhead Publishing.

44. Presuel-Moreno, F., Balasubramanian, H., & Wu, Y.-Y. (2013). Corrosion of Reinforced Concrete Pipes: An Accelerated Approach. NACE - International Corrosion Conference Series, PP. 2551.

45. Ragab, A. M., Elgammal, M. A., Hodhod, O. A. G., & Ahmed, T. E. S. (2016). Evaluation of field concrete deterioration under real conditions of seawater attack. Construction and Building Materials, 119, 130–144.

46. Rossi, E., Polder, R., Copuroglu, O., Nijland, T., & Šavija, B. (2020). The influence of defects at the steel/concrete interface for chloride-induced pitting corrosion of naturally

deteriorated 20-year-old specimens was studied through X-ray Computed Tomography. Construction and Building Materials, 235, 117474.

47. Shao, W., & Li, J. (2014). Service life prediction of cracked RC pipe piles exposed to marine environments. Construction and Building Materials, 64, 301–307.
48. Silva, F. S., Nunes, S. P., Barros, J. A. O., & Correia, J. R. (2020). Autogenous Healing of Cracks in Concrete: Effect of High and Low Cement Ratios. Materials and Structures, 53(5), 125.
49. Song, G., & Atrens, A. (1999). Corrosion mechanisms of magnesium alloys. Advanced Engineering Materials, 1(1), 11-33.
50. Song, H. W., Kwon, S. J., Kim, J. K., & Yi, N. H. (2018). Effect of Rebar Size on Corrosion Rate in Reinforced Concrete Structures. Journal of Materials in Civil Engineering, 30(3), 04018008.
51. Soutsos, M., Tang, L., Millard, S. G., & Bungey, J. H. (2016). Concrete Durability: Cementitious Materials and Reinforced Concrete Properties, Behavior, and Corrosion Resistance. CRC Press.
52. Smith, J., Johnson, A., & Thompson, R. (2019). Influence of Sodium Chloride on the Corrosion Rate of Reinforced Steel in Marine Environments. Journal of Corrosion Science, 45(2), 127-140.
53. Tang, Y., Li, S., Gao, F., Wu, S., & Yu, L. (2020). Investigation of Corrosion Products on Reinforcement Using SEM and EDX. Construction and Building Materials, 259, 119739.
54. Tuutti, K. (1982). Corrosion of Steel in Concrete. Swedish Cement and Concrete Research Institute.

55. Wang, J., Li, X., Zhang, Q., & Chen, Y. (2019). Effect of Crack Size on the Corrosion Rate of Reinforced Steel in a Marine Environment. Journal of Materials Science, 54(17), 11643-11654.
56. Wang, J., Li, Z., Wang, Z., & Huang, X. (2017). Effect of Cement Ratio on Autogenous Healing of Concrete. Construction and Building Materials, 149, 182-190.
57. Yang, S., Zhang, X., Li, W., & Liu, Y. (2020). Effect of Applied Voltages on the Corrosion Rate of Reinforced Steel in a Chloride-Contaminated Environment. Journal of Corrosion Science and Engineering, 25(2), 56-69.
58. Zhang, H., Liu, Y., Wang, G., & Li, Z. (2017). Effect of Crack Width on the Corrosion Rate of Reinforced Steel in Concrete Structures. Construction and Building Materials, 156, 231-241.
59. Zhang, Y., Li, Q., Wang, M., & Yuan, G. (2019). Investigation on Corrosion Mechanism of Reinforcement in Concrete by SEM and EDX. Journal of Materials Science and Chemical Engineering, 7(11), 28-35.

Appendix I: Numerical Results Obtained from Profometer & Remaining Weight

Table 31. Results for 2,000 ppm and 0.01" Crack Width at Different Voltages.

		Days	0.0	30.0	60.0	90.0	120.0	150.0	180.0
2,000 ppm & 0.01"	*0 V*	*Profometer (mV)*	*-120.0*	*-121.8*	*-124.0*	*-127.2*	*-129.6*	*-133.2*	*-135.6*
		Remaining Weight (%)	*100.0*	*99.7*	*99.4*	*99.2*	*98.9*	*98.5*	*98.2*
	2 V	*Profometer (mV)*	*-120.0*	*-138.2*	*-153.0*	*-172.4*	*-189.2*	*-202.6*	*-205.4*
		Remaining Weight (%)	*100.0*	*97.5*	*95.8*	*93.5*	*91.5*	*89.4*	*87.7*
	4 V	*Profometer (mV)*	*-120.0*	*-204.3*	*-225.2*	*-240.3*	*-251.9*	*-262.2*	*-274.1*
		Remaining Weight (%)	*100.0*	*87.0*	*76.9*	*69.4*	*63.8*	*57.4*	*50.6*
	8 V	*Profometer (mV)*	*-120.0*	*-241.6*	*-259.1*	*-281.1*	*-301.3*	*-321.8*	*-349.8*
		Remaining Weight (%)	*100.0*	*66.6*	*57.5*	*47.1*	*36.6*	*26.3*	*11.3*

Table 32. Results for 2,000 ppm and 0.03" Crack Width at Different Voltages.

		Days	0	30	60	90	120	150	180
2,000 ppm & 0.03"	*0 V*	*Profometer (mV)*	*-120.0*	*-123.3*	*-126.4*	*-132.8*	*-134.9*	*-136.1*	*-139.5*
		Remaining Weight (%)	*100*	*99.5*	*99.1*	*98.6*	*98.3*	*97.8*	*97.4*
	2 V	*Profometer (mV)*	*-120*	*-144.2*	*-174.8*	*-197.8*	*-206.2*	*-211.3*	*-216.2*
		Remaining Weight (%)	*100*	*96.6*	*93.1*	*90.4*	*87.6*	*84.6*	*81.9*
	4 V	*Profometer (mV)*	*-120*	*-217.1*	*-241.1*	*-256.2*	*-267.2*	*-286.1*	*-299.1*
		Remaining Weight (%)	*100*	*80.4*	*68.4*	*60.7*	*53.0*	*44.8*	*36.6*
	8 V	*Profometer (mV)*	*-120*	*-262.9*	*-286.8*	*-30.1*	*-321.2*	*-341.2*	*-590.1*
		Remaining Weight (%)	*100*	*56.2*	*44.7*	*34.7*	*26.4*	*15.5*	*4.1*

Table 33. Results for 2,000 ppm and 0.05" Crack Width at Different Voltages.

		Days	0	30	60	90	120	150	180
2,000 ppm & 0.05"	*0 V*	*Profometer (mV)*	*-120.0*	*-125.2*	*-130.4*	*-137.6*	*-143.1*	*-147.2*	*-152.7*
		Remaining Weight (%)	*100*	*99.2*	*98.6*	*97.9*	*97.3*	*96.5*	*95.8*
	2 V	*Profometer (mV)*	*-120*	*-164.2*	*-201.9*	*-209.5*	*-217.1*	*-222.1*	*-233.8*
		Remaining Weight (%)	*100*	*94.7*	*89.4*	*85.5*	*81.8*	*77.0*	*72.6*
	4 V	*Profometer (mV)*	*-120*	*-228.9*	*-259.3*	*-278.9*	*-295.1*	*-307.2*	*-323.1*
		Remaining Weight (%)	*100*	*73.8*	*57.6*	*48.8*	*40.0*	*31.6*	*23.3*
	8 V	*Profometer (mV)*	*-120*	*-282.1*	*-314.2*	*-339.8*	*-600.0*	*-600.0*	*-600.0*
		Remaining Weight (%)	*100*	*45.7*	*29.3*	*16.6*	*0.0*	*0.0*	*0.0*

Table 34. Results for 2,000 ppm and 0.1" Crack Width at Different Voltages.

			0	30	60	90	120	150	180
2,000 ppm & 0.1"	*0 V*	*Profometer (mV)*	*-120*	*-128.4*	*-137.1*	*-146.1*	*-150.2*	*-156.1*	*-163.9*
		Remaining Weight (%)	*100*	*98.8*	*97.9*	*97.0*	*96.3*	*95.4*	*94.7*
	2 V	*Profometer (mV)*	*-120*	*-182.1*	*-214.5*	*-222.8*	*-227.9*	*-236.7*	*-247.6*
		Remaining Weight (%)	*100*	*92.0*	*83.1*	*79.2*	*75.3*	*70.5*	*65.6*
	4 V	*Profometer (mV)*	*-120*	*-247.1*	*-278.2*	*-297.1*	*-315.1*	*-330.2*	*-350.4*
		Remaining Weight (%)	*100*	*65.5*	*49.4*	*39.1*	*28.1*	*19.3*	*11.6*
	8 V	*Profometer (mV)*	*-120*	*-304.6*	*-341.1*	*-553.0*	*-600.0*	*-600.0*	*-600.0*
		Remaining Weight (%)	*100*	*33.6*	*15.4*	*5.0*	*0.0*	*0.0*	*0.0*

Table 35. Results for 30,000 ppm and 0.01" Crack Width at Different Voltages.

			0	30	60	90	120	150	180
30,000 ppm & 0.01"	*0 V*	*Profometer (mV)*	*-120*	*-124.3*	*-126.5*	*-133.1*	*-135.1*	*-141.2*	*-143.1*
		Remaining Weight (%)	*100*	*99.5*	*99.1*	*98.5*	*97.9*	*97.4*	*97.0*
	2 V	*Profometer (mV)*	*-120*	*-155.3*	*-196.1*	*-205.2*	*-218.1*	*-227.2*	*-235.5*
		Remaining Weight (%)	*100*	*95.4*	*90.7*	*87.4*	*81.1*	*75.1*	*70.5*
	4 V	*Profometer (mV)*	*-120*	*-229.3*	*-249.1*	*-263.3*	*-282.1*	*-310.1*	*-329.1*
		Remaining Weight (%)	*100*	*73.7*	*64.1*	*55.7*	*44.8*	*32.1*	*19.9*
	8 V	*Profometer (mV)*	*-120*	*-275.1*	*-293.9*	*-320.1*	*-350.2*	*-600.0*	*-600.0*
		Remaining Weight (%)	*100*	*48.9*	*38.7*	*27.0*	*11.6*	*0.0*	*0.0*

Table 36. Results for 30,000 ppm and 0.03" Crack Width at Different Voltages.

			0	30	60	90	120	150	180
30,000 ppm & 0.03"	*0 V*	*Profometer (mV)*	*-120*	*-125.5*	*-129.7*	*-136.1*	*-140.4*	*-145.3*	*-150.2*
		Remaining Weight (%)	*100*	*99.3*	*98.7*	*98.1*	*97.3*	*96.7*	*96.3*
	2 V	*Profometer (mV)*	*-120*	*-186.9*	*-205.7*	*-220.9*	*-231.9*	*-241.4*	*-249.4*
		Remaining Weight (%)	*100*	*91.5*	*87.7*	*80.0*	*74.5*	*69.1*	*64.0*
	4 V	*Profometer (mV)*	*-120*	*-240.6*	*-261.1*	*-269.2*	*-300.3*	*-326.2*	*-353.2*
		Remaining Weight (%)	*100*	*67.2*	*56.7*	*48.6*	*37.6*	*21.8*	*9.4*
	8 V	*Profometer (mV)*	*-120*	*-313.4*	*-324.2*	*-349.3*	*-582.1*	*-600.0*	*-600.0*
		Remaining Weight (%)	*100*	*30.4*	*23.9*	*11.6*	*5.6*	*0.0*	*0.0*

Table 37. Results for 30,000 ppm and 0.05" Crack Width at Different Voltages.

			0	30	60	90	120	150	180
30,000 ppm & 0.05"	*0 V*	*Profometer (mV)*	*-120*	*-128.2*	*-132.9*	*-142.8*	*-147.5*	*-153.3*	*-156.3*
		Remaining Weight (%)	*100*	*99.0*	*98.2*	*97.2*	*96.5*	*95.9*	*95.4*
	2 V	*Profometer (mV)*	*-120*	*-206.1*	*-215.6*	*-231.1*	*-243.1*	*-254.2*	*-261.2*
		Remaining Weight (%)	*100*	*86.4*	*81.6*	*74.4*	*66.7*	*62.1*	*57.7*
	4 V	*Profometer (mV)*	*-120*	*40.9*	*-280.9*	*-303.1*	*-324.0*	*-347.2*	*-600.0*
		Remaining Weight (%)	*100*	*59.1*	*48.0*	*35.7*	*24.8*	*11.8*	*0.0*
	8 V	*Profometer (mV)*	*-120*	*80.1*	*-342.5*	*-542.1*	*-600.0*	*-600.0*	*-600.0*
		Remaining Weight (%)	*100*	*19.9*	*14.3*	*4.4*	*0.0*	*0.0*	*0.0*

Table 38. Results for 30,000 ppm and 0.1" Crack Width at Different Voltages.

			0	30	60	90	120	150	180
30,000 ppm & 0.1"	*0 V*	*Profometer (mV)*	*-120*	*-131.1*	*-143.1*	*-153.9*	*-161.3*	*-168.3*	*-172.1*
		Remaining Weight (%)	*100*	*98.4*	*97.0*	*96.0*	*95.0*	*94.2*	*93.6*
	2 V	*Profometer (mV)*	*-120*	*-219.3*	*-237.4*	*-250.1*	*-259.3*	*-276.8*	*-292.4*
		Remaining Weight (%)	*100*	*78.3*	*70.8*	*63.9*	*58.6*	*50.1*	*41.9*
	4 V	*Profometer (mV)*	*-120*	*-275.1*	*-304.1*	*-321.1*	*-346.3*	*-600.0*	*-600.0*
		Remaining Weight (%)	*100*	*48.6*	*35.1*	*26.5*	*12.8*	*0.0*	*0.0*
	8 V	*Profometer (mV)*	*-120*	*-342.1*	*-404.8*	*-592.1*	*-600.0*	*-600.0*	*-600.0*
		Remaining Weight (%)	*100*	*13.4*	*7.7*	*1.1*	*0.0*	*0.0*	*0.0*

Table 39. Results for 100,000 ppm and 0.01" Crack Width at Different Voltages.

			0	30	60	90	120	150	180
100,000 ppm & 0.01"	*0 V*	*Profometer (mV)*	*-120*	*-128.1*	*-134.2*	*-144.1*	*-155.3*	*-168.7*	*-180.2*
		Remaining Weight (%)	*100*	*99.0*	*98.1*	*97.1*	*95.7*	*94.1*	*92.6*
	2 V	*Profometer (mV)*	*-120*	*-202.2*	*-213.1*	*-238.1*	*-250.0*	*-264.6*	*-274.5*
		Remaining Weight (%)	*100*	*89.3*	*81.4*	*70.5*	*64.3*	*56.8*	*49.7*
	4 V	*Profometer (mV)*	*-120*	*-273.1*	*-295.2*	*-315.3*	*-342.8*	*-600.0*	*-600.0*
		Remaining Weight (%)	*100*	*50.4*	*39.1*	*27.5*	*15.4*	*0.0*	*0.0*
	8 V	*Profometer (mV)*	*-120*	*-332.3*	*-478.0*	*-600.0*	*-600.0*	*-600.0*	*-600.0*
		Remaining Weight (%)	*100*	*18.0*	*5.8*	*0.0*	*0.0*	*0.0*	*0.0*

Table 40. Results for 100,000 ppm and 0.03" Crack Width at Different Voltages.

			0	30	60	90	120	150	180
100,000 ppm & 0.03"	*0 V*	*Profometer (mV)*	*-120*	*-129.4*	*-140.4*	*-150.9*	*-166.4*	*-176.7*	*-186.4*
		Remaining Weight (%)	*100*	*98.7*	*97.5*	*96.3*	*94.3*	*93.0*	*91.8*
	2 V	*Profometer (mV)*	*-120*	*-209.1*	*-231.6*	*-250.4*	*-263.5*	*-272.2*	*-282.6*
		Remaining Weight (%)	*100*	*84.3*	*74.7*	*62.1*	*56.8*	*51.4*	*46.5*
	4 V	*Profometer (mV)*	*-120*	*-292.1*	*-313.0*	*-337.1*	*-355.1*	*-600.0*	*-600.0*
		Remaining Weight (%)	*100*	*40.2*	*30.6*	*17.6*	*10.5*	*0.0*	*0.0*
	8 V	*Profometer (mV)*	*-120*	*-341.7*	*-579.7*	*-600.0*	*-600.0*	*-600.0*	*-600.0*
		Remaining Weight (%)	*100*	*12.7*	*1.7*	*0.0*	*0.0*	*0.0*	*0.0*

Table 41. Results for 100,000 ppm and 0.05" Crack Width at Different Voltages.

			0	30	60	90	120	150	180
100,000 ppm & 0.05"	*0 V*	*Profometer (mV)*	*-120*	*-132.3*	*-145.8*	*-157.1*	*-172.1*	*-182.3*	*-196.4*
		Remaining Weight (%)	*100*	*98.3*	*96.8*	*95.5*	*93.2*	*91.9*	*90.6*
	2 V	*Profometer (mV)*	*-120*	*-224.3*	*-241.1*	*-266.3*	*-281.6*	*-294.2*	*-307.4*
		Remaining Weight (%)	*100*	*77.5*	*66.7*	*54.2*	*47.1*	*40.2*	*33.4*
	4 V	*Profometer (mV)*	*-120*	*-306.8*	*-327.1*	*-600.0*	*-600.0*	*-600.0*	*-600.0*
		Remaining Weight (%)	*100*	*33.6*	*21.1*	*0.0*	*0.0*	*0.0*	*0.0*
	8 V	*Profometer (mV)*	*-120*	*-412.9*	*-600.0*	*-600.0*	*-600.0*	*-600.0*	*-600.0*
		Remaining Weight (%)	*100*	*5.0*	*0.0*	*0.0*	*0.0*	*0.0*	*0.0*

Table 42. Results for 100,000 ppm and 0.1" Crack Width at Different Voltages.

			0	30	60	90	120	150	180
100,000 ppm & 0.1"	*0 V*	*Profometer (mV)*	*-120*	*-141.5*	*-162.3*	*-169.4*	*-179.2*	*-201.7*	*-204.8*
		Remaining Weight (%)	*100*	*97.2*	*94.9*	*93.9*	*92.7*	*90.2*	*88.9*
	2 V	*Profometer (mV)*	*-120*	*-235.4*	*-261.1*	*-287.1*	*-301.2*	*-305.3*	*-319.1*
		Remaining Weight (%)	*100*	*69.8*	*58.4*	*43.2*	*37.4*	*32.7*	*27.4*
	4 V	*Profometer (mV)*	*-120*	*-320.2*	*-345.6*	*-600.0*	*-600.0*	*-600.0*	*-600.0*
		Remaining Weight (%)	*100*	*26.4*	*10.1*	*0.0*	*0.0*	*0.0*	*0.0*
	8 V	*Profometer (mV)*	*-120*	*-455.5*	*-600.0*	*-600.0*	*-600.0*	*-600.0*	*-600.0*
		Remaining Weight (%)	*100*	*2.2*	*0.0*	*0.0*	*0.0*	*0.0*	*0.0*

Appendix II: Graphical Results from the Remaining Weight

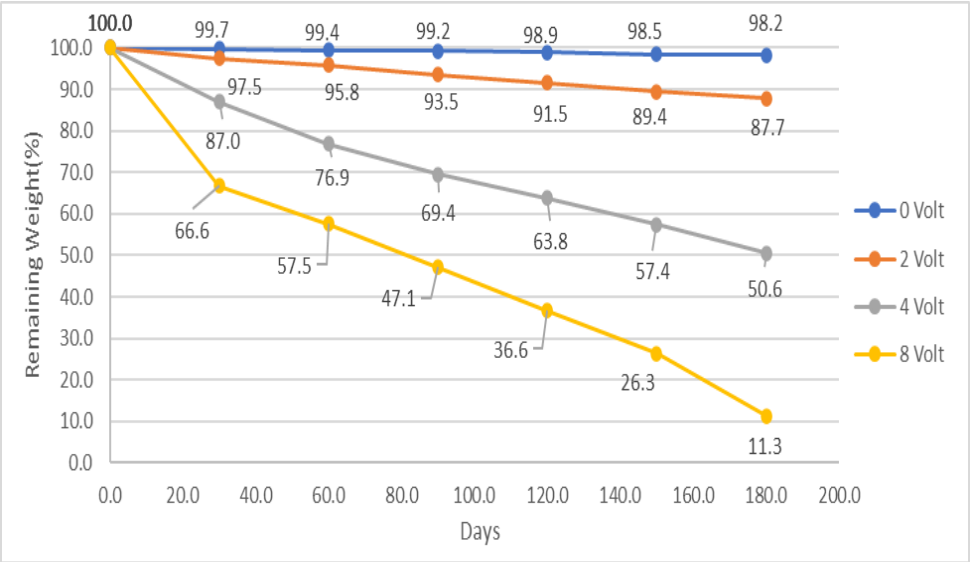

Figure 76. Effect of Voltages at 2,000 ppm and 0.01" Crack Width.

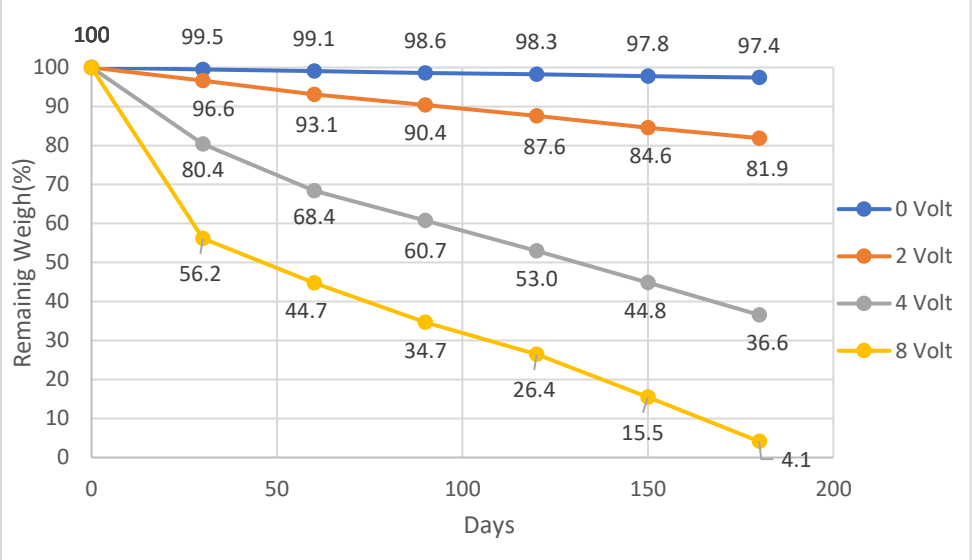

Figure 77. Effect of Voltages at 2,000 ppm and 0.03" Crack Width.

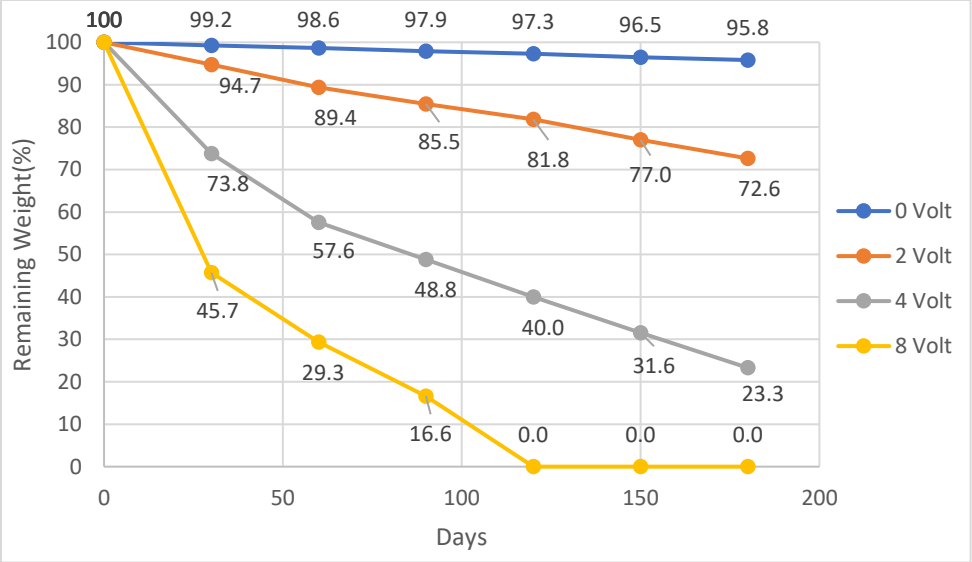

Figure 78. Effect of Voltages at 2,000 ppm and 0.05" Crack Width.

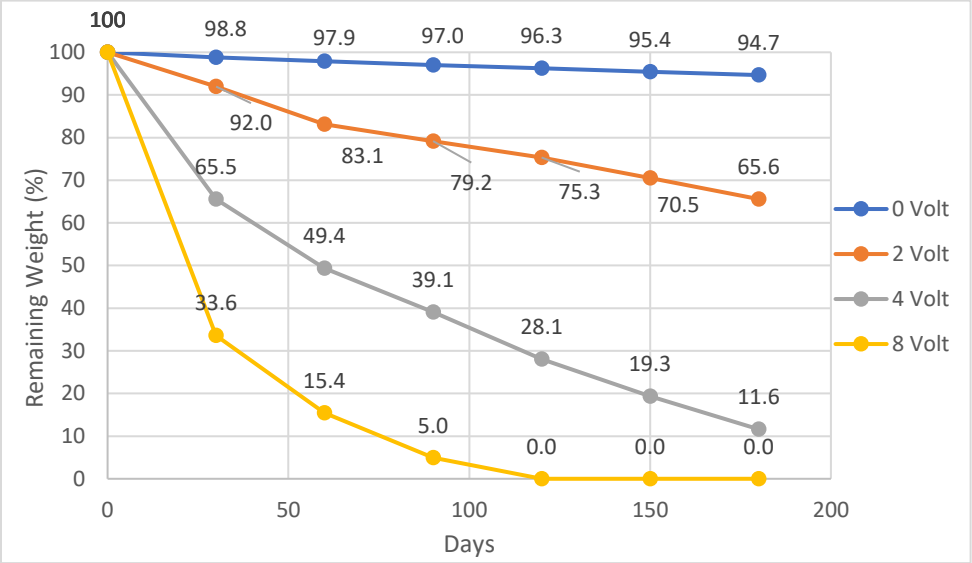

Figure 79. Effect of Voltages at 2,000 ppm and 0.1" Crack Width.

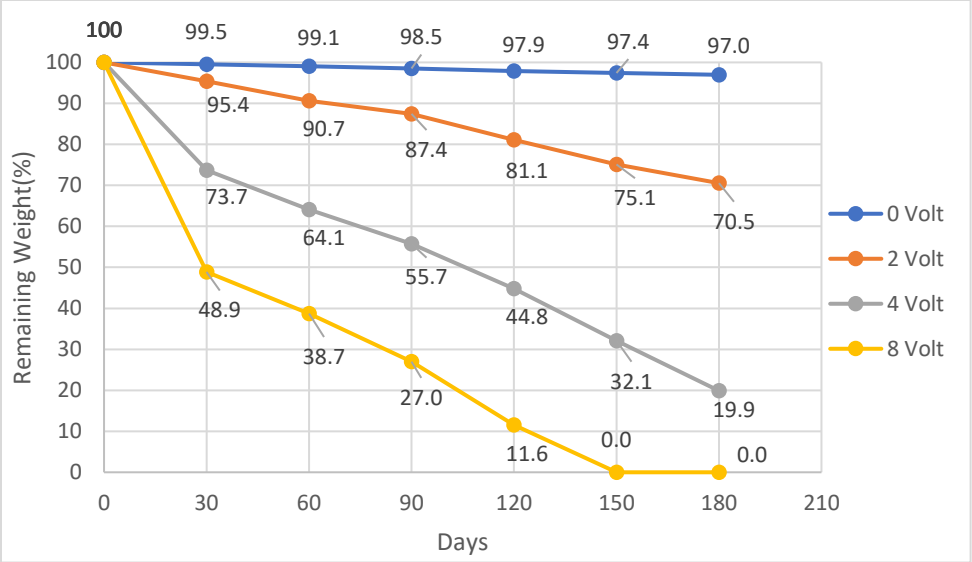

Figure 80. Effect of Voltages at 30,000 ppm and 0.01" Crack Width.

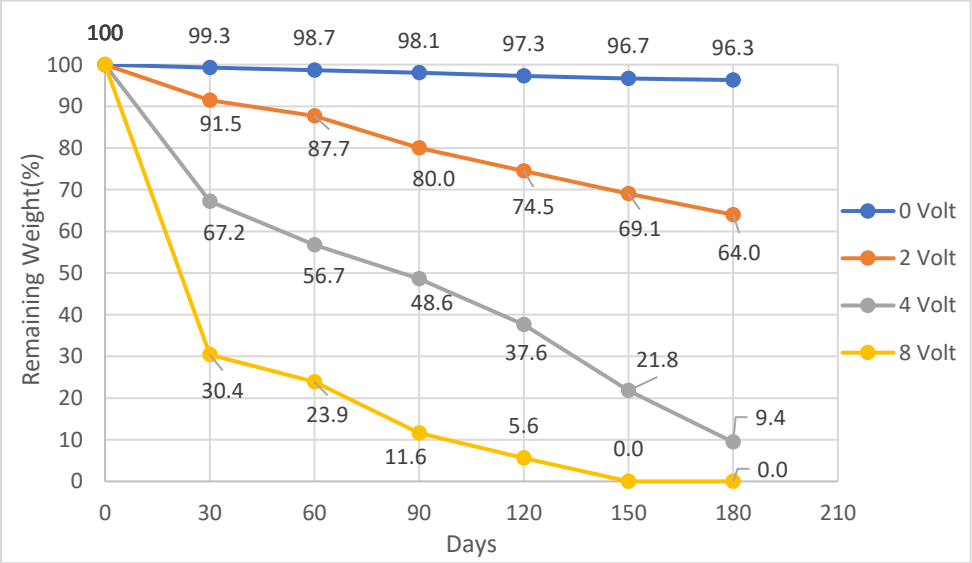

Figure 81. Effect of Voltages at 30,000 ppm and 0.03" Crack Width.

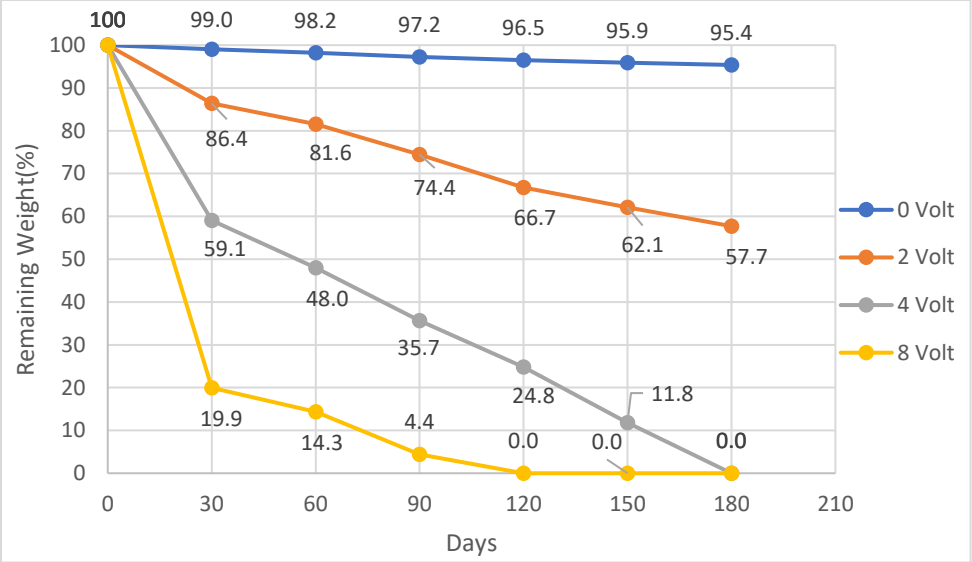

Figure 82. Effect of Voltages at 30,000 ppm and 0.05" Crack Width.

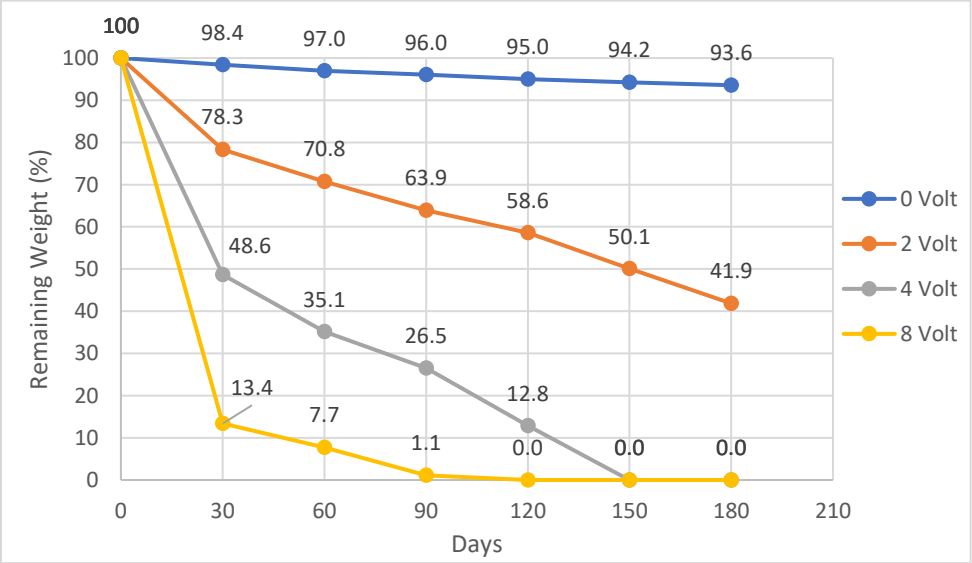

Figure 83. Effect of Voltages at 30,000 ppm and 0.1" Crack Width.

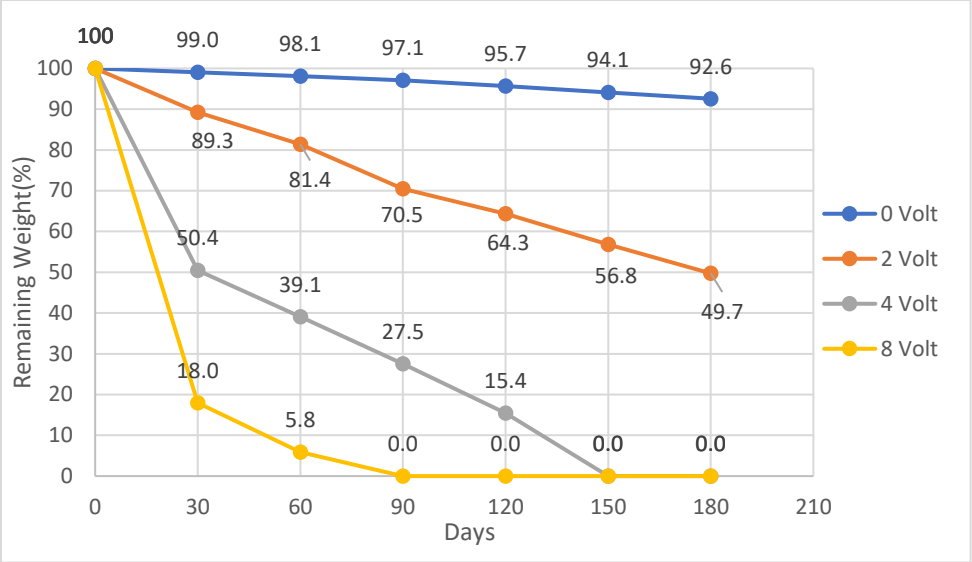

Figure 84. Effect of Voltages at 100,000 ppm and 0.01" Crack Width.

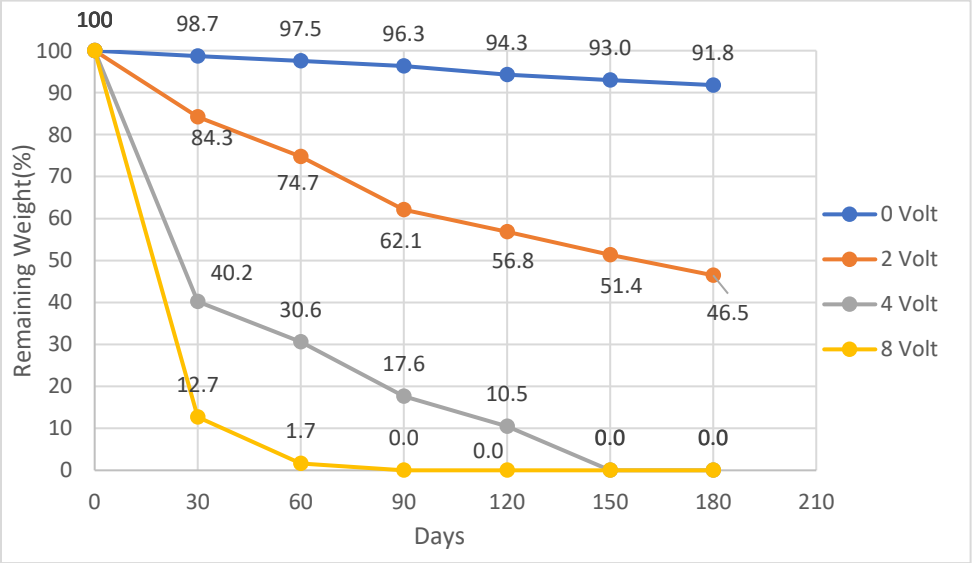

Figure 85. Effect of Voltages at 100,000 ppm and 0.03" Crack Width.

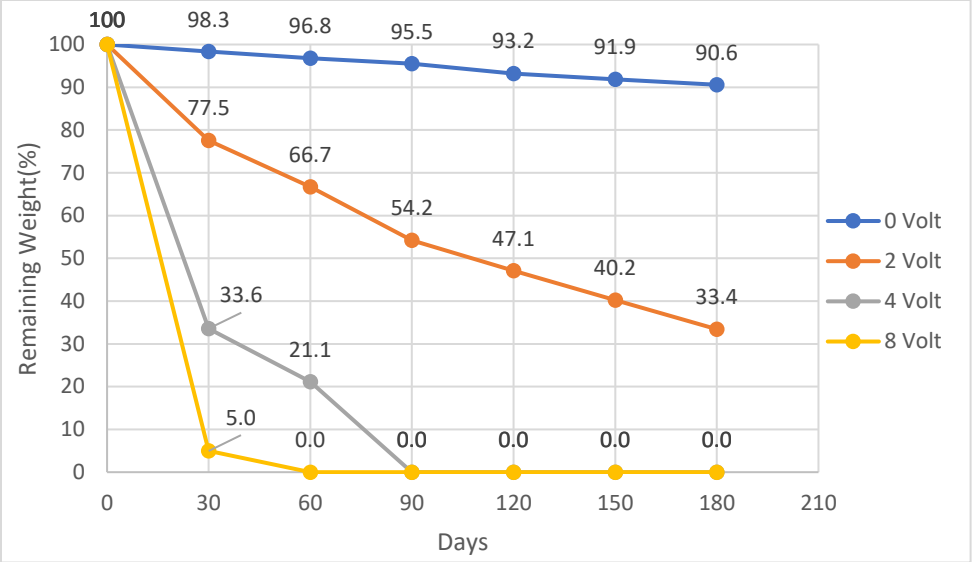

Figure 86. Effect of Voltages at 100,000 ppm and 0.05" Crack Width.

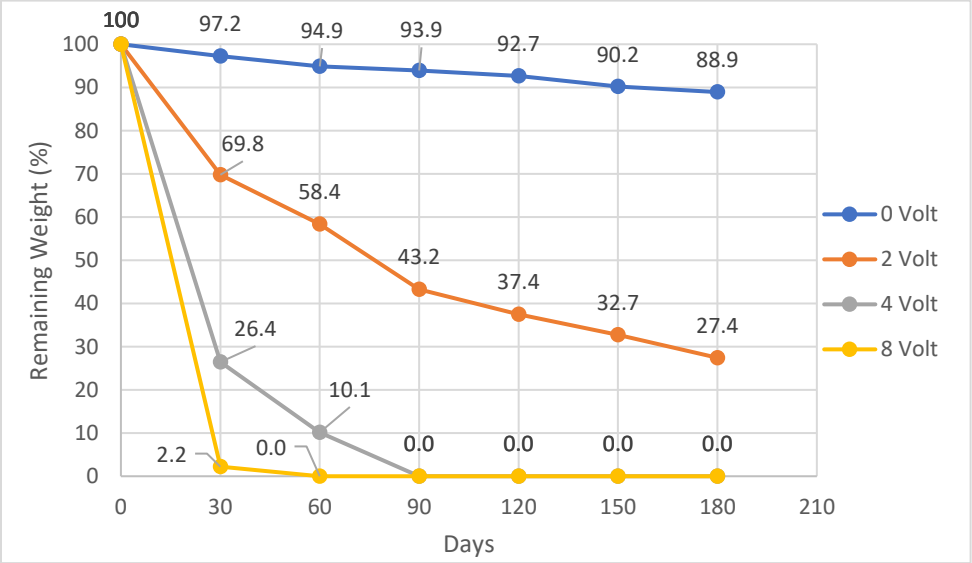

Figure 87. Effect of Voltages at 100,000 ppm and 0.1" Crack Width.

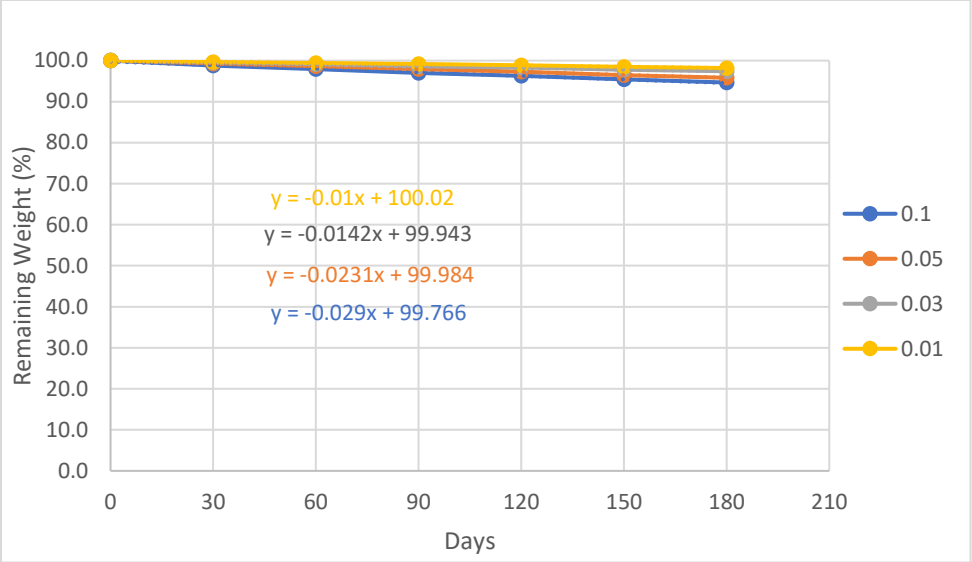

Figure 88. Effect of Crack Width at 0 Volt & 2,000 ppm.

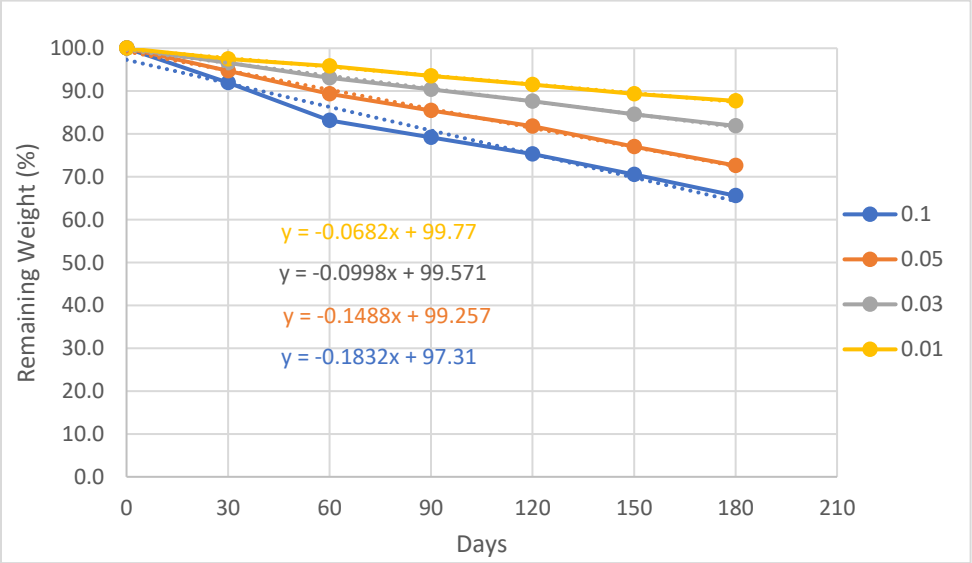

Figure 89. Effect of Crack Width at 2 Volt & 2,000 ppm.

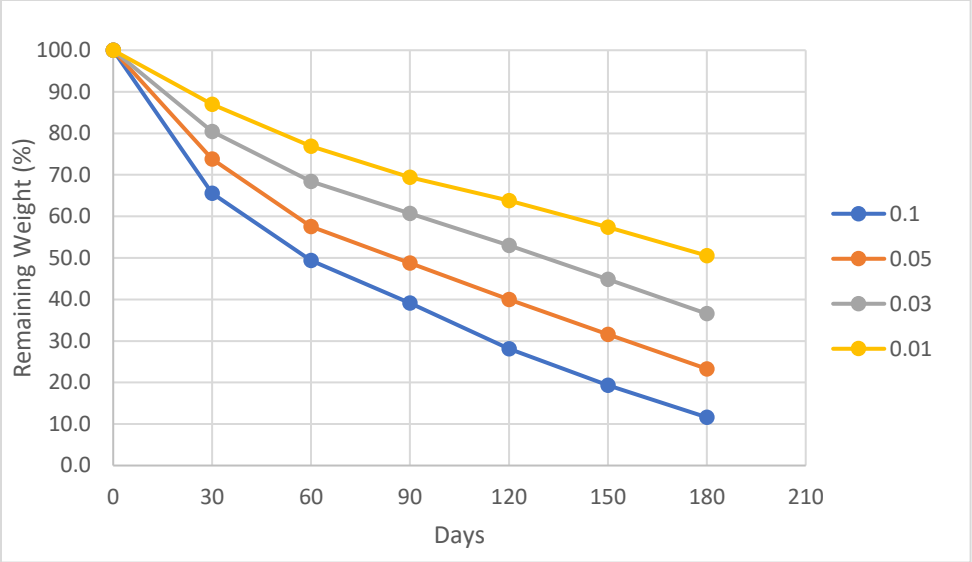

Figure 90. Effect of Crack Width at 4 Volt & 2,000 ppm.

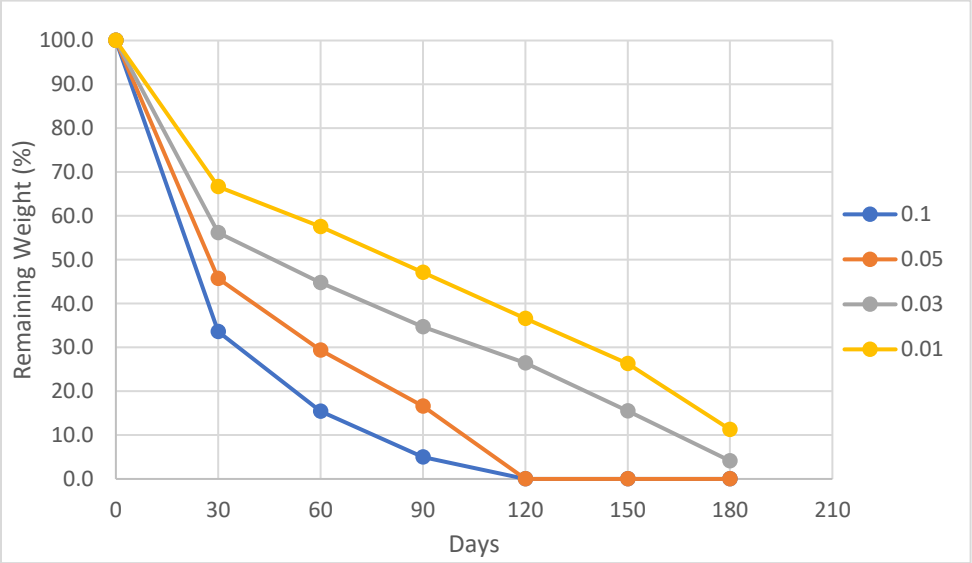

Figure 91. Effect of Crack Width at 8 Volt & 2,000 ppm.

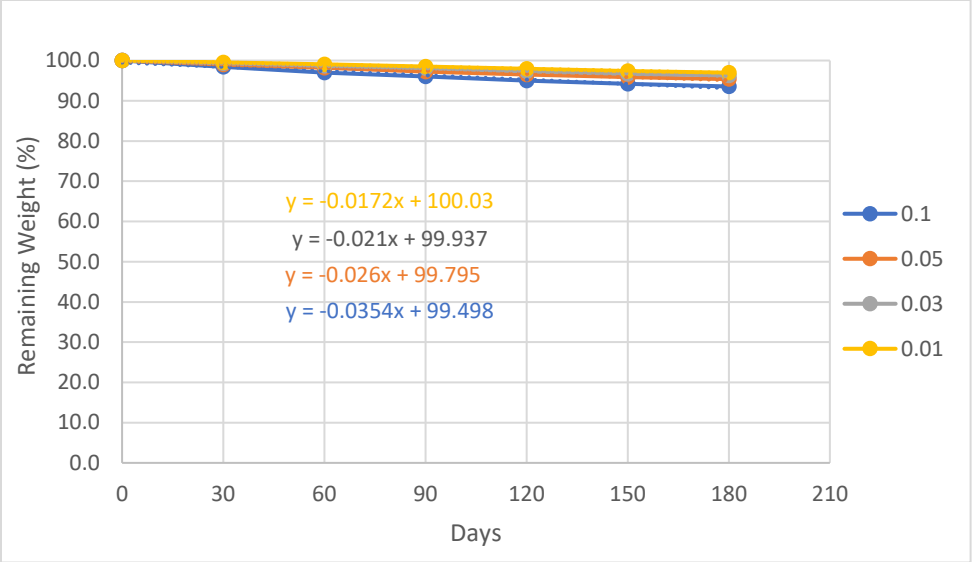

Figure 92. Effect of Crack Width at 0 Volt & 30,000 ppm.

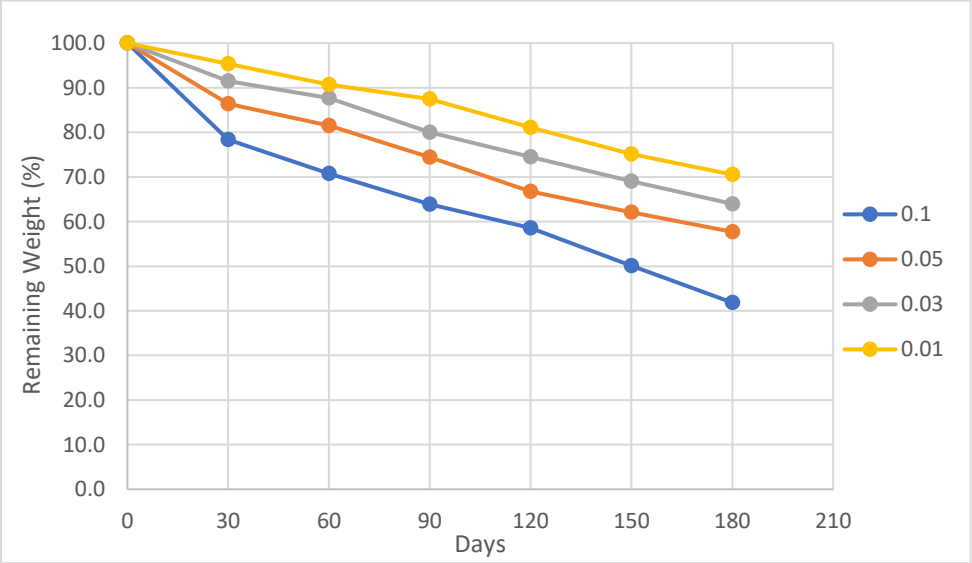

Figure 93. Effect of Crack Width at 2 Volt & 30,000 ppm.

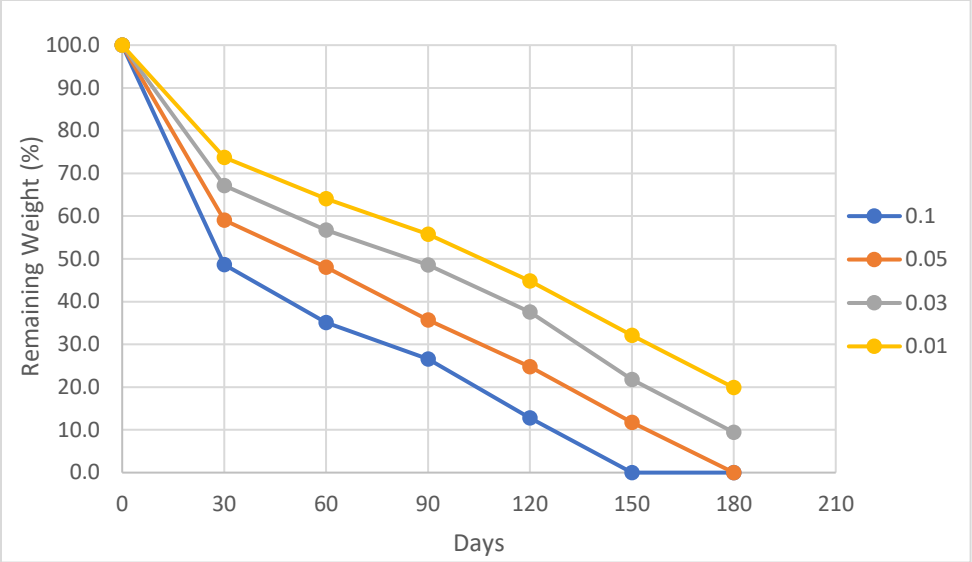

Figure 94. Effect of Crack Width at 4 Volt & 30,000 ppm.

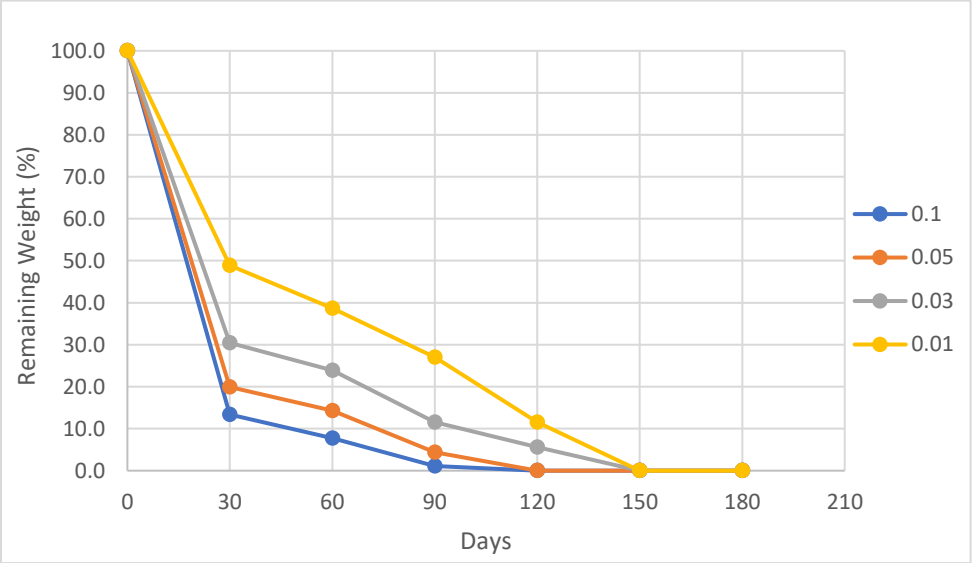

Figure 95. Effect of Crack Width at 8 Volt & 30,000 ppm.

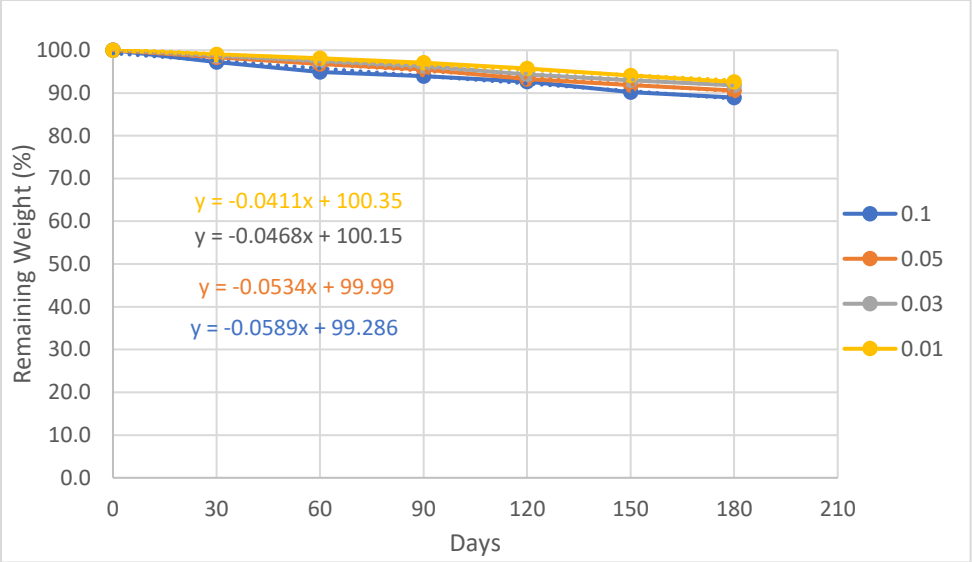

Figure 96. Effect of Crack Width at 0 Volt & 100,000 ppm.

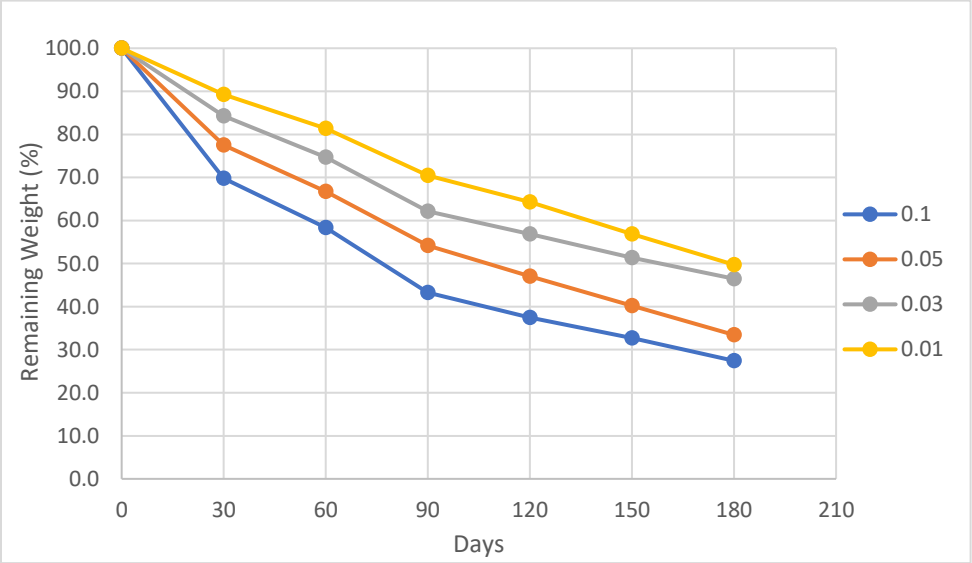

Figure 97. Effect of Crack Width at 2 Volt & 100,000 ppm.

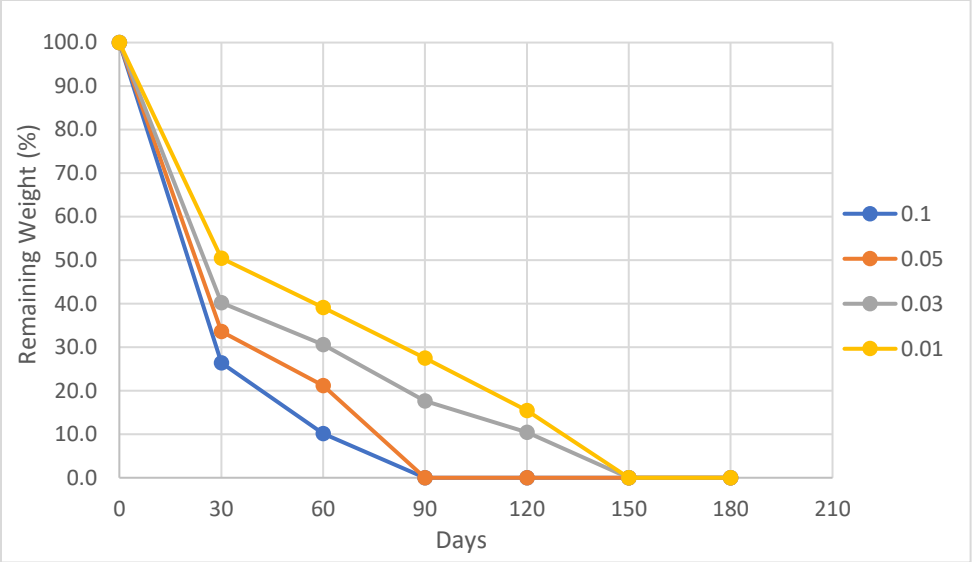

Figure 98. Effect of Crack Width at 4 Volt & 100,000 ppm.

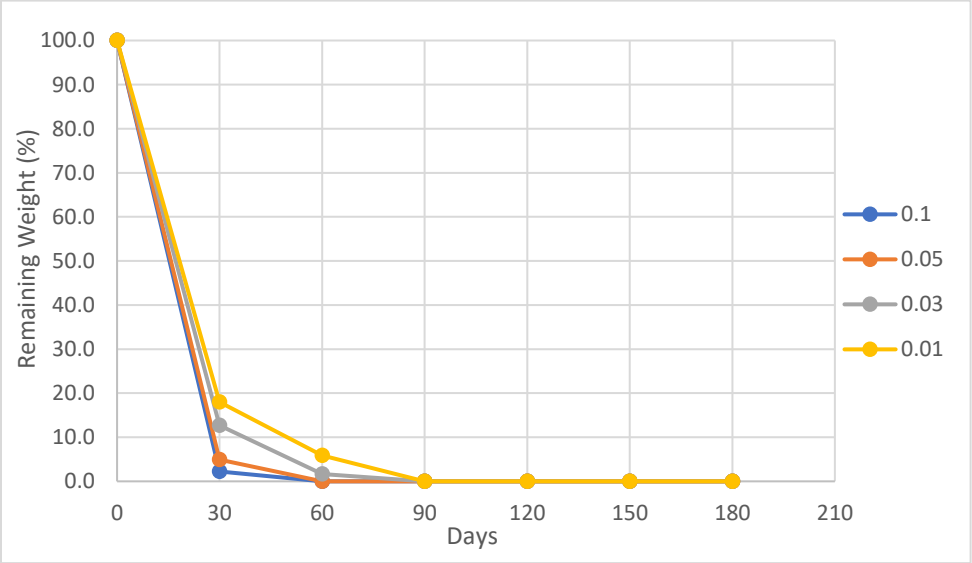

Figure 99. Effect of Crack Width at 8 Volt & 100,000 ppm.

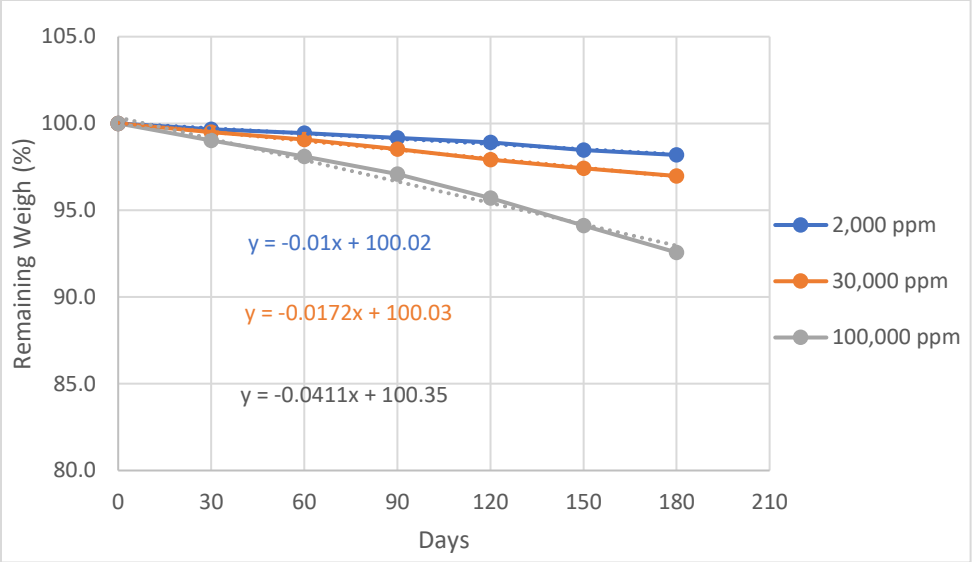

Figure 100. Effect of Concentration Solutions at 0.01" Crack Width & 0 Volt.

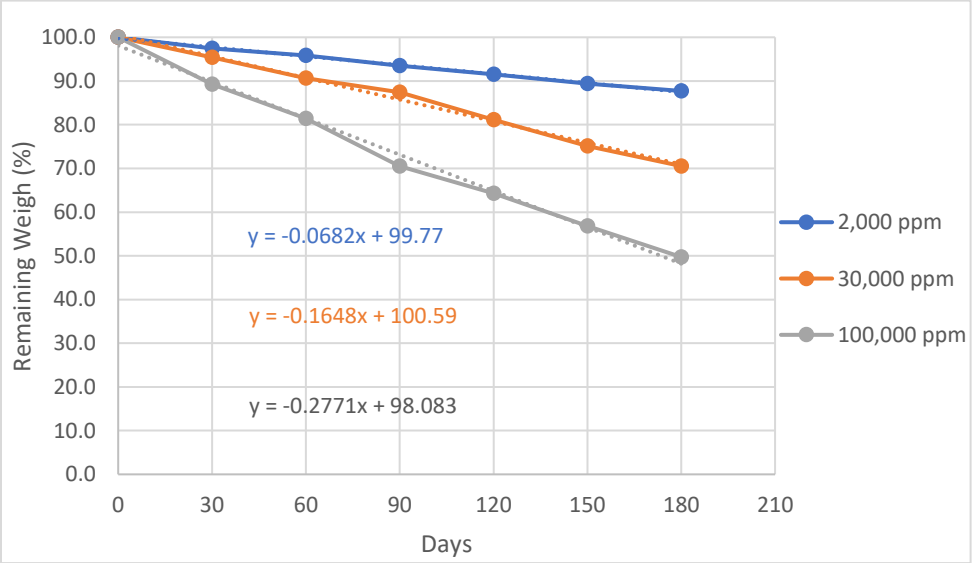

Figure 101. Effect of Concentration Solutions at 0.01" Crack Width & 2 Volt.

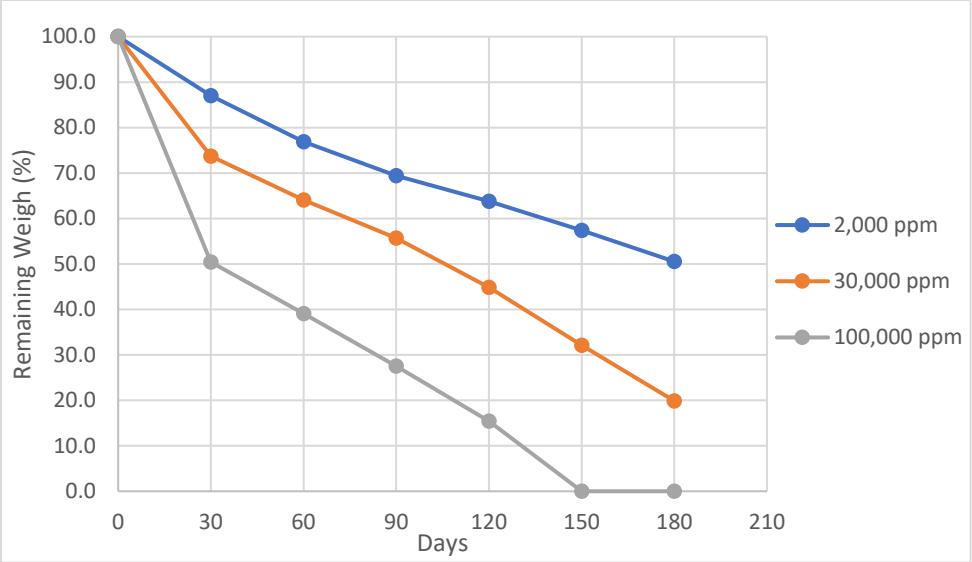

Figure 102. Effect of Concentration Solutions at 0.01" Crack Width & 4 Volt.

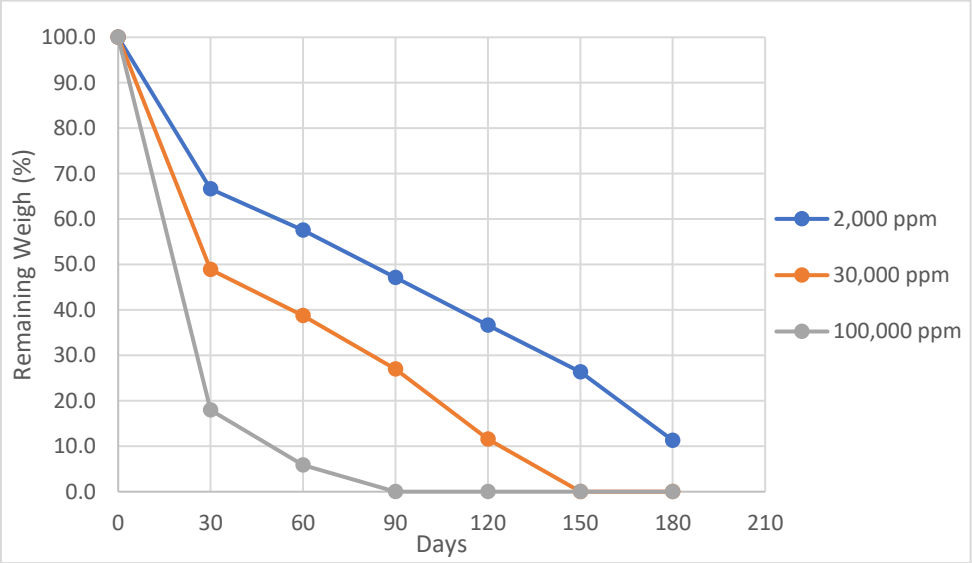

Figure 103. Effect of Concentration Solutions at 0.01" Crack Width & 8 Volt.

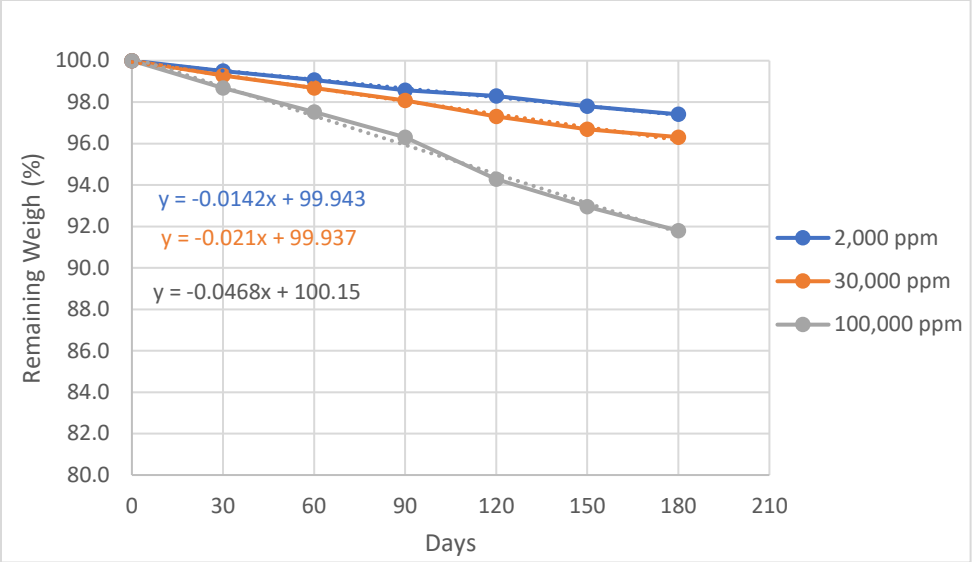

Figure 104. Effect of Concentration Solutions at 0.03" Crack Width & 0 Volt.

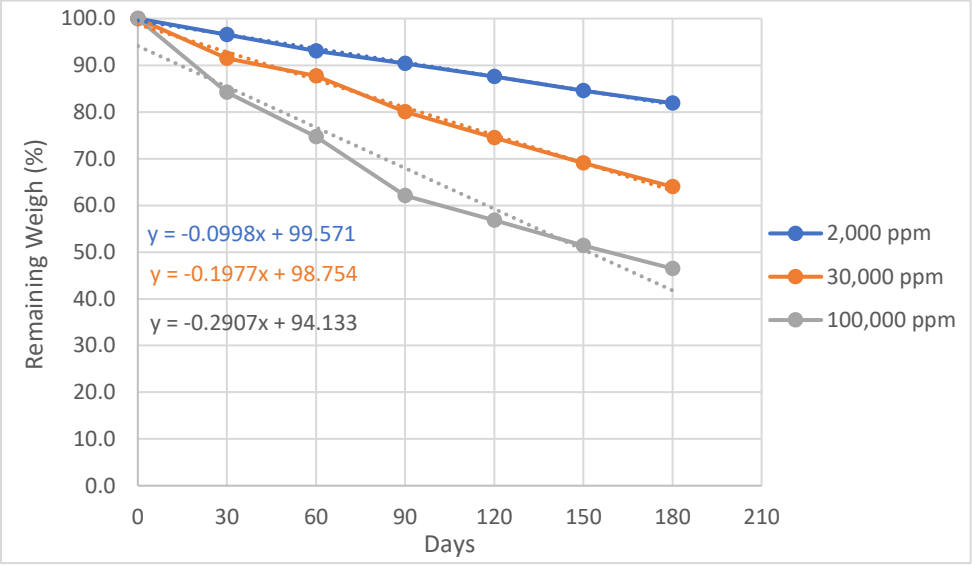

Figure 105. Effect of Concentration Solutions at 0.03" Crack Width & 2 Volt.

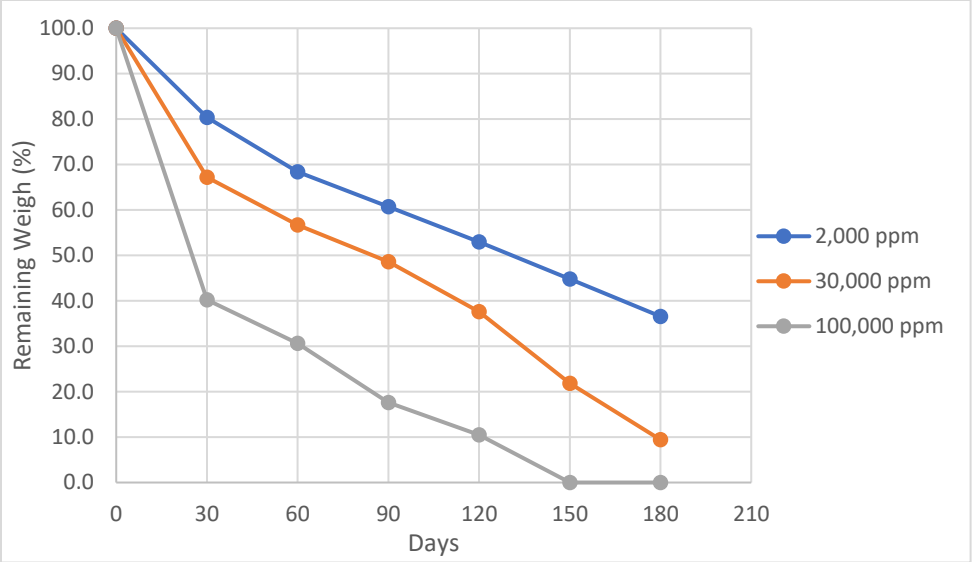

Figure 106. Effect of Concentration Solutions at 0.03" Crack Width & 4 Volt.

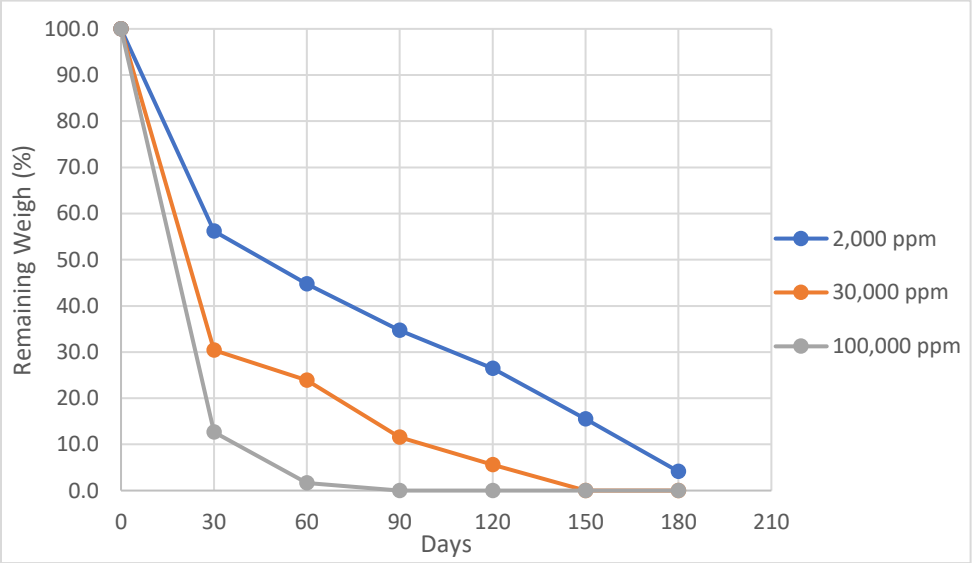

Figure 107. Effect of Concentration Solutions at 0.03" Crack Width & 8 Volt.

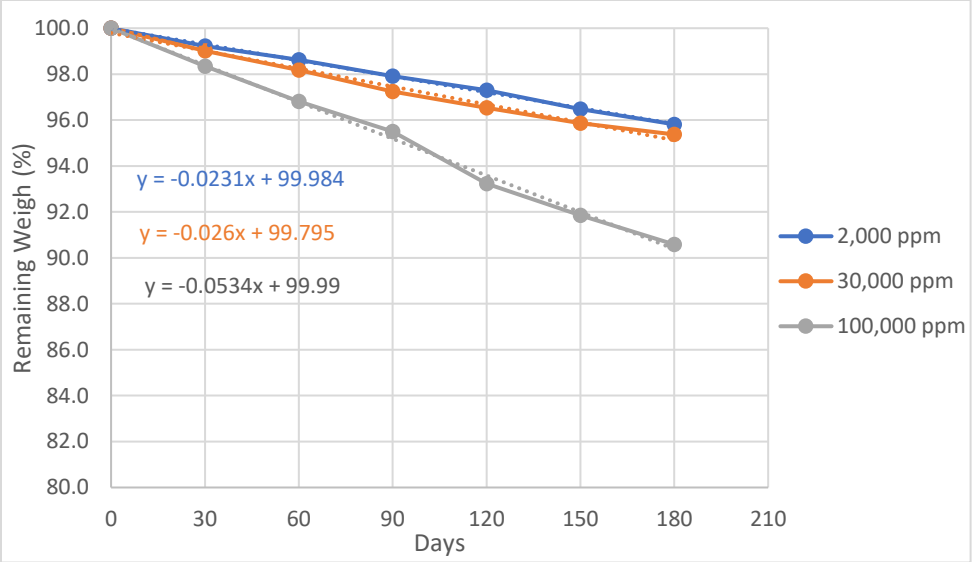

Figure 108. Effect of Concentration Solutions at 0.05" Crack Width & 0 Volt.

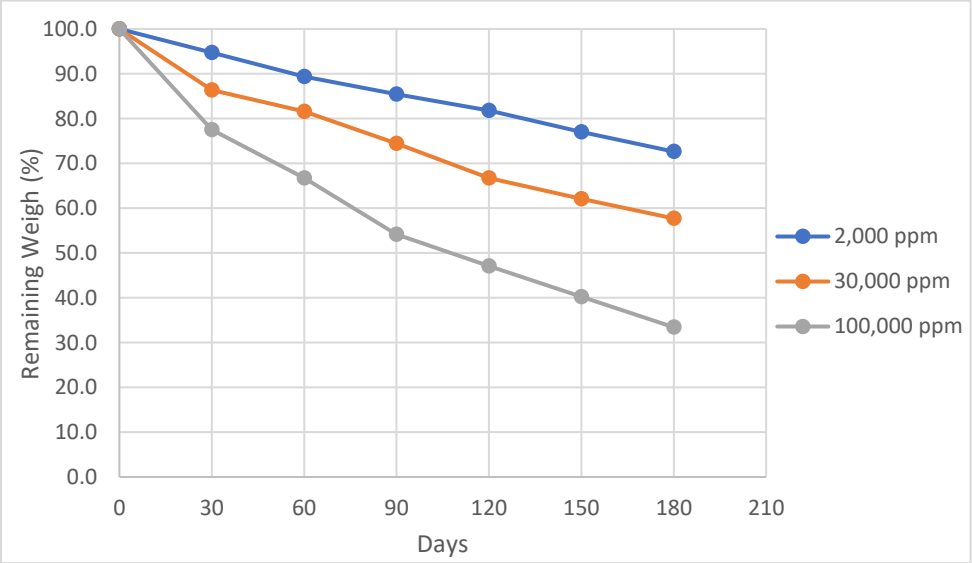

Figure 109. Effect of Concentration Solutions at 0.05" Crack Width & 2 Volt.

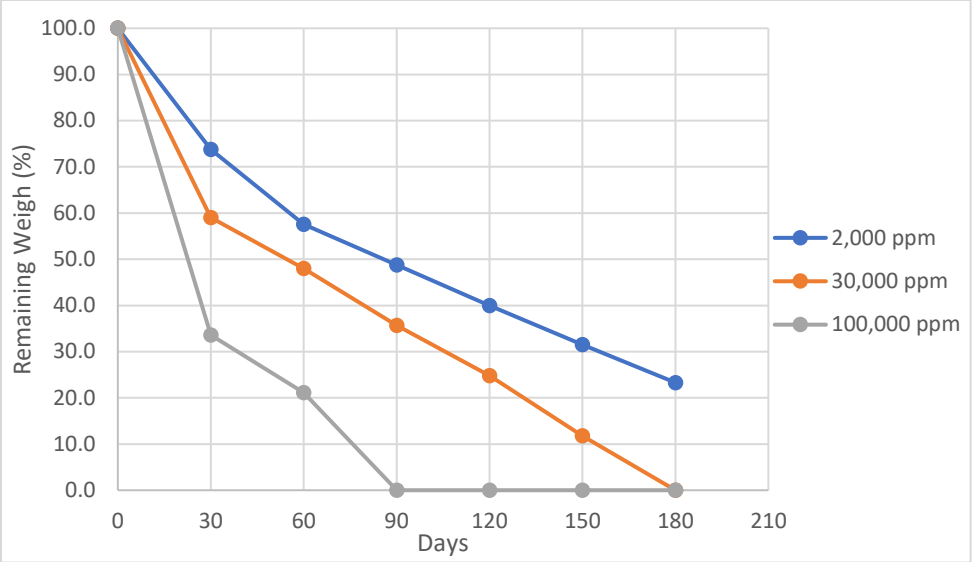

Figure 110. Effect of Concentration Solutions at 0.05" Crack Width & 4 Volt.

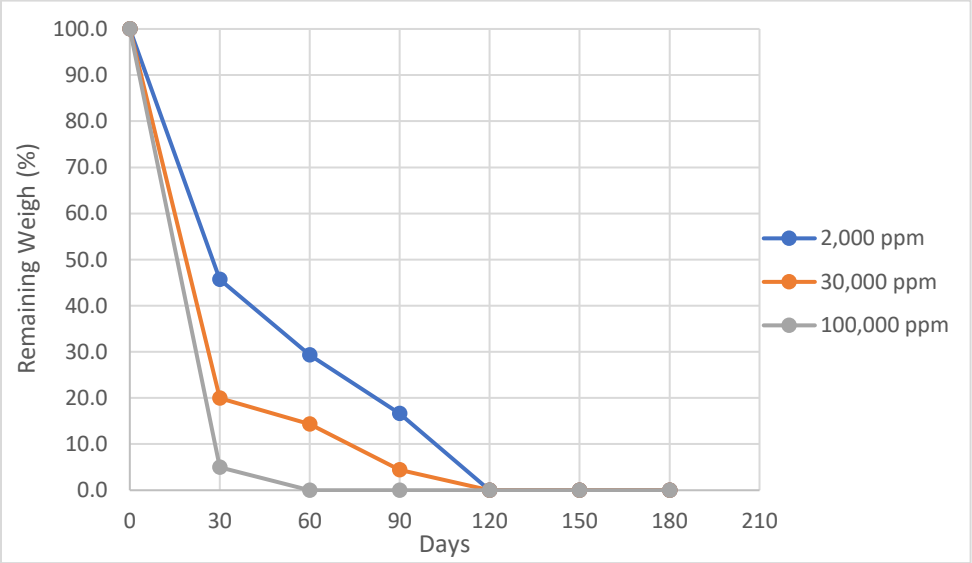

Figure 111. Effect of Concentration Solutions at 0.05" Crack Width & 8 Volt.

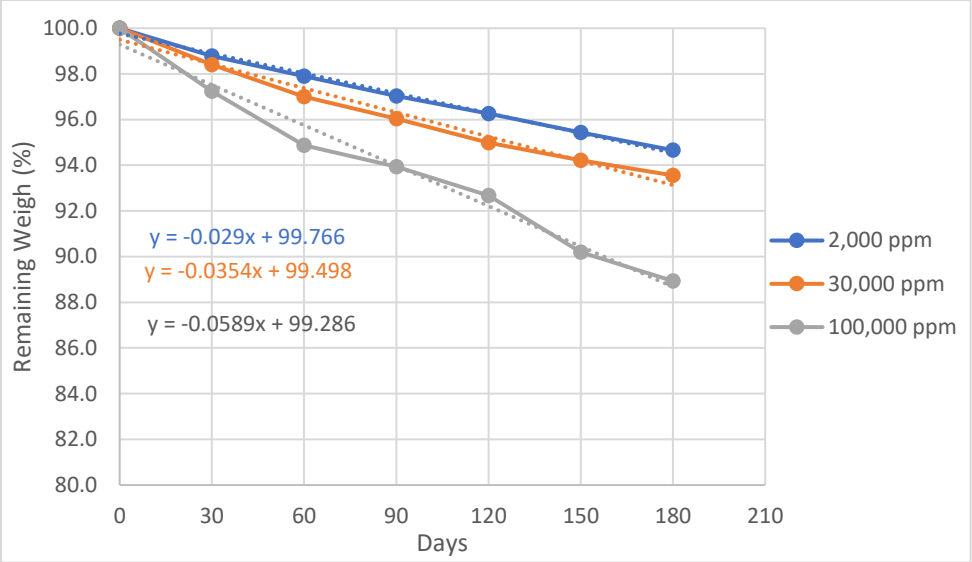

Figure 112. Effect of Concentration Solutions at 0.1" Crack Width & 0 Volt.

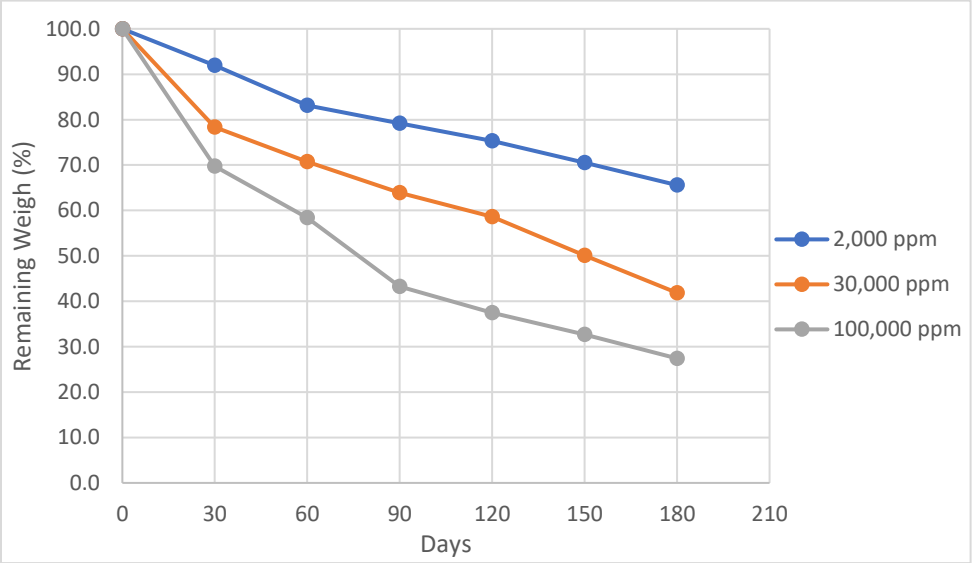

Figure 113. Effect of Concentration Solutions at 0.1" Crack Width & 2 Volt.

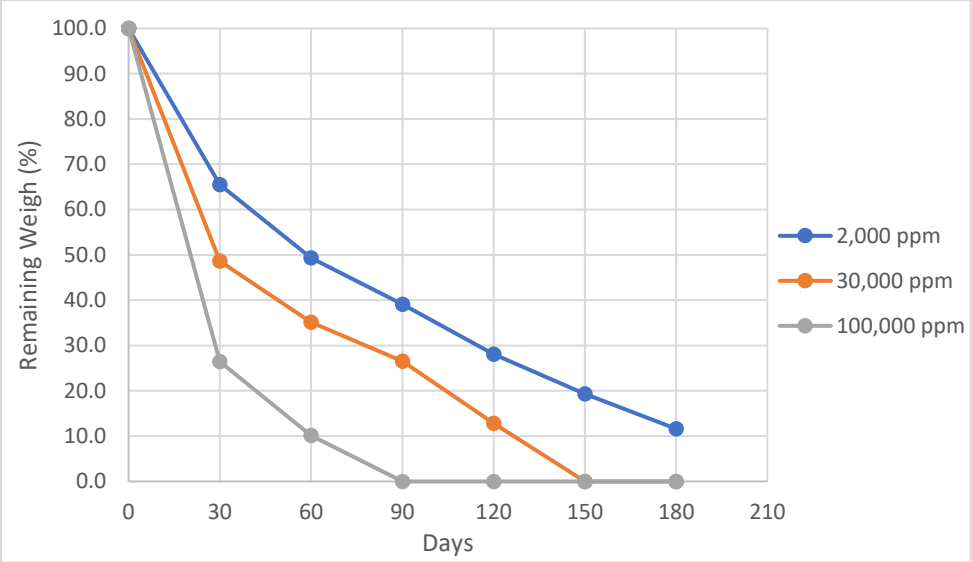

Figure 114. Effect of Concentration Solutions at 0.1" Crack Width & 4 Volt.

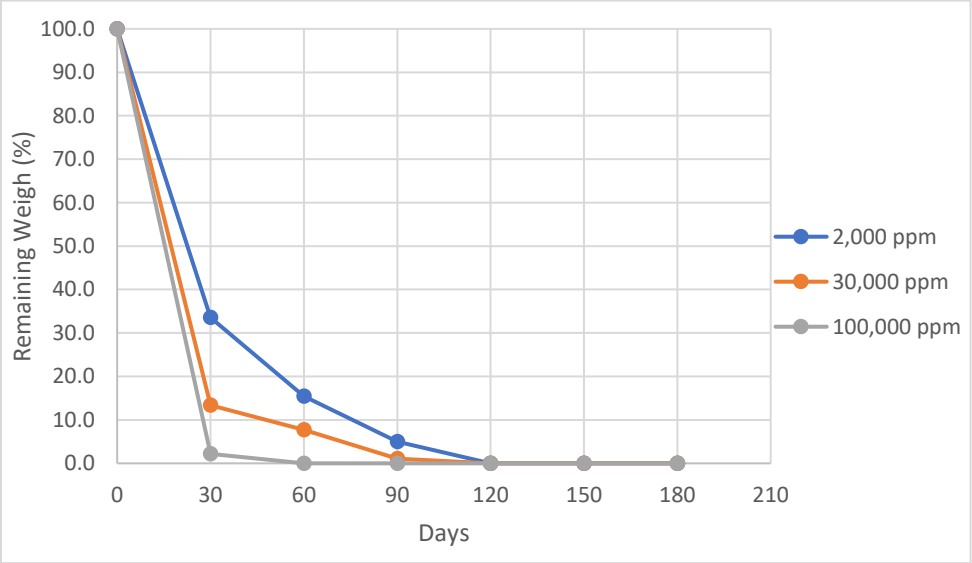

Figure 115. Effect of Concentration Solutions at 0.1" Crack Width & 8 Volt.

Appendix III: Codes Generated in Python Software

1. Import the Required Libraries

```
import pandas as pd
import numpy as np
import matplotlib.pyplot as plt
```

2. Perform Correlation Analysis

```
correlation_matrix = data.corr()
correlation_matrix
```

3. Perform Linear Regression.

```
import statsmodels.api as sm

# Create the design matrix
X = data[['Days', 'Concentration Solutions', 'Crack Width', 'Voltage']]
X = sm.add_constant(X)  # Add a constant term for the intercept

# Create the target variable
y = data['Remaining Weight']

# Fit the linear regression model
model = sm.OLS(y, X).fit()

# Print the model summary
print(model.summary())
```

4. Visualize the Results

```
# Plotting observed vs. predicted values
predicted_values = model.predict(X)
plt.scatter(y, predicted_values)
plt.xlabel('Observed')
plt.ylabel('Predicted')
plt.title('Observed vs. Predicted Values')
plt.show()

# Plotting residuals
residuals = model.resid
plt.hist(residuals)
plt.xlabel('Residuals')
plt.ylabel('Frequency')
plt.title('Residual Distribution')
plt.show()
```

5. Interaction regression

```
import pandas as pd
import statsmodels.api as sm

# Load the data from the Excel file
file_path = r'C:\Users\shahriar\Desktop\Data for Analysis.xlsx'
sheet_name = 'Sheet1'
df = pd.read_excel(file_path, sheet_name=sheet_name)
# Create interaction terms
df['Interaction_1'] = df['Days'] * df['Concentration Solutions']
df['Interaction_2'] = df['Days'] * df['Crack Width']
df['Interaction_3'] = df['Days'] * df['Voltage']
df['Interaction_4'] = df['Concentration Solutions'] * df['Crack Width']
df['Interaction_5'] = df['Concentration Solutions'] * df['Voltage']
df['Interaction_6'] = df['Crack Width'] * df['Voltage']
```

```
df['Interaction_7'] = df['Days'] * df['Concentration Solutions'] * df['Crack Width']

df['Interaction_8'] = df['Days'] * df['Concentration Solutions'] * df['Voltage']

df['Interaction_9'] = df['Days'] * df['Crack Width'] * df['Voltage']

df['Interaction_10'] = df['Concentration Solutions'] * df['Crack Width'] *
df['Voltage']

df['Interaction_11'] = df['Days'] * df['Concentration Solutions'] * df['Crack Width']
* df['Voltage']

# Define the independent variables (including interaction terms) and the dependent variable

X = df[['Days', 'Concentration Solutions', 'Crack Width', 'Voltage',

'Interaction_1', 'Interaction_2', 'Interaction_3', 'Interaction_4',

'Interaction_5', 'Interaction_6', 'Interaction_7', 'Interaction_8',

'Interaction_9', 'Interaction_10', 'Interaction_11']]

y = df['Remaining Weight']
```

```
# Add a constant term to the independent variables
X = sm.add_constant(X)


# Fit the OLS model
model = sm.OLS(y, X).fit()


# Print the regression results
print(model.summary())
```

Appendix IV: Steps for Making the Prediction MODEL in MATLAB

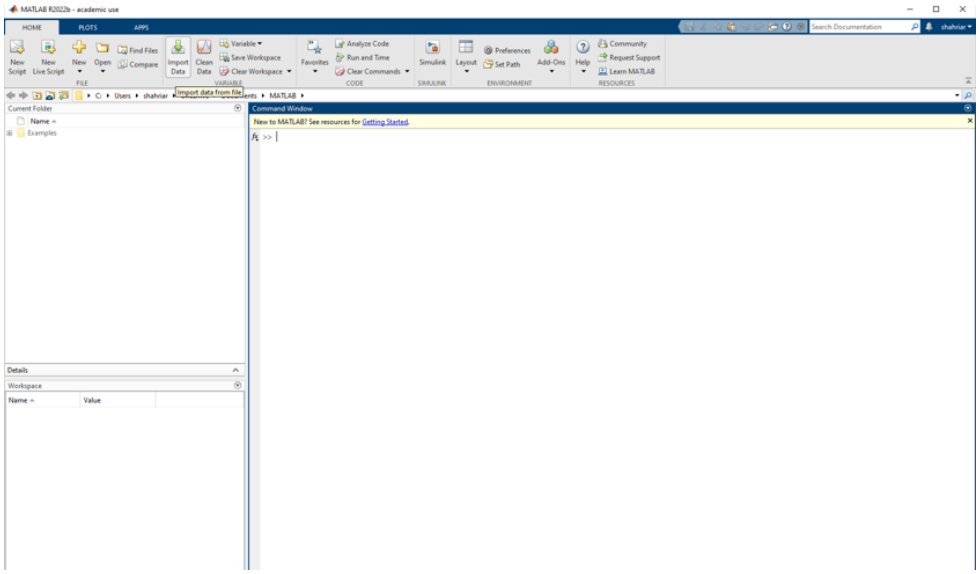

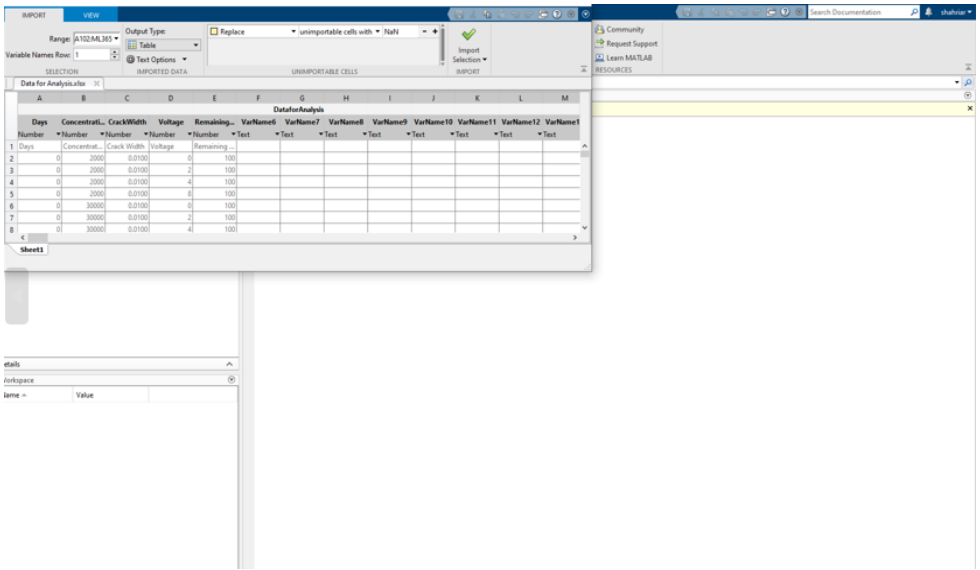

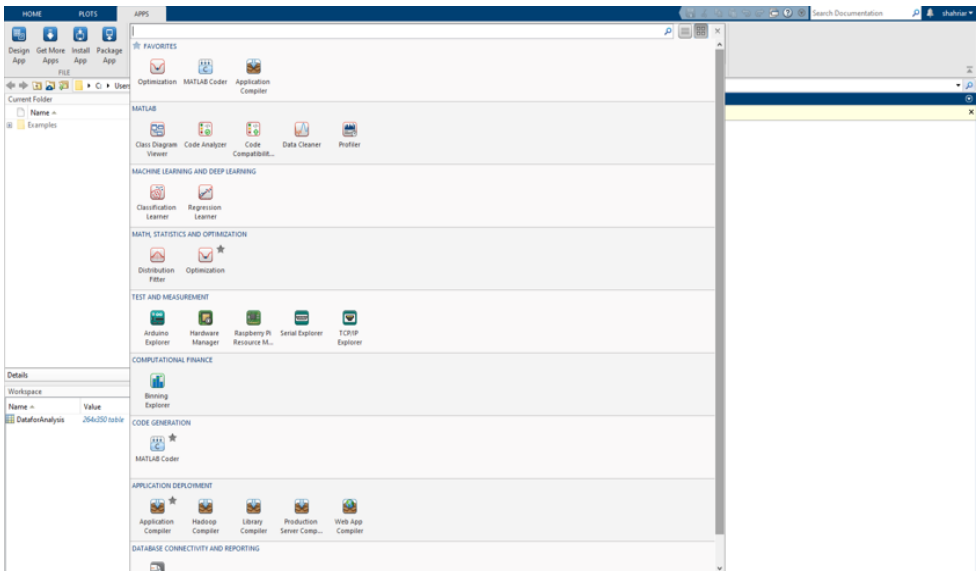
HOME
PLOTS
APPS
Design App
Get More Apps
Install App
Package App
FAVORITES
Optimization
MATLAB Coder
Application Compiler
MATLAB
Class Diagram Viewer
Code Analyzer
Code Compatibilit...
Data Cleaner
Profiler
MACHINE LEARNING AND DEEP LEARNING
Classification Learner
Regression Learner
MATH, STATISTICS AND OPTIMIZATION
Distribution Fitter
Optimization
TEST AND MEASUREMENT
Arduino Explorer
Hardware Manager
Raspberry Pi Resource M...
Serial Explorer
TCP/IP Explorer
COMPUTATIONAL FINANCE
Binning Explorer
CODE GENERATION
MATLAB Coder
APPLICATION DEPLOYMENT
Application Compiler
Hadoop Compiler
Library Compiler
Production Server Comp...
Web App Compiler
DATABASE CONNECTIVITY AND REPORTING
Current Folder
Name
Examples
Details
Workspace
Name
Value
DataforAnalysis
264x350 table

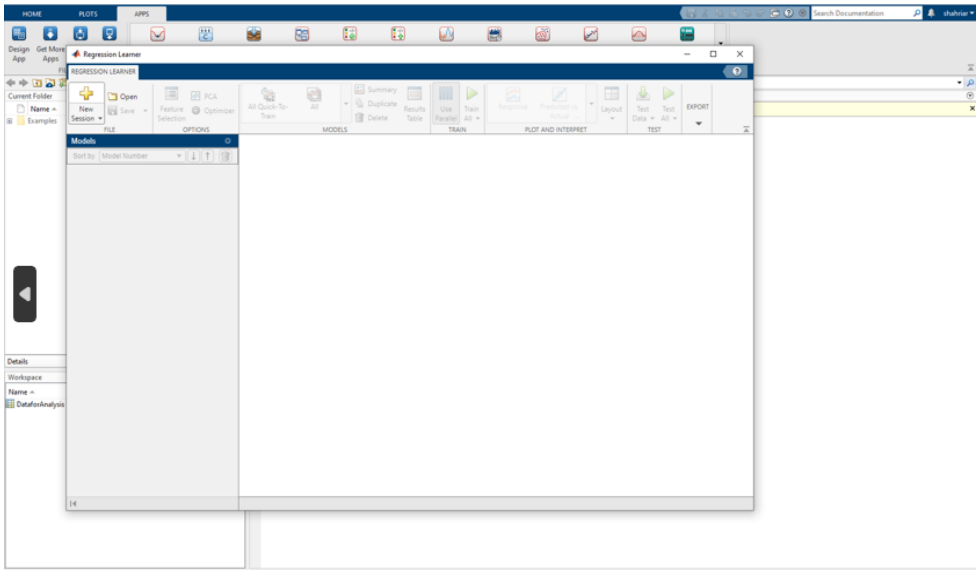
HOME
PLOTS
APPS
Regression Learner
REGRESSION LEARNER
New Session
Open
Save
FILE
Feature Selection
PCA
Optimizer
OPTIONS
All Quick-To-Train
All
Summary
Duplicate
Delete
Results Table
MODELS
Use Parallel
Train All
TRAIN
Response
Predicted vs. Actual
PLOT AND INTERPRET
Layout
Test Data
Test All
TEST
EXPORT
Models
Sort by
Model Number
Current Folder
Name
Examples
Details
Workspace
Name
DataforAnalysis

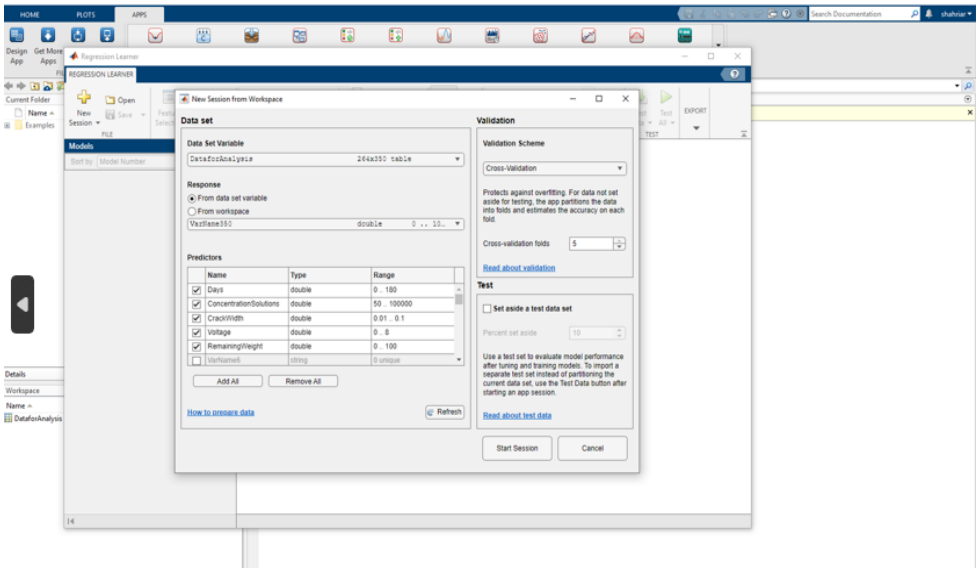
HOME
PLOTS
APPS
Regression Learner
REGRESSION LEARNER
New Session from Workspace
Data set
Data Set Variable
DataforAnalysis
264x350 table
Response
From data set variable
From workspace
VarName350
double
Predictors
Name
Type
Range
Days
double
0 .. 180
ConcentrationSolutions
double
50 .. 100000
CrackWidth
double
0.01 .. 0.1
Voltage
double
0 .. 8
RemainingWeight
double
0 .. 100
VarName6
string
0 unique
Add All
Remove All
How to prepare data
Refresh
Validation
Validation Scheme
Cross-Validation
Protects against overfitting. For data not set aside for testing, the app partitions the data into folds and estimates the accuracy on each fold.
Cross-validation folds
5
Read about validation
Test
Set aside a test data set
Percent set aside
10
Use a test set to evaluate model performance after tuning and training models. To import a separate test set instead of partitioning the current data set, use the Test Data button after starting an app session.
Read about test data
Start Session
Cancel
Models
Sort by
Model Number
Details
Workspace
Name
DataforAnalysis

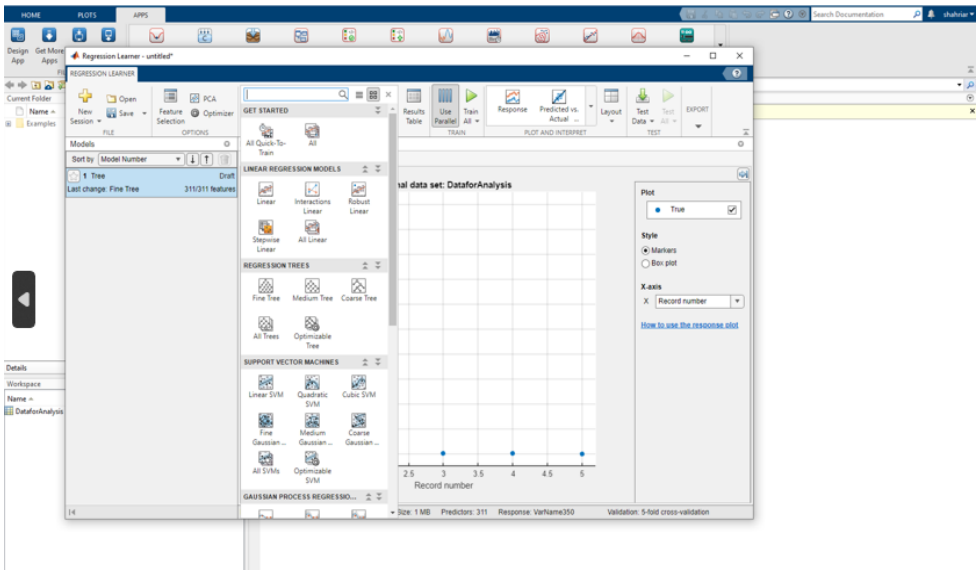
HOME
PLOTS
APPS
Regression Learner - untitled*
REGRESSION LEARNER
GET STARTED
All Quick-To-Train
All
LINEAR REGRESSION MODELS
Linear
Interactions Linear
Robust Linear
Stepwise Linear
All Linear
REGRESSION TREES
Fine Tree
Medium Tree
Coarse Tree
All Trees
Optimizable Tree
SUPPORT VECTOR MACHINES
Linear SVM
Quadratic SVM
Cubic SVM
Fine Gaussian ...
Medium Gaussian ...
Coarse Gaussian ...
All SVMs
Optimizable SVM
GAUSSIAN PROCESS REGRESSIO...
Results Table
Use Parallel
Train All
Response
Predicted vs. Actual
Layout
Test Data
EXPORT
TRAIN
PLOT AND INTERPRET
TEST
al data set: DataforAnalysis
Record number
Plot
True
Style
Markers
Box plot
X-axis
Record number
How to use the response plot
Models
Sort by
Model Number
1 Tree
Last change: Fine Tree
311/311 features
Details
Workspace
DataforAnalysis
Size: 1 MB
Predictors: 311
Response: VarName350
Validation: 5-fold cross-validation